Shear Bands in Granular Materials: Formation and Persistence at Smooth Walls

Von der Fakultät für Physik
der Universität Duisburg-Essen
zur Erlangung des Grades
Dr. rer. nat.
genehmigte Dissertation
von

Zahra Shojaaee
aus Teheran

Tag der Disputation: 08.06.2012
Referent: Prof. Dr. Dietrich E. Wolf
Korreferent: Prof. Dr. Stefan Luding

Für meine Eltern, Masoumeh Joudaki und Khodarahm Shojaaee, die meine Liebe zur Physik respektiert und liebevoll unterstützt haben.

Abstract

This thesis contains numerical studies of rheology and shear characteristics of dense assemblies of granular materials. Beside the various experimental and theoretical studies, which deal with these materials, there is also a wide variety of simulation methods, which are used to study the flow behavior, compaction and other characteristics of granular materials. In this work, the contact dynamics method (CD) has been used to study two-dimensional systems of hard, dry disks. The particles interact by Coulomb friction forces parallel to, and volume exclusion forces normal to the contact surfaces, with collisions being fully inelastic. The shear flow is confined between two parallel, smooth, frictional walls, moving with opposite prescribed velocities. Discrete element simulations, carried out in samples with prescribed normal stress reveal that, unlike rough walls made of strands of particles, absolutely smooth but frictional ones can lead to inhomogeneous shear rate and shear strain localization in boundary layers. These are both caused by slip at smooth walls. Three shear regimes associated with different shear velocity intervals are identified and studied in this work. The transitions between these regimes are essentially independent of system size and occur for specific values of shear velocity. Applying constitutive laws deduced both for the bulk material and the boundary regions supplemented by an elementary stability analysis, the occurrence of both transitions, as well as the characteristic transient times are predicted. Investigating the role of the rotational degrees of freedom of round frictional particles and their microscopic contact properties at smooth walls, a critical microscopic friction coefficient at the walls is identified, below which the walls are unable to shear the system. New distinctive features are observed at this critical point. To perform a finite-size-analysis, simulations with very large systems have been frequently necessary during this thesis. To afford large scale simulations with CD, which are more comparable to real granular systems, within a conceivable time, a fully parallel version of CD is presented in this work. For large enough systems, 100% efficiency is achieved for up to 256 processors using a hierarchical domain decomposition with dynamic load balancing. Compared to the sequential implementation, no influence of the parallelization on simulation results is found.

Zusammenfassung

Diese Arbeit behandelt die numerische Untersuchung der Rheologie und Schereigenschaften granularer Materie aus runden Teilchen. Neben den vielfältigen experimentellen und theoretischen Arbeiten, die sich mit dieser Materie beschäftigen, gibt es unterschiedliche Simulationsmethoden mit denen das Fließverhalten, die Kompaktierung und andere Eigenschaften granularer Materie untersucht werden. In dieser Arbeit wurde die Kontakt-Dynamik-Methode (CD) zur Untersuchung eines zweidimensionalen Systems aus granularer Materie angewandt. Die Teilchen sind starre Scheiben und die einzigen Kontaktkräfte zwischen diesen sind die Coulombsche Reibungskraft parallel und Volumenausschluss-Kräfte senkrecht zur Kontaktfläche. Die Teilchen befinden sich in einem System mit planarer Geometrie, das von oben und unten durch zwei parallele Wände begrenzt ist. Der Druck und die Schergeschwindigkeit sind in jeder Simulation fest vorgegeben und bleiben während der gesamten Simulation konstant. In dieser Arbeit werden, im Gegensatz zu vielen aktuellen Untersuchungen, absolut glatte, mit Reibung versehene Wände zur Scherung benutzt. Diese führen zu sehr inhomogenen Scherraten im System mit deutlicher Scherlokalisierung an den Wänden, die durch den Schlupf an diesen verursacht wird. Drei unterschiedliche Scherregime werden hierbei beobachtet. Jedes dieser Regime gehört zu einem wohldefinierten Intervall der Schergeschwindigkeit, das hauptsächlich von der Systemgröße unabhängig ist. Sowohl die Eigenschaften dieser drei Regime als auch die beiden Übergänge zwischen Ihnen werden detailliert in Kapitel 6 behandelt. In Kapitel 7 werden die konstitutiven Gesetze separat im Bulk und in den Grenzgebieten zu den Wänden hergeleitet. Anhand dieser konstitutiven Gesetze und ergänzender elementarer Stabilitätsanalysen wird das Vorkommen beider Übergänge, sowie charakteristische Transientenzeiten vorausberechnet. In Kapitel 8 wird eine kritische Mindestgröße des Reibungskoeffizienten an glatten Wänden festgestellt, die das Scheren ermöglicht. Bei diesem kritischen Reibungskoeffizienten wird ein besonderes Verhalten des Systems im quasistatischen Regime beobachtet, über welches zuvor noch nicht in der Literatur berichtet worden ist. In Kapitel 9 wird über eine erfolgreiche Parallelisierung der CD berichtet. Diese ermöglicht Simulationen in größeren Systemen, eher vergleichbar zur realen Systemen, die ebenso für die "Finite-Size-Analyse" notwendig sind.

Contents

List of Figures

List of Tables

1 Introduction

Granular media are a particular material class, due to their very different behavior in comparison to gases, fluids and solids. The importance of this material state is essentially based on its industrial applications [1–4]. The most manipulated material by man (if measured by tons) after water is granular material [2]. Lots of pharmaceutical products are delivered from powders. Also in the production of cement, granules such as calcium silicates are used. Lots of other industries such as food industry, cosmetics, coal mining and polymer industry have to deal with granular matter. Recently, the interest in the possible usage of granular or powder mixtures as a means of applying solid lubrication has increased. At temperatures greater than $500°C$, conventional liquid lubricants cannot be applied and particulate lubrication may be an attractive alternative [3]. Lots of industries have to deal with problems such as silo collapse, when filled with grains. Although silos are built from steel sheets and are supported by a steel frame, the resistance of granular matter against flow during the discharge can lead to a collapse of the whole massive structure [4]. Another problem faced by a large number of industries is segregation in granular systems with polydispersity [5, 6].

Granular material is very widespread in nature. The classical example is sand to be found in deserts and on the beaches. Snow is another frequent granular material in nature [2]. The movement of tectonic plates [7, 8] and avalanches [9, 10] are natural incidents related to the unusual behavior of granular matter.

All examples mentioned above make it clear that granular material with its numerous features and its widespread appearance in nature and industry is an important field of study for scientists. Physicists and civil engineers are very interested in understanding the granular behavior. This class of material has been studied over a long period of time experimentally. The first studies date back to the 19th century, in which M. Faraday discovered the convective instability in a vibrated powder [11] and O. Reynolds published the results of his experimental studies on dilatancy in granular matter [12, 13]. In 1941 E. R. Bagnold has published his book on sand dunes and sand transport [14]. In the last decades, however, much more scientists

have studied the different aspects of the behavior of granular material. Meanwhile, some theories have been developed to describe the granular characteristics and its flow. There are essentially two different theoretical approaches to describe granular flows. As a discrete, many particle system, one approach is to consider the individual particles, while the other is to view granular media as a macroscopic system, i.e. as a continuum [15–17]. Since the nineties, computer simulations of granular material have become a very important part of this research field, providing information on the scale of individual particles not only from the surface, but also from the interior of the material [18–21].

Depending on the surrounding environment, flow velocity, density and other parameters, granular material exhibits very different behavior [1, 4, 22–26]. Hence, despite long-time theoretical and experimental investigations in this area, no single practical constitutive law could describe the granular behavior in all its flow regimes [27–31]. The influence of boundaries on the rheology of granular material has always been one of the important parts of the granular research field [18–21, 32–34]. Velocity slip at the boundaries is one of the characteristics of granular flow [21] and boundary conditions, which involve slip, are important to understand the granular flows properly [20, 21, 35]. In this thesis the study of strain localization at smooth boundaries (i.e. with asperities much smaller compared to the particles in the system) is the focus of the work. Smooth boundaries occur frequently in nature and in industry for particles in the millimeter regime and above and are thus not just an academic idealization. Allowing for slip at the walls and considering only a short time window reveals clearly a collective behavior of the sheared granular material.

The outline of this thesis is as follows: In chapters 2 and 3 more insight is given into the properties of granular material and its flow properties. The results of previous contributions, on which this thesis is based are presented in these two chapters as well. In chapter 4, the simulation methods, which are suitable to study granular media are briefly introduced. The contact dynamics method is the discrete element method used in this numerical study, which is the focus of chapter 4. In chapter 5, the simulation setup, which has been used to perform the simulations throughout this work, is introduced. The distinctive flow regimes as a result of shearing at different velocities with smooth walls are introduced in chapter 6. The transitions between these regimes are predicted in chapter 7 by means of deduced constitutive laws and stability analysis. The role of Coulomb friction and rolling friction at smooth walls on slip and consequently on the shear behavior of the system is investigated in chapter 8. In chapter 9, a fully parallel version of the contact dynamics method is introduced. I conclude with a summary of new results and a brief discussion in chapter 10.

Part I

Theory

2 Granular Material

The general term "granular media" refers to systems involving a large collection of solid particles such as soil, sand, powder, minerals, grains, beads or rocks, immersed in a fluid environment, or vacuum such as particles in outer space. It could also be a gas, which is mostly the case, or a liquid such as in suspensions [36].

The size of individual particles in a granular media is at least 1μm. This criterion is a consequence of negligible thermal energy in comparison to the gravitational energy. The relevant energy scale in this context is the potential energy mgd of a grain of mass m raised by its own diameter d in the Earth's gravity g. For typical sand, this energy is at least 10^{12} times larger than the thermal energy $k_B T$ at room temperature [22]. On the other hand, the order of magnitude of typical cohesion forces between dry granular particles amounts to 100nN. In three dimensions (regardless of numerical factors of the order of magnitude 1) one could write:

$$F = \rho g r^3 \Longrightarrow r = \left(\frac{F}{\rho g}\right)^{\frac{1}{3}}, \tag{2.1}$$

with F being the cohesion force, ρ the density of granular particles and r the radius of the particles. Considering F and ρ to be of the order of magnitude 100nN [37] and 10000kg/m^3 respectively, Eq. (2.1) leads to a particle size of:

$$r = \left(\frac{10^{-7}\mathrm{N}}{10000\mathrm{kg/m^3} \cdot 10\mathrm{m/s^2}}\right)^{\frac{1}{3}} = 100\mu\mathrm{m}. \tag{2.2}$$

This would mean that such cohesion forces are important for particles of size 100μm or smaller. For larger particles, cohesion forces can be neglected in comparison to gravity [38].

One important characteristic of granular material is its tendency to build clusters of particles. This property of granular material is, in principle, based on different origins as for molecular gases. Essentially, the collisions between granular particles are inelastic. Here, in contrast to elastic gases with a restitution coefficient of $e \simeq 1$,

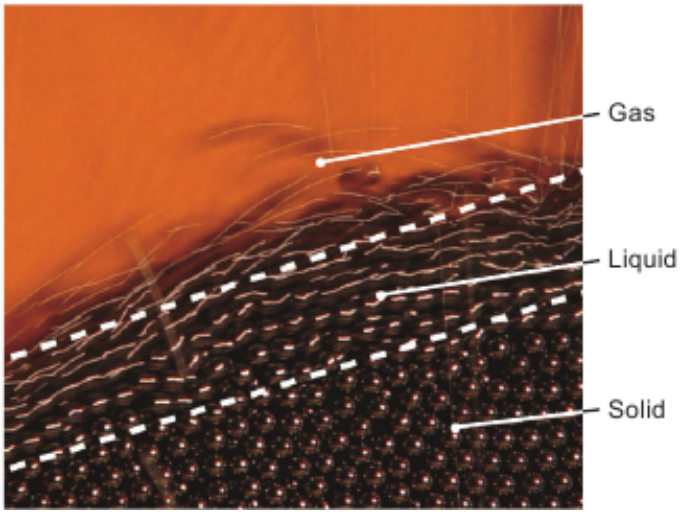

Figure 2.1: An illustration of the coexistence of solid, liquid and gas granular flow regimes obtained by pouring steel beads on a pile [39].

the restitution coefficient takes values in the interval $0 \leqslant e < 1$. The friction between the particles is the other dominant factor, determining their behavior. These two factors lead to dissipative interactions between the grains [22].

2.1 Some Features of Granular Material

2.1.1 Granular Temperature

As a result of dissipative nature of collisions between granular particles, without an external source pumping kinetic energy into the system, the granular packing would develop towards a dense system. To classify the system state the relevant measure is the *granular temperature* [40]:

$$T_{\text{gran}} = \langle (\vec{v}_{\text{grain}} - \langle \vec{v}_{\text{grain}} \rangle)^2 \rangle, \tag{2.3}$$

where the average is done over all particles in the system and also over time in the steady state. Without pumping energy into the system the granular temperature tends to get zero. In fact, this quantity reveals how large is the relative velocity between the particles. Accordingly, granular packings with different granular temperatures behave very differently. At high temperatures as a gas, at intermediate temperatures like a fluid, and at low temperatures like a solid. All these three regimes could be observed simultaneously in a granular system (Fig. 2.1). As the behavior of

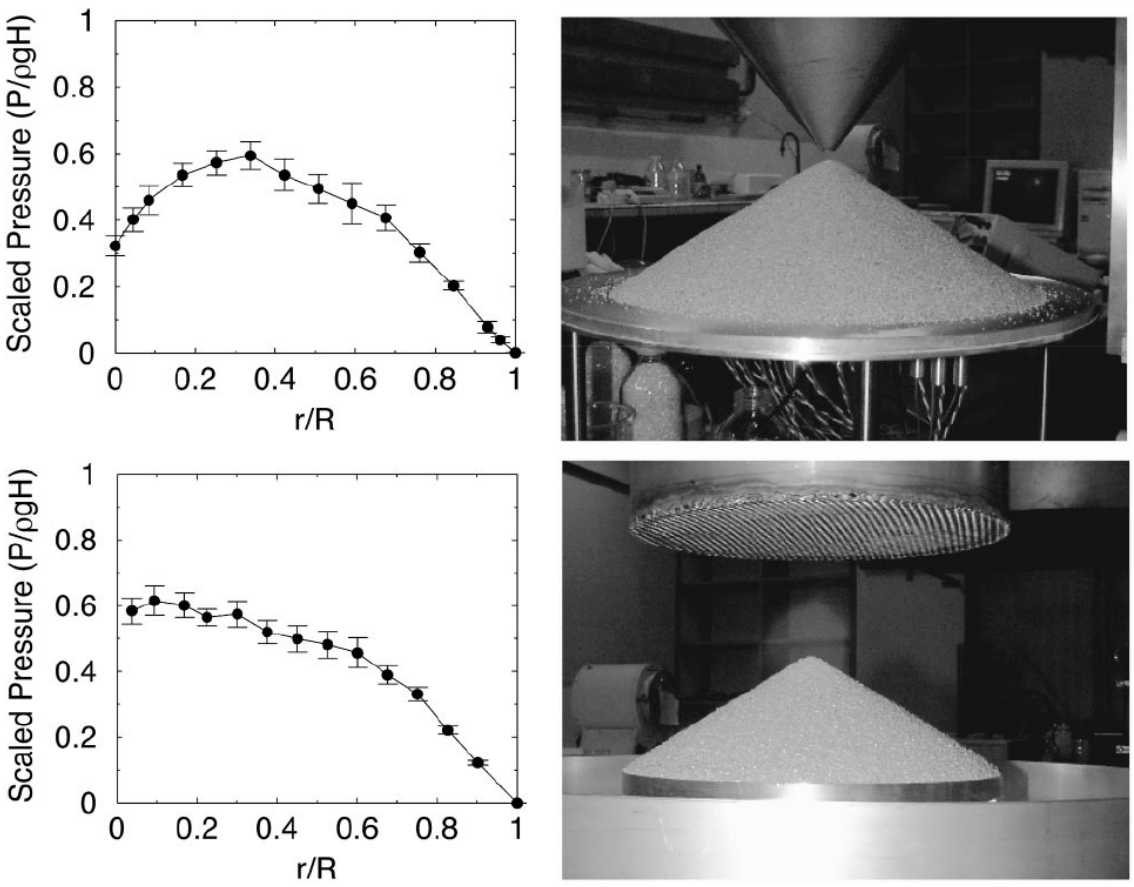

Figure 2.2: Dimensionless normal stress profiles versus dimensionless radial distance, beneath conical piles of granular materials of height H and radius R. The construction techniques are illustrated by the accompanying photographs [41].

granular material in these regimes is very different and the transitions from one to the other regime is not fully defined, there is not yet a single theory, which is able to fully describe the granular behavior.

2.1.2 History

Not only the granular density and temperature influence the behavior of a granular system, but also the history of its preparation. It is not yet known, to what extent the granular packing history is relevant and, if so, how to include it in theories of compaction or stress patterns within the medium [22]. There have been experiments studying the effect of construction history on static stress distributions [41]. In such experiments a sand pile has been prepared with two different methods: i) a "localized source" procedure using a hopper, ii) a "raining procedure" using a sieve (Fig. 2.2). The normal forces were measured under each pile locally. It was observed

that depending on the preparation method, the normal stress profiles as a function of radial distance from the center behave very differently. While a pressure dip exists at the center of the pile prepared with a localized source, in the case of the more homogeneously prepared pile the dip is missing. It seems, as if the progressive formation of the pile by successive small avalanches causes the pressure dip [41].

The "memory" of granular systems could be reasoned as follows [42]: The granular systems are built up gradually and the last particles added to the system influence just the particles surrounding them and the structure of the rest of the system remains unchanged.

2.1.3 Segregation

When agitation is imposed on a granular system composed of particles with size polydispersity [5] or with different shapes [43, 44], densities [45] or even with different microscopical properties like friction [46] or restitution coefficient [47], these particles may start to get separated according to their different properties. This phenomenon is called *segregation*. The agitation source could e.g. be shearing [48–50], tapping [51] or shaking [46].

Different studies have shown that the size polydispersity plays the most important role in segregation [5]. While the microscopic friction coefficient and the gravity are crucial in dense regimes with lasting contacts, the density of particles and the restitution coefficient are more relevant in dilute regimes with binary collisions [52, 53]. In experiments with vertically shaken systems, Knight *et al.* found a direct link between convection and size separation. In many industries, segregation of the flowing particles due to high size polydispersity of the particles causes some problems. This influences for example the desired homogeneous flow down the inclined plane [6]. The vertical size segregation of granular materials is usually associated with the Brazil-nut effect and is assumed to proceed faster for larger size differences between particles [49, 54]. However, more recent studies give more insight into the other dependencies of this phenomenon.

Golick *et al.* [49] investigate in their new experiments the mixing and subsequent resegregation of a dense granular material under shear. The mixing and segregation rates are measured as a function of particle size ratio and confining pressure. The mixing rate is observed to decrease as particles become more similar in size. This corresponds to the expected kinetic sieving behavior, whereby small particles filter

down through a fluctuating "sieve" of large particles. The resegregation rates, however, are observed to be nonmonotonic in particle size ratio, in contrast to kinetic sieving theory, and strongly depend on the confining pressure. The latter is more pronounced for contrasting rather than similar particle sizes. For small particle size ratio, Golick *et al.* propose the slow segregation rate to be influenced by the presence of a large-particle-dominated force chain network at larger pressures as well as the increased packing fraction for mixtures of dissimilar particle sizes. Recently, Fan *et al.* [50] observed phase transitions in shear-induced segregation of granular materials in their computational study. While for low solid fractions, large particles segregate towards regions of low shear rates with low granular temperature, this trend reverses with increasing solid fraction, and large particles segregate toward regions of high shear rates and temperatures.

2.1.4 Jamming

Dry granular materials are collections of particles that interact through repulsive and frictional contact forces. As stated in Sec. 2.1 the thermal energy is negligible in comparison to the gravitational energy. Consequently, without an external energy supply, these materials get jammed into a disordered configuration, even under the action of a small confining pressure [55]. When jammed, the disordered system is caught in a small region of phase space with no possibility of escape [56]. In solids, the mechanical stability implies a finite resistance to shear and isotropic deformation. Such stability originates essentially from long-range crystalline order. How the mechanical stability is satisfied in disordered systems is still an interesting question to be answered [57]. There are different studies trying to develop models to explain this stability. Cates *et al.* connect the appearance of jamming with the formation of force chains along the compression direction. Such an array or network of force chains can support the shear stress indefinitely [58]. However, the fundamental difference to the ordinary solids is that, if the direction of the applied stress changes even by a small amount, then the jam will break up and the chains will fall apart [58]. Cates *et al.* call the jammed disordered material "fragile matter".

O'Hern *et al.* [59] have shown a connection between the development of a yield stress, either by a glass transition or conventional jamming transition, and the appearance of a peak in the force distribution P(F) (see Sec. 2.2.3). For four different modeled supercooled liquids, they have observed this peak by decreasing temperature below the glass transition, by decreasing shear stress from the flowing state and also by increasing density from the liquid state at fixed temperatures (Fig. 2.3). Static

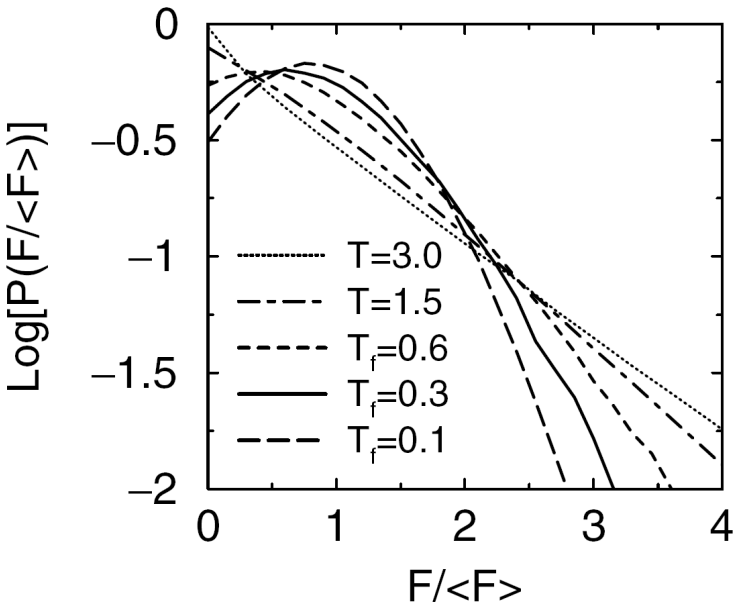

Figure 2.3: $P(F/\langle F\rangle)$ for all interparticle force pairs versus $F/\langle F\rangle$ for a purely repulsive potential for two equilibrium temperatures T above and three (T_f, final temperature after a quench) below T_g (temperature at glass transition) [59].

granular packings exhibit the same behavior by varying the three parameters temperature, shear stress and density. They propose that the appearance of this peak signals the development of a yield stress. The sensitivity of the peak to temperature, shear stress, and density confirms the proposed generalized jamming phase diagram by Liu and Nagel [56] (Fig. 2.4). According to Fig. 2.4, jamming can occur only when the density is high enough. One can then unjam the system either by raising the temperature or by applying a stress.

There are different works studying the jamming transition by changing the shear stress. da Cruz has studied both shear rate and shear stress controlled Couette flows [60]. If the shear rate is controlled, the flow becomes intermittent in the quasistatic regime. In contrast, with shear stress being controlled, he shows that the jamming transition between the quasistatic and the dynamic regimes is discontinuous, hysteretic and presents strong similarities with the transition observed in thixotropic fluids. He shows also a discontinuous transition of the contact network during jamming and proposes a model of the jamming, based on the trapping of the grains induced by the wall roughness.

Silbert *et al.* [61] have studied the dynamic jamming transition of systems of athermal grains through large-scale simulations of dense packings of soft particles flowing down a rough, inclined plane. The fraction of sliding contacts has been measured in these simulations as a function of the tilt angle of the inclined plane. This fraction decreases

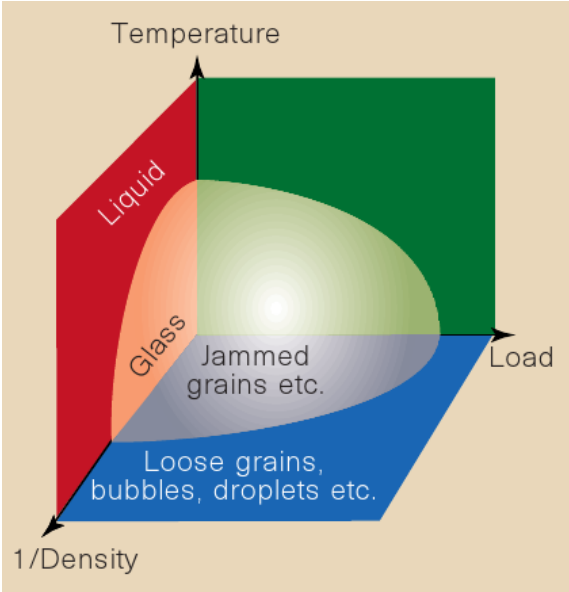

Figure 2.4: A possible phase diagram for jamming. The jammed region, near the origin, is enclosed by the depicted surface. The line in the temperature-load plane is speculative, and indicates how the yield stress might vary for jammed systems in which there is thermal motion [56].

with decreasing angle towards a critical angle at which jamming happens. Below this critical angle, the packing is static and almost no contact slides. This transition has characteristics similar to a thermally driven glass transition.

2.2 Contact and Force Networks

Not only flowing granular material exhibits different behavior than fluids, but also granular material at rest can be a source of anomalous behavior. For normal fluid held in a container, the pressure at the bottom of the container increases linearly with the filling height. In the case of granular matter, in contrast, the pressure at the bottom grows linearly for small filling heights, reaches a maximum value after a certain height is exceeded and above that the pressure saturates. With increasing height, due to the contact forces between the grains and the static friction between the particles and the side walls of the container, the extra weight of the filling is supported by the walls [22, 62]. This phenomenon is called "Janssen effect" and is based on arching, which is a direct consequence of force chains in a granular packing [63, 64]. A static granular packing has the tendency to build up force chains, supporting the overlying material.

In a dense granular packing, the contact forces are transferred through the contacts between the particles. The contact network acts as the skeleton of a granular packing and is the key factor determining its mechanical properties [65]. For a disordered distribution of contact points, while the contact network is essentially homogeneous in large scales, the force network could be strongly inhomogeneous [22, 65] (Fig. 2.5). Getting a better knowledge of contact forces and their spatial correlations, specially in response to external forces and deformations at the system boundaries, is a fundamental goal of granular mechanics, being relevant to civil engineering, geophysics and physics. This knowledge is important for the understanding of e.g. jamming, shear-induced yielding and mechanical response [66].

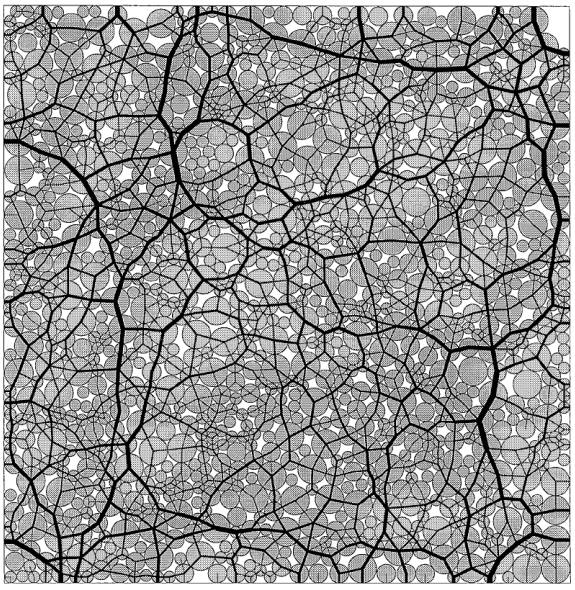

Figure 2.5: Force network of static granular matter is inhomogeneous in space. In this figure, grains are represented as grey disks and forces as bonds. The thickness of each bond is proportional to the magnitude of the contact force [67].

2.2.1 Measurement

The early experiments to investigate the contact force network had been done with very simple experimental setups. In these experiments, carbon paper has been placed between the boundary walls and the bulk material to make marks proportional to the applied normal local forces [68–70]. This setup makes the contact force measurements possible in 2D and 3D, but just at the boundaries of the system.

An alternative recent method uses particles made of photoelastic material in a 2D setup to visualize the contact network in the bulk of the packing at the grain scale. The photoelastic particles display stress-induced birefringence in response to applied

forces. Using an arrangement of circular polarizers, it is possible to characterize the stress on the particles [71–73] (Fig. 2.6). Extracting individual contact forces from the stress pattern of the granular packing is, however, a very complicated task, which was recently solved successfully [66].

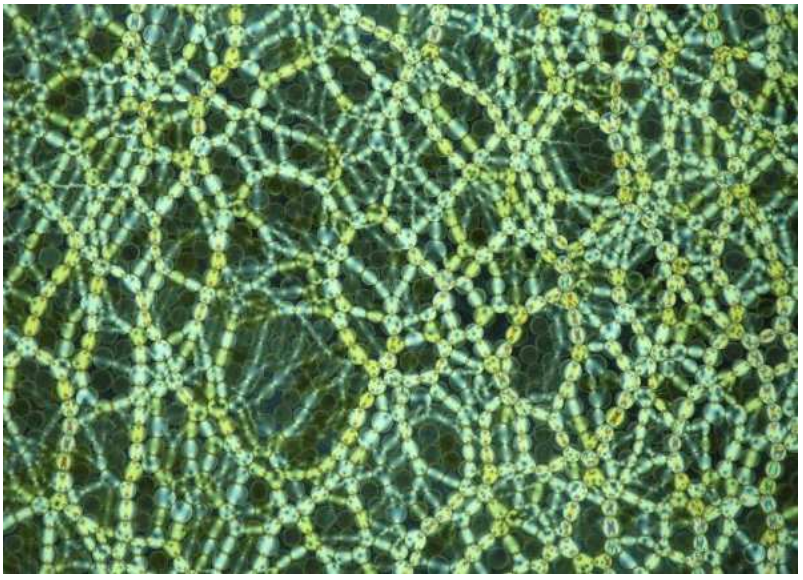

Figure 2.6: Photoelastic visualization of contact force network in a granular packing [74].

Until now, the only method to determine the contact force network in the bulk of a 3D packing is doing simulations. In contrast to the complex experimental setups with the limited choice of parameters for the grain properties, the simulations make a broad range of parameters possible. Moreover, the resolution of contact force measurement for small contact forces is much higher in simulations. However, developing realistic numerical simulations is a great challenge. There are different simulation methods amongst others, trying to mimic the real behavior of granular material. An overview of these methods will be presented in chapter 4.

2.2.2 Coordination Number

Solid fraction ν in a granular packing is defined as the ratio between the occupied volume to the whole volume including the pores. This quantity provides simple information about the packing structure [75]. In many studies, local measurements of ν with high resolution deliver valuable information about the structure of the packing specially near the boundaries [34, 76]. Moreover the variation of the mean solid fraction with the dimensionless shear rate (see Eq. (3.3)) in granular systems obeys a global constitutive law independent of microscopic properties and system geometry (see Sec. 3.6.1).

Regarding the fact that all interactions in a dry granular packing take place at contact points, one could think of defining another quantity known as *coordination number*. In a packing of granular material, the coordination number Z is equivalent to the number of touching neighbors per particle $Z = 2N_c/N$. Z is an important quantity, because the amount of contacts between particles in a pile provides the necessary mechanical constraints to ensure its stability [77]. Z increases monotonically with decreasing dimensionless shear rate (decreasing shear rate or increasing pressure, according to Eq. (3.3)) to its maximum value in a jammed static packing. Not only Z at a finite dimensionless shear rate, but also its maximum value in a static packing depends on the microscopic particle properties like the microscopic friction coefficient and the stiffness of the particles [29, 78].

2.2.3 Contact Force Distribution

In Figs. 2.5 and 2.6 one can recognize a mixed structure with thick chains connected with thinner cross lines. For a compressed granular packing, Radjai *et al.* distinguish between the "strong" force network with contact forces greater than the average normal contact force, and the "weak" force network with contact forces smaller than the average [79]. The strong force network carries the load in the whole structure and the weak subnetwork is dissipative and contributes just to the average pressure. While the strong network is comprised of pure sticking contacts, nearly the whole dissipation happens due to sliding in the weak subnetwork [80].

To make statistical study of these two networks, the histogram of the measured normal forces has to be plotted. After normalizing the force N by its mean value $\langle N \rangle$, the probability distribution function P of $N/\langle N \rangle$ would be obtained. The first studies in this direction have analyzed the results of experiments [69, 70, 73, 81, 82]. Most of the experiments are able just to measure the contact force distribution of strong forces ($N > \langle N \rangle$) [70, 73, 81]. However, only the more sensitive methods measure also the contact force distribution of weak forces ($N < \langle N \rangle$) [69, 82]. There have been also numerous numerical simulations attempting to study the probability distribution function of contact forces [67, 83, 84]. The advantage of numerical simulations to the experiments could be summarized as follows: i) the contact force distribution of weak forces could also be measured, ii) not only the normal forces, but also the tangential forces could be measured with high precision and iii) one could study 3D structures and take the contacts in the bulk of the packing for such analysis into account. The general trend of the probability distribution function P stays, however, very similar to the experimental results. P decreases exponentially

for strong forces, while it follows a power law with a negative exponent for weak forces.

$$P(N) = \begin{cases} k\left(\frac{N}{\langle N\rangle}\right)^{-\alpha} & N < \langle N\rangle \\ ke^{\beta\ (1-\frac{N}{\langle N\rangle})} & N > \langle N\rangle \end{cases} \tag{2.4}$$

where k is determined by normalization as:

$$\frac{1}{k} = \frac{1}{1-\alpha} + \frac{1}{\beta} \tag{2.5}$$

The weak forces, comprising nearly 60% of contacts, are more frequent than the mean force itself [84] (see also Fig. 4.6). The results remain very similar for frictionless particles [85] and in sheared systems [86]. However, the detailed study of Silbert *et al.* [80] shows that the probability distribution function P for weak forces depends on the microscopic friction coefficient between the particles.

2.2.4 Distribution of Contact Orientation

Another microscopic quantity is the statistical orientation of the contact directions $P(\theta)$. This quantity is specially interesting to study sheared systems, which show anisotropy in the angular distributions of both contact and force networks (Fig. 2.7). While isotropically compressed systems have short-range correlations regardless of the direction, sheared systems have long-range correlations in the direction of force chains [66].

Given a static packing with a homogeneous contact network, with increasing applied shear stress, strong contact forces orient in a preferred direction, and the contact force network becomes more and more anisotropic. Finally, the packing can not further sustain the shear stress and starts to flow at a threshold shear stress. Simultaneously, more and more contacts open in the shear direction and new ones form in the perpendicular direction. Consequently, the anisotropy of $P(\theta)$ also increases [87, 88].

Distinguishing between strong and weak contacts (Sec. 2.2.3), one could plot the angular distribution of these contacts separately. As the role of the strong force network is to carry the external load imposed on the system, the distribution of strong contacts is also sensitive to the applied forces. To study this effect, a two-dimensional system of particles confined in a rectangular box, is biaxially compressed

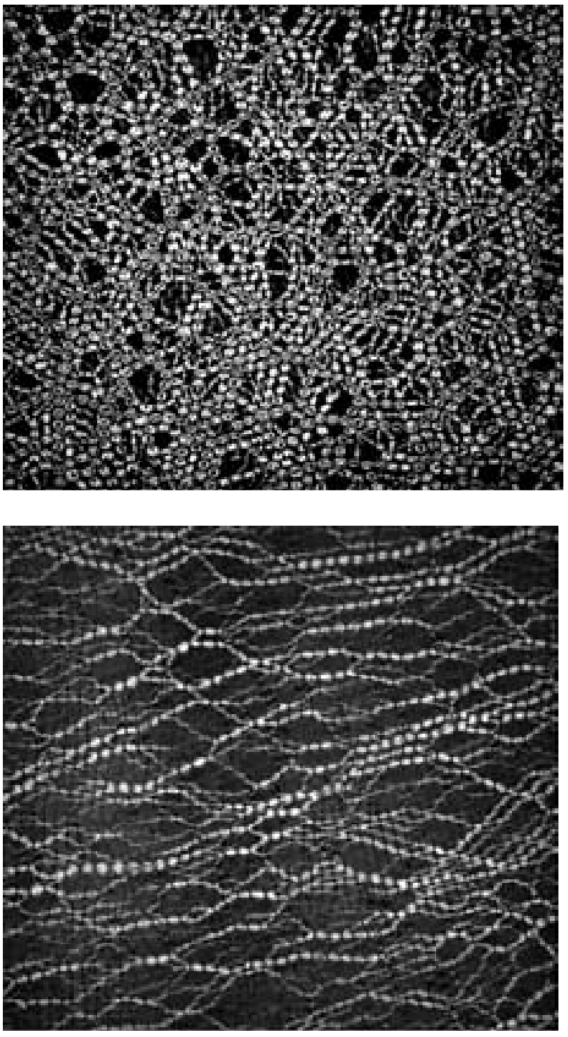

Figure 2.7: Images of an isotropically compressed state (top) and a sheared state (bottom) [66].

[79]. Consequently, strong contacts are preferentially oriented parallel to the axis of compression, while for weak contacts, the direction of anisotropy is orthogonal to the axis of compression (Fig. 2.8). The strong contact distribution is highly anisotropic and the weak contacts are distributed in a more isotropic way. Although the strong contacts build up less than 40% of the contacts, their positive contribution overcompensates the negative contribution of the weak contacts and they support the whole deviatoric load [79].

The distribution of contact normal orientations $P(\theta)$ is a π-periodic function and its Fourier expansion with a truncation at second order

$$P(\theta) = \frac{1}{\pi}\{1 + a\cos(2\theta - 2\theta_F)\} + h.o.t., \tag{2.6}$$

is a good empirical fit for this polar histogram, which includes information about the

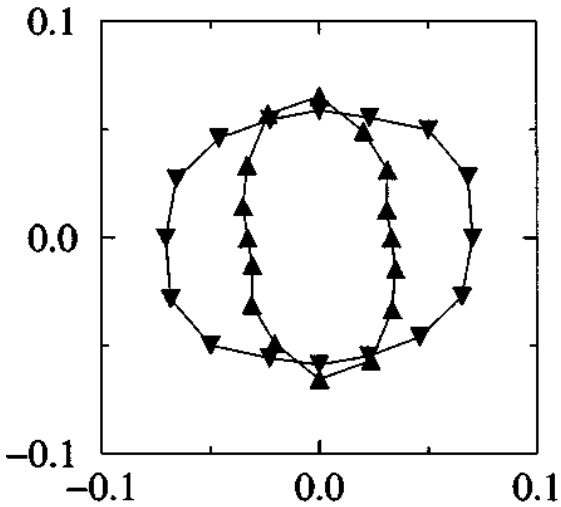

Figure 2.8: The polar diagrams of the probability density of contact directions for weak (▼) and strong (▲) contacts during a biaxial compression [79]. While strong contacts are preferentially oriented parallel to the axis of compression, for weak contacts the direction of anisotropy is orthogonal to the axis of compression and the diagram is indeed more isotropic.

internal structure of the system (for the definition of θ_F, see below). To encode the microscopic information from this function, several tensors have been introduced. The simplest of them is the *fabric tensor*. Scalar parameters like solid fraction and coordination number (see Sec. 2.2.2) are unable to describe the state of a granular packing, which is not only sensitive to the magnitude of shear, but also to its orientation. This requires at least a second-order tensor to be defined. Fabric tensor defined as the volume average of the dyadic tensor product of contact normals $\mathbf{F} = \langle \vec{n} \otimes \vec{n} \rangle$ delivers higher-order microstructural information [75]. Normalizing the fabric tensor by the number of particles results in:

$$tr(\mathbf{F}) \propto Z, \tag{2.7}$$

where Z is the mean coordination number (Sec. 2.2.2).

Neglecting second and higher order terms in the Fourier expansion of $P(\theta)$ (Eq. (2.6)), one could find a connection to the fabric tensor: The major principal direction of $\mathbf{F}$ is θ_F and the deviatoric part of $\mathbf{F}$ is $(a/2)tr(\mathbf{F})$ [75].

2.2.5 Compactness and Influence of Friction

The investigation of the coordination number in a system at the jamming transition with interparticle friction coefficient has attracted considerable attention. For a

static packing consisting of frictional particles, not just a single solution, but an ensemble of force networks exists, which provide mechanical equilibrium under the given external load and satisfy the Coulomb condition at every contact [89]. There exist two extreme cases, at which a static packing at the jamming transition point is "isostatic" (the number of equilibrium equations is equal to the number of unknowns): i) frictionless particles and ii) the limit of $\mu \to \infty$. The critical average coordination number Z_c for these two cases is $Z_c = 2D$ and $Z_c = D + 1$ respectively (D is the dimension of the system) [90]. Between these two states, Z depends strongly on the friction coefficient μ and decreases with increasing μ smoothly and monotonically in 2D from $Z = 4.0$ to $Z = 3.0$ (Fig. 2.9). The behavior of the packing fraction ν is similar to that of Z, with $\nu = 0.84$ in the limit of frictionless particles and $\nu = 0.80$ in the limit of $\mu \to \infty$ [91].

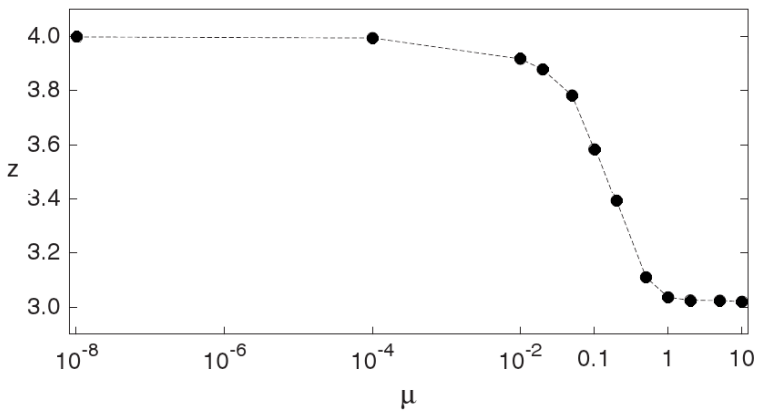

Figure 2.9: Influence of friction on the coordination number Z [91].

Another approach to define the coordination number is to take just the number of force carrying particles into account. With this approach, Shaebani *et al.* [89] have compared the behavior of Z in two packings prepared with different methods: i) homogeneous compaction and ii) compaction by gravity. This definition helps to exclude rattlers in zero gravity and reduces the deviation of Z at finite μ calculated for both packings.

2.2.6 Mobilization of Friction

As mentioned in Sec. 2.2.3 the strong force network carries the load in the whole structure and the weak subnetwork is dissipative and contributes just to the average pressure. While the strong network is comprised of pure sticking contacts, nearly the whole dissipation happens due to sliding in the weak subnetwork. Another fundamental aspect of granular packings behavior is the intergrain friction. While force chains

are responsible for the stability of granular packing, ensuring its mechanical strength, frictional contacts result in local instabilities and constitute a threat to stability [9]. One could define the *mobilization of friction* at each contact, measured by the ratio of the tangential to the normal force times the inverse of microscopic coefficient of friction, as follows:

$$\eta = \frac{1}{\mu}\frac{F_T}{F_N} \tag{2.8}$$

η varies between 0 and 1 and for $\eta = 1$ the contact is sliding ($F_T = \mu F_N$). One could study the angular distribution of η to find connections to the contact normal orientations for the stability analysis as done in [9]. Another approach is to consider just the fully mobilized contacts $\eta = 1$ and define a coordination number for sliding contacts Z_s. According to this definition Z_s is the average number of sliding contacts per particle. Dividing Z_s by Z (equivalent to the ratio between the sliding contacts and the total number of contacts) the quantity *mobilization* M is defined, which could be used for global statistical analysis [10]. da Cruz *et al.* [29] have studied the variation of M as a function of dimensionless shear rate and found a master curve of $M(I)$ independent of microscopic packing properties. One could also measure M locally in inhomogeneous systems to perform stability analysis.

3 Sheared Granular Materials

3.1 Granular Flow

The dissipative nature of collisions between the elements of a granular material drives the system towards a compact one in the absence of an external source of kinetic energy. Upon increasing external driving forces, the system yields and starts to flow. Depending on the amount of energy pumped into the system and the density of the packing, one may deal with a granular fluid or gas. Avalanches, movement of earth's tectonic plates, dune formation, river sedimentation and planetary ring dynamics are few examples of granular flow observed in nature. Flow of granular materials is fundamentally different from that of any molecular gas. One special characteristic of granular flow is clustering that originates from the presence of inelastic collisions and friction between the grains. There are different ways to drive a granular packing. The granular flow can be initiated e.g. by gravity [4, 6, 92], an interstitial fluid or gas [24, 93], shearing [25, 87, 94], shaking [95, 96] or compaction [26, 97]. Although throughout this work the results of planar shearing with smooth walls are presented, in this chapter common shear geometries are introduced and some characteristics of shear flow are elucidated.

3.2 Shear Induced Flow

Granular materials are often sheared in nature and industry. Understanding of the mechanisms of shear induced flow in granular systems is of great interest for geophysicists, to get more insight into geological phenomena e.g. rupture or earthquake [1]. Shear mostly initiates from moving boundaries, where there exists a relative velocity between the confining boundaries and the bulk material.

3.2.1 Newtonian Fluid

A Newtonian fluid is a simple ideal fluid, in which the stress at any point is proportional to the time rate of strain at that point; the proportionality factor is the viscosity coefficient. In such a flow, the viscosity coefficient is constant for different shear rates and does not change with time.

For a laminar flow of a Newtonian fluid along a wall in x-direction (Fig. 3.1), the fluid layers slide over each other in the $x - z$ plane, which gives rise to a shear force F_x (tangential friction force), for which the Newtonian ansatz is valid:

$$F_x = \eta A_{xz} \frac{dV_x}{dy}, \tag{3.1}$$

leading to:

$$\tau = \frac{F_x}{A_{xz}} = \eta \frac{dV_x}{dy}, \tag{3.2}$$

in which η is the viscosity coefficient, A_{xz} is the surface area, $\frac{dV_x}{dy}$ is the yx-component of the velocity gradient, and τ is the shear stress. Assuming a constant F_x, the velocity gradient remains also constant over time, which leads to a linear velocity profile [98].

3.2.2 Shearing of Granular Materials

Shear Localization

When a system composed of a granular matter is sheared, the spatial distribution of the shear rate is generally nonhomogeneous. Most of the time, shear is localized near the system boundaries in a region referred to as *shear band*. The width of shear bands amounts to a few particle diameters, and the velocity profile decays typically exponentially outside the shear band. Depending on the boundary conditions, confining pressure and shear velocity, apart from a few layers close to the boundaries, the bulk of the granular system could exhibit different behaviors: i) for high shear velocities and small confining pressures, the granular matter is fluidized and, on average, homogeneously sheared. Keeping the distance between the shearing walls constant, granular gases with very small filling densities could also be sheared homogeneously [99]. ii) For small shear velocities and high confining pressures, the shear is not ho-

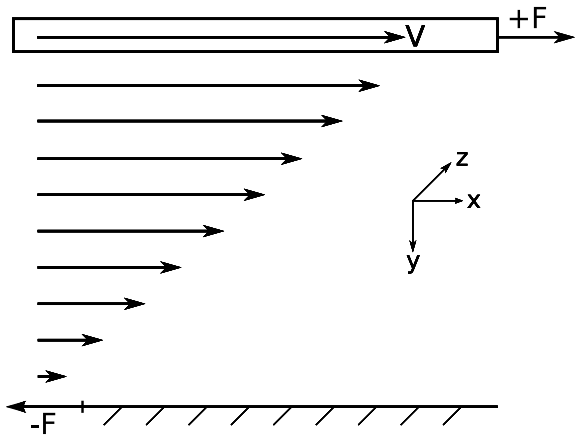

Figure 3.1: In a Newtonian flow the shear stress at any point is proportional to the time rate of strain at that point. The figure depicts an example, where the Newtonian fluid is confined between a fixed and a moving plate of velocity V. The arrows show the velocity profile in the system.

mogeneous and solid and fluid phases coexist [1, 23]. Such a behavior of granular materials has not yet been fully understood and no consistent and general formalism can predict it successfully.

Shear localization has been one of the interesting subjects in the research area of sheared granular matter. Several systems with various boundary conditions and microscopic properties have been considered to facilitate the understanding of this effect [100–105]. There are also theoretical studies within the scope of Cosserat-theory [106] and those based on the gradient dependent dilatancy, implemented in the flow theories of plasticity [107]. Although these two approaches are based on different physical assumptions, both of them proof the necessity of existence of shear bands and calculate their thickness. In contrast to DEM simulations and theoretical studies, the study of shear band structure with experimental methods is rather difficult. The visualization of the granular interface is usually limited to the upper (free surface) or bottom layers (through a transparent glass window). Recently, MRI has been used to study the granular rheology (velocity and solid fraction profiles) inside the granular system [108].

Slip Velocity

The influence of boundaries on the rheology of granular flow has always been an important part of research [18–21, 32–34]. Velocity slip at the boundaries is one of the characteristics of granular flows [21]: the granular material in the vicinity of the boundary does not take the boundary velocity. The difference between the boundary

velocity and the mean velocity of the granular material adjacent to the boundary is defined as *the slip velocity*. While the existence of a finite slip velocity at the wall in fluids has been neglected for a long time [109], it gained attention in granular flow rather quickly [21]. Slip at the boundaries is not often desired, though, and in lots of experiments boundaries are roughened using sandpaper [32] or glued beads [33] in order to efficiently transfer momentum and energy to the flow [20]. Even in most of the recent numerical studies, rough boundaries are favored, as they intuitively produce less velocity slip and therefore a larger shear rate [21, 29, 34, 110]. Boundary conditions, which involve slip are important to understand the granular flows properly, though [20, 21, 35].

3.3 Shear Geometries

There are different shear geometries, which are commonly used to study the macroscopic properties of granular flow. A list of some well-established geometries is presented in Fig. 3.2 [39]. In this section, a brief overview of these different geometries is presented to give an insight into their flow properties and applications.

Planar shear (Fig. 3.2 (a)) is one of the simplest geometries. The granular material is confined between two parallel walls (usually rough ones) with a prescribed pressure or distance. More about this geometry could be found in Sec. 3.4. Cylindrical Couette cell (Fig. 3.2 (b)), known also as annular Couette cell, is another confining geometry. It is a proper geometry for experiments, because of its periodicity conditioned by its shape. Mostly, the inner cylinder rotates and the outer one is fixed. In different realizations of this geometry, the bottom plate rotates either with the inner cylinder or is fixed [111]. Some geometries are confined at the top and some others have a free surface. The distance between the two cylinders is usually kept constant, however, recently Koval *et al.* have constructed an annular Couette cell surrounded by a flexible membrane, allowing for a prescribed radial pressure rather than a prescribed distance in this direction [76, 112]. Vertical silo driven under gravity (Fig. 3.2 (c)) is another confined geometry, which is important for technical applications. In all confined geometries, the shear bands are localized in a thin layer of 5 to 10 particle diameters in the vicinity of the moving wall. Local rheology is understood to a wide extent in the fluidized regime in these geometries. However, by decreasing shear velocity, the former local rheology can not capture the quasistatic regime [39].

The configurations introduced in Figs. 3.2 (d)-(f) have a fundamental difference to

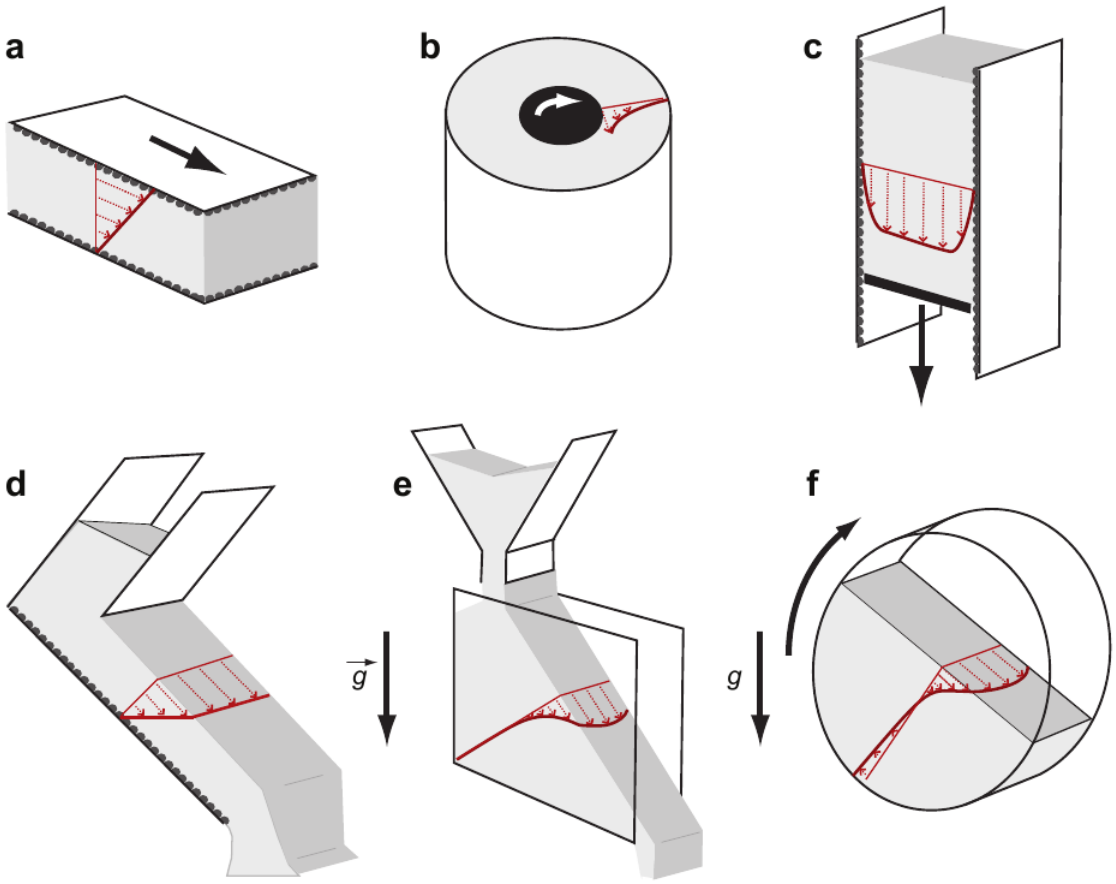

Figure 3.2: Different flow configurations: (a) planar shear, (b) Couette cell, (c) vertical silo, (d) inclined plane, (e) flow on a pile, and (f) rotating drum [39].

the first three ones, as they all have a free surface and thus are not confined geometries. Inclined plane (Fig. 3.2 (d)) is one of the most important geometries, studied both numerically and experimentally due to its practical applications. In contrast to the static threshold of motion on an inclined plane, which is well investigated experimentally and numerically, the dynamic case is not fully understood. For the case of steady uniform flow, the volume fraction is constant throughout the layer and the shape of the velocity profiles is derived for the limit of very thick and thin layers [113].

Granular pile flow (Fig. 3.2 (e)) is the geometry used to study the avalanche phenomenon. In contrast to ordinary fluids, granular materials form piles with an inclined surface. As soon as a critical angle is exceeded, the pile cannot sustain the steep surface and an avalanche occurs. At first glance, the avalanche seems to be composed of a superficial flowing layer, with a "frozen" bulk region below. In fact, the velocity profile is approximately linear in the upper region, followed by an exponential creeping tail below [114]. The only control parameter is the injection flow rate in this geometry [39]. The sidewalls confine the flow laterally and their friction influences the stability of the steep pile [115]. Rotating drum (Fig. 3.2 (f)) is much more com-

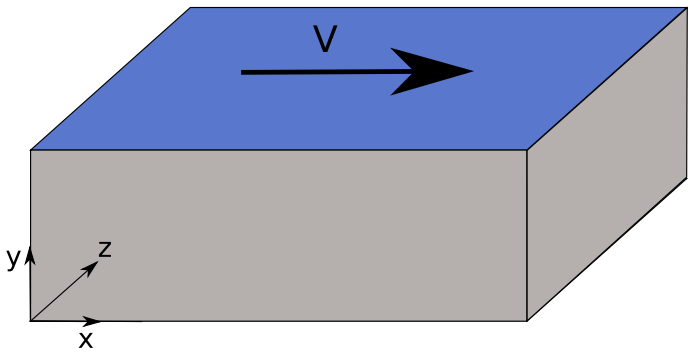

Figure 3.3: Planar shear geometry with confining shearing walls perpendicular to y direction and shear velocity V in x direction with periodic boundary conditions. In z direction either periodic boundary conditions or confining walls could be applied.

plex than the other geometries explained above, as the flow is highly nonuniform. Though the experimental setups are very thin and the side wall friction influences the flow strongly, local rheology derived for planar shear is applicable to this system.

3.4 Boundaries in Planar Shear

Planar shear (Fig. 3.3) is one of the simplest shear geometries to study the granular flow properties. This geometry consists of two confining shearing walls at the top and bottom of the system. In the numerical simulations, periodic boundary conditions are imposed in shear direction (x). In 3D systems one could set periodic boundary conditions perpendicular to the shear direction as well (z direction). Alternatively, the flow could be confined with walls in this direction.

Depending on the boundary conditions in this simple geometry, one could perform a large variety of simulations showing the different features of granular shear flow. In the following, some of the common planar systems are introduced.

3.4.1 Shearing with Smooth Walls

One possibility to construct a planar shear system is to use smooth walls, without any roughness. In a planar system with smooth walls, the rotational velocity of the particles increases towards the shearing walls. The smooth walls drive not only the center of mass velocity, but also the rotational velocity around the center of mass of the particles. Since not all particles build a sticking contact with the walls, there

exists slipping at the walls, even if we consider the rotational velocity of the particles to calculate the average velocity at the walls. Considering just the center of mass velocity of the particles to calculate the slip velocity at the walls, it amounts even to the same order of magnitude as the shear velocity. Campbell performed computer simulations to study shear properties of two-dimensional systems of elastic disks with smooth walls [18, 116]. He studied particle rotation at smooth walls and proposed two rotation induction mechanisms, transferring rotation into the bulk of the granular system [18]. In the first mechanism (Fig. 3.4 (a)) the velocity gradient towards the center of the system generates clockwise rotations in the particles through particle binary collisions (faster from above and behind and slower from below and front). Fig. 3.4 (b) shows the rotation transfer, induced directly at the walls. The particles in contact with walls gain a high angular velocity, which in turn induce a counter rotation in the next layer. The particles in this second layer induce again a counter rotation in the next layer, until the wall effect vanishes and gives way to the first mechanism.

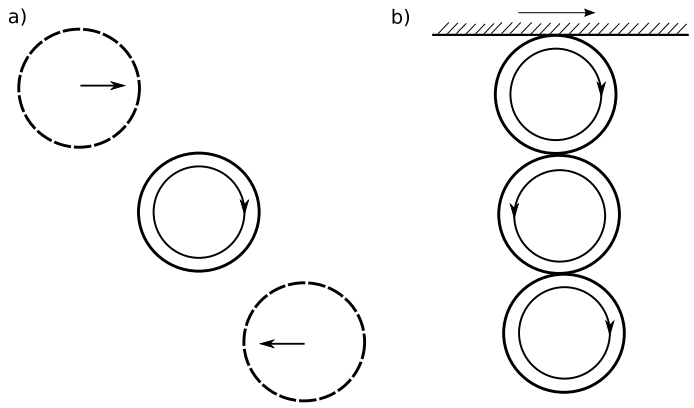

Figure 3.4: Two rotation induction mechanisms, which transfer rotation into the bulk of the granular system [18].

The solid fraction in the systems studied by Campbell (ν_{max}=0.65) are smaller than the very compact systems ($\nu \simeq 0.85$), which allows for simulations with monodisperse materials and results in larger penetration of wall induced effects. Though he presents some examples on the influence of the microscopic friction coefficient on the shear properties, this issue has not been addressed in his work extensively. J. P. Bardet and J. Proubet [101, 102] have also studied the structure of persistent shear bands with numerical simulations. The rotation distribution of particles in shear bands and their neighboring layers have been used to determine the position and the thickness of shear bands.

Smooth boundaries (with much smaller asperities compared to the particles in the bulk) occur frequently in nature and in industry for particles in the millimeter regime and above, and hence are not just an academic idealization.

3.4.2 Shearing with Rough Walls

In almost all shear geometries, rough walls are used to avoid slip at the walls and to induce larger and more homogeneous shear rates. In such cases, almost homogeneous shearing has been reported at moderate shear velocities. In planar shear systems with rough walls, the rotation of the particles is frustrated directly at the walls. The center of mass velocity of these particles in contrast takes almost the wall velocity [21, 29, 34, 110]. Although experiments provided data about the increased shear stresses through roughening [32, 33] in the eighties, more detailed and accurate studies were performed for the first time through computer simulations much later (since the nineties by DEM simulations [18–21] and recently by continuum simulations (GKL) [3]), providing information about the stresses at the boundary and in the interior of the flow with different boundary conditions. Earlier, there have also been theories devised on the subject, i.e. trying to find a relation between the transferred momentum into the flow and the boundary properties [15–17, 117]. While some of them concentrate solely on rough, frictionless walls and others on smooth, frictional ones, almost all of them (namely the continuum descriptions) consider the rapid dilute flow [17–20]. Such theories are not applicable to the dense granular flow, though.

Campbell has compared the shear properties of smooth and rough frictional walls with computer simulations of two-dimensional systems of elastic disks [18, 19, 116]. Though rough walls are usually considered as those with particles glued on their surface, the classification of boundaries as "smooth" and "rough" is not really straightforward [21]. In most of molecular dynamics simulations, rough walls consist of a chain of polydisperse or even monodisperse particles without any spacing between them [21, 29, 34, 110]. In other works, in contrast, such walls are classified as "flat" boundaries and they claim that the walls could only be considered as rough, when large spacings (considering the density of the flow) exist between the roughening particles [19, 21, 118].

First studies, concerning the influence of roughness on dense granular flows started with the problem of granular flow down inclined planes [6]. In many industries, segregation of the flowing materials due to their high size polydispersity causes some problems. This prevents e.g. the desired homogeneous flow down the inclined plane; while the larger particles find their way to the bottom of the plane, the small particles are stopped farther uphill [6]. To get the first insights into the problem of steady state flow down an inclined plane, S. Dippel *et al.* have studied the motion of a single disk on an inclined plane consisting of smaller disks separated with regular as well

as with random spacings, in 2D both with a stochastic model [6] and by means of MD simulations [119] and in 3D with MD simulations [120–122]. Simulations with a large number of monodisperse particles [123] in 2D and 3D and those with bidisperse assemblies [31] have shown that in the limit of large roughness in steady state the friction force acting on the moving particle on the rough surface is independent of material properties such as microscopic friction coefficient and the restitution coefficient. In contrast, the characteristics of motion rather depend strongly on the ratio of the moving particle size to that of the roughening particles as well as on the spacing between them [6, 119–125]. According to the geometry of contacts at rough walls, the friction mobilization tends to increase, when shearing with rough walls [34]. Bulk particles are trapped between the roughening particles and the normal forces at the contact points drive the flow. Hence, the tangential components of the contact forces are not important. They become important in the limit of small roughness, when they, inducing rotation of the particles in the neighborhood of the walls, drive the flow [34]. All these results are in accordance with experimental investigations [124, 125] and with the simple models developed to understand the influence of boundaries on the flow [6, 123].

3.4.3 Lees-Edwards Boundary Conditions

There exist alternative approaches, in which the driving device is eliminated to focus solely on the intrinsic properties of the material [126, 127] by using Lees-Edwards boundary conditions [128]. In the setup of Fig. 3.3, this would mean to remove the flat walls and to set periodic boundary conditions also in y direction.

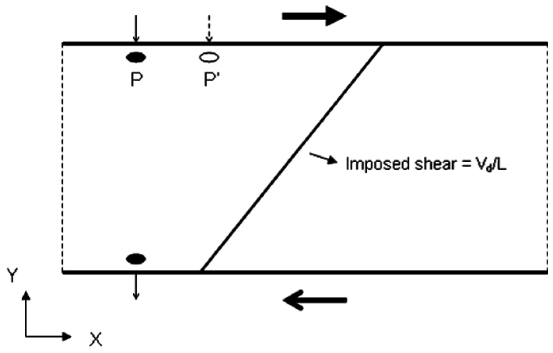

Figure 3.5: Lees-Edwards periodic boundary condition for constant shear rate [129]. L is the length in the y direction and V_d is the velocity difference between the two parallel boundaries. P is the insertion point in ordinary periodic boundary condition and P' in the case of Lees-Edwards condition.

If a linear velocity profile is imposed across the y dimension with Lees-Edwards boundary condition, the particle, which leaves the system through one of the boundaries in y direction, in contrast to standard periodic boundary condition, would not be introduced back in the symmetric location P with the same velocity. In Fig. 3.5, the particle leaving the lower y boundary is introduced back to the upper boundary at the location P'. P' is displaced to the right of the symmetric location P. The distance between the points P' and P and their relative locations depend on the magnitude of V_d (velocity difference between the two parallel boundaries) and the direction of shear velocity [129]. The velocity of the particle at position P' is increased by V_d.

3.4.4 Shearing with Constant Volume

In the default configuration of planar shear, there are two possible ways of confining the granular material. The most common method, especially for the case of dense systems, is to prescribe the normal forces acting on the top and the bottom walls and let the walls fluctuate in y direction. This would be equivalent to prescribing the pressure of the system. The other method would be to fix the y position of the walls and to shear with a constant volume. In most configurations, constant volume is preferred to shear granular gases [18, 19, 99]. The studies of da Cruz *et al.* [29, 130] on dense granular systems with MD simulations show that in steady state the system behavior for both prescribed pressure and prescribed volume are identical. They observe homogeneous shear without shear localization, except for soft particles or monodisperse assemblies.

3.4.5 Split Bottom Geometry

Split-bottom shear cell is a suitable experimental setup to study quasistatic granular flow and the widening of the shear zone. The first setups with split bottom had a cylindrical form known as modified Couette cell. This setup has been studied in many experiments, theories, and simulations [132–136]. In this geometry, the bottom of the cylinder is divided into a central and an outer part. The central part of the bottom rotates with the inner cylinder and induces wide shear zones in the bulk of the material away from the side walls. The bulk velocity profiles lie on a universal curve.

To avoid the problems concerning the cylindrical geometry of the cell (e.g. the non-

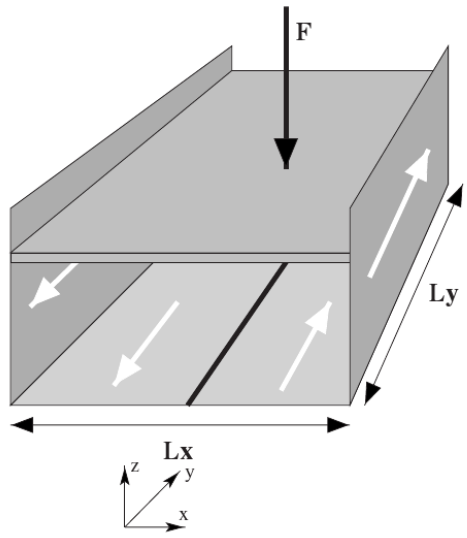

Figure 3.6: The straight split-bottom cell [131].

trivial curved shape of the shear zone, which depends also on the filling height), Ries *et al.* have simulated a straight version of the split-bottom cell (Fig. 3.6) to analyze the shear widening [131].

3.5 Shear Regimes

Granular flows are often classified into three different regimes [22]: i) a dense quasistatic regime in which the deformations are very slow and the particles interact by long lasting frictional contacts; ii) a gaseous regime with a very rapid and dilute flow, in which the particles interact by binary collision; and iii) an intermediate liquid regime in which the material is dense but still flows and the particles interact by binary collisions as well as frictional contacts.

The flow is called quasistatic, when inertia effects are negligible. This can be achieved by combining large pressure and low deformation rate [131]. In the quasistatic flows local stresses become independent of the local deformation rate. Elasto-plastic rate independent constitutive laws have been developed to describe this shear regime [137, 138].

The other extreme regime is the granular gas, in which the granular media is strongly agitated and the particles interact mainly by binary collisions as in a molecular gas. According to the analogies to gases a kinetic theory of granular gases has been developed [139], allowing for a hydrodynamical description. The kinetic theory provides

successfully constitutive equations, which connect the mean density, the mean velocity, and the granular temperature [15]. Although kinetic theory successfully describes the dilute regime, it breaks down with increasing density. This problem arises by increasing energy dissipation due to inelasticity of collisions. With increasing density, one enters the dense liquid regime [39].

The intermediate dense flow regime, characterized by both enduring contacts and collisions between particles and the existence of a percolating force network, is between the solid and gas regimes. In the dense flow regime the solid fraction is close to the maximum possible value. The contact network fluctuates strongly in space and time. The very strong correlations of motion and force makes the theoretical description of this regime very difficult [29]. Throughout this work, we deal with the dense flow regime.

3.6 Constitutive Laws

The dense granular flow is very complex and still no single rheology is defined for it. While the flow rules in the quasistatic and specially in the dilute regimes are more or less understood, the dense flow regime is not yet explainable with a single constitutive law, due to its rich variety of behaviors [27]. Lots of works have been done to this end with a large variety of geometries, material properties and compositions, under different driving circumstances [27–31, 34, 60, 76, 126, 140–142], to extract the relevant quantities, which allow to infer constitutive equations.

Planar shear is one of the studied geometries, which obeys distinct constitutive laws due to the linear velocity profiles and uniform stress distribution inside the sheared layer. Shearing dissipative, frictional, rigid materials in a plane shear geometry with several boundary conditions, the shear state has been described with a single dimensionless number, called the *inertial number* I, which describes the ratio of inertial to pressure forces [29, 60] and is defined in two dimensions as follows:

$$I = \dot{\gamma}\sqrt{\frac{m}{P}}. \tag{3.3}$$

Here, $\dot{\gamma}$ is the shear rate, m is the mean grain mass and P is the pressure.

The linear dependency of two dimensionless quantities (the solid fraction ν and the effective friction coefficient $\mu^\star$) on the inertial number I leads to the derivation of

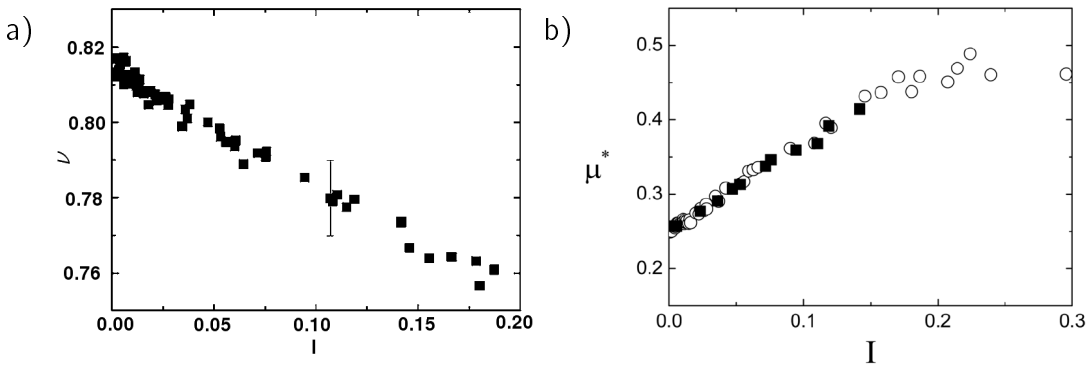

Figure 3.7: (a) Dilatancy law and (b) friction law in the bulk of a planar shear flow for μ=0.4 and various restitution coefficients and elastic stiffness constants [29, 60].

the constitutive laws for the dense granular flow. One can formulate these two linear dependencies as *the dilatancy law* and *the friction law*.

3.6.1 Dilatancy Law

The average solid fraction ν decreases approximately linearly with increasing I, starting from a maximum value ν_{max}:

$$\nu\,(I) \simeq \nu_{\text{max}} - aI \tag{3.4}$$

with e.g. ν_{max}≃0.81 and a≃0.3 for μ=0.4 (Fig. 3.7 (a)). This dependency is a result of spatial heterogeneity within the sheared layer, which increases with I [143].

3.6.2 Friction Law

The effective friction coefficient $\mu^\star$ is defined as the ratio of the shear stress to the pressure inside the material. The variation of $\mu^\star$ as a function of I is called the friction law in [29, 60]. $\mu^\star$ increases approximately linearly with I, starting from a minimal value $\mu^\star_{\text{min}}$

$$\mu^\star(I) \simeq \mu^\star_{\text{min}} + bI \tag{3.5}$$

with e.g. $\mu^\star_{\text{min}}$≃0.25 and $b \simeq 1.1$ for μ=0.4. $\mu^\star$ saturates for I⩾0.2 (Fig. 3.7 (b)).

The constitutive laws are sensitive to the microscopic friction coefficient μ. However, their sensitivity to the restitution coefficient e is restricted to μ=0 and the collisional

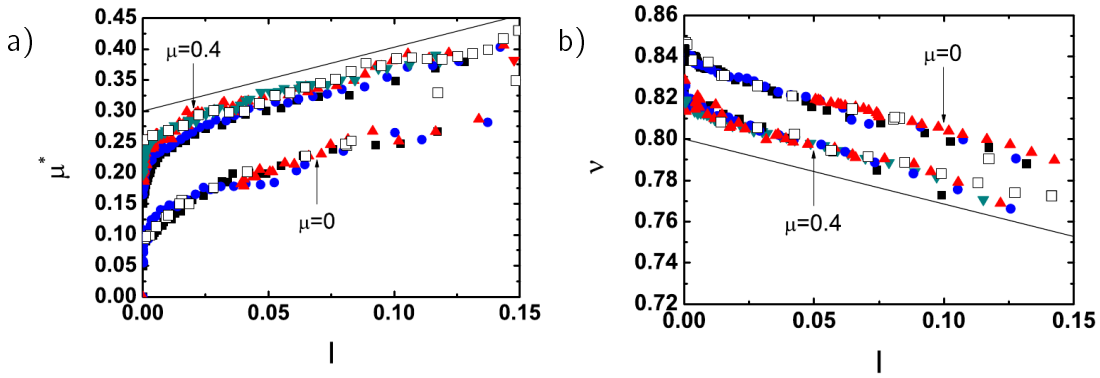

Figure 3.8: (a) Friction law and (b) dilatancy law for different annular geometries for μ=0 and μ=0.4 compared with those of planar shear. The black solid lines show the constitutive laws of planar shear with the correct slope, but some offset (cf. Fig. 3.7) [76].

regime ($I \geqslant 0.1$). The microscopic friction coefficient μ has a significant influence on the dilatancy law. The $\nu(I)$ curve remains linear, but both parameters ν_{max} and a depend on μ. In contrast, the friction law shows no obvious changes through the variation of μ, except for μ=0, where the linear increase of $\mu^\star$ is substituted by a sublinear dependency. These effects are more distinct in the quasistatic regime [29]. Presenting the effective friction coefficient as a function of the solid fraction leads to a data-collapse for all different values of the microscopic friction coefficient even for μ=0.

3.6.3 Constitutive Laws in Annular Shear Geometry

Koval *et al.* have studied the rheology of frictional cohesionless granular materials in a two-dimensional annular shear geometry [76]. As the distribution of the stress in this geometry is not homogeneous, the study of the validity of the constitutive laws is important. In this work they focus on the area near the inner wall, where the shear strain concentrates because of the large shear rate (inertial zone). The width of this region depends on the geometry and the velocity of the inner wall.

The same friction and dilatancy laws as in a planar geometry are valid for shear in an annular shear geometry for $I \gtrsim 0.02$ [34, 76].

$$\mu^\star(I) \simeq \mu^\star_{\text{min}} + bI \quad , \mu^\star_{\text{min}} \simeq 0.26, b \simeq 1 \tag{3.6}$$

$$\nu(I) \simeq \nu_{\text{max}} - aI \quad , \nu_{\text{max}} \simeq 0.82, a \simeq 0.37 \tag{3.7}$$

The parameter values correspond to microscopic friction coefficient μ=0.4. Deviations from the linear behavior are observed for $I \lesssim 0.02$ (Fig. 3.8).

4 Contact Dynamics Method

Granular matter has been widely investigated both experimentally and theoretically over a long period of time. Essentially, since the nineties computer simulations have been also used to study the behavior of granular matter from granular gases to dense granular flows and static packings. Here, the material could be treated as a continuous medium (*finite element method*, often abbreviated to FEM) [144–147] or at the level of distinct particles (*discrete element method*, often abbreviated to DEM) [145, 148–150]. The advantage of discrete simulation methods compared to the experiments is that they provide information about every particle and contact even in the bulk of the investigated material, which would require very sensitive complex experimental setups, if it is possible at all. Depending on the system under consideration, there are different simulation methods. Each simulation method has to be validated in the area of application by comparing its results with well-known experiments. According to these comparisons the abilities and weak points are manifested and the area of application of each method is determined. One major concern of simulations is their run time. For most of the methods the simulation time increases much faster than linearly with the number of particles. In order to obtain the results within a reasonable time, one is limited to moderate system sizes in simulations [62].

Throughout this work a discrete element method called *contact dynamics* (CD) has been used. This is a relatively new method developed in the eighties [151, 152]. In the nineties this algorithm has been applied to the field of granular matter by M. Jean and J. J. Moreau [153–156]. In this chapter, first the most important and widespread DEM techniques often used to simulate granular media, and then the CD method will be introduced. The contact model in CD, the solution method, and the convergence criteria are explained in details. Some experimental scenarios (validating the CD method) as well as the corresponding simulation efforts are also addressed in this chapter.

In most of the contact dynamics simulations, due to iterative solvers used to reach the convergence, the method is accurate but slow, and hence it is not suitable to simulate large scale systems. In order to preserve the accuracy of the method and

simultaneously be able to perform large scale simulations with several million particles, I have developed a distributed memory parallel contact dynamics code during my thesis, which will be introduced in chapter 9 (see also [157]).

4.1 Discrete Element Methods

The discrete element method (also called distinct element method) was first developed in 1979 by Cundall and Strack [148] based on an earlier work by Cundall in 1971 [158] and was applied to rock mechanics problems. This method is specially applicable to compute the motion of large numbers of discrete particles, interacting by either short- or long-range forces. Being capable of considering different shapes and properties of particles and various kinds of interactions, DEM has a high potential to be applied in fields like research and engineering of granular material, liquids, solutions and nano particles. The applications extend to agriculture, civil engineering, pharmaceutical, mineral processing and robotics. All DEM methods consist of three main parts:

- Initialization
- Force calculation
- Time stepping

The Initialization of the system includes the assignment of positions, orientations and velocities of the particles at the beginning of the simulation. To calculate the total forces on the particles, all different contributions from contacts with neighboring particles (friction, cohesion, liquid bridges) and long range interactions (external forces like gravity and internal ones like magnetic forces) have to be considered. To calculate the contact force, in turn, a relevant contact model has to be used. After adding up all forces acting on a particle, an integration method is needed to compute the new velocity and position of each particle in the next time step according to Newton's laws of motion. The typical integration methods are Euler, Verlet and Leapfrog algorithms. The common property of all DEM methods is that the time evolution of the system is treated on the level of individual particles, i.e. the trajectory of each particle is calculated by integrating its equations of motion.

Depending on the application field, particle properties and system density, different DEM algorithms have been developed. The main distinction could be done between algorithms with *smooth contact* models implemented e.g. in *molecular dynamics*

(MD) method [148, 149] and those with *non-smooth contact* models, on which the well-known *event-driven dynamics* (ED) [159, 160] and *rigid multibody dynamics* (RMD) [153, 154, 156, 161, 162] are based. The three methods mentioned above are often used to simulate granular media.

4.1.1 Molecular Dynamics

Molecular dynamics [146, 148–150] is the most widely used algorithm for discrete element simulations. Although DEM methods often assume nondeformable particles, in the smooth contact methods the contact force between two contacting particles is calculated according to the interpenetration of them (based on linear or non-linear contact laws). Since the particles are allowed to overlap, the notion *soft particle molecular dynamics method* is used occasionally. According to the size of overlap and the tangential velocity at the contact, the contact force is calculated locally. There have been very different contact models introduced to calculate the normal and tangential components of the contact force. In [149, 163] a summary of frequently used approaches is given. The repulsive normal force models are listed as follows:

- The linear spring-dashpot model (LSD),
- The general, nonlinear spring-dashpot model,
- The hysteretic spring model.

The tangential force models introduced are:

- Viscous tangential force,
- Coulomb friction force,
- Elastic tangential spring.

In [164], Brilliantov and Pöschel have introduced a contact model governed with viscoelastic, adhesive deformation. They have also proposed a solution of this general contact problem in the quasistatic approximation.

For granular materials, the contact forces between the soft particles stem from visco-elastic force laws. The collision duration τ in MD increases with the stiffness of particles. The collision duration is on the other hand the characteristic time in the simulation and it is recommended to take time steps proportional to τ to reduce numerical errors. This means that with increasing particle stiffness the MD simulations

become slower and are not the best choice, as experience shows [62]. Hence MD is efficient for dense systems of soft particles, but to a much less extent for hard particles and dilute systems.

4.1.2 Event-Driven Dynamics

Event-driven dynamics [165, 166] is used to simulate very dilute systems, like granular gases, in which just binary instantaneous contacts rather than multiple long-lasting contacts exist [62, 149]. This means that the particle interactions have to be of negligible duration compared to the time between the collisions. In contrast to the *classical* molecular dynamics method introduced in section 4.1.1 (also called "time-driven molecular dynamics"), the event driven method (event-driven molecular dynamics) does not work with a prescribed time step. In event-driven method the particles follow an undisturbed translational motion, until an event (a collision) happens. Accordingly, no time integration is necessary between the contact moments and just the analytical solutions are sufficient. Another difference to MD method is that the particles in ED method are assumed to be perfectly rigid without any overlap. The collisions are treated simply by using a collision matrix based on momentum conservation and energy-loss rules [149]. In the limit of dilute regime, MD and ED methods deliver similar results. With increasing particle density, as multiple contacts become more probable, the hard sphere approach used in ED method becomes invalid, while MD method still provides reasonable results.

4.1.3 Rigid Multibody Dynamics

Rigid multibody dynamics (also called rigid body dynamics) is another discrete element method to simulate completely undeformable bodies. In contrast to ED, this method is developed to deal with lasting contacts in dense systems with many simultaneous contacts [162]. The very important assumption in this model is the undeformability of particles under external forces or at collision points with other particles. Despite the strict rigidity assumption, one could apply this simulation method to study the behavior of "real" rigid materials in nature and deal with problems in engineering. Not only the behavior of granular systems can be well studied with rigid multibody dynamics, but this method is also used in robotics communities as well as for computer graphics and games [167, 168].

In RMD algorithm the contact forces are treated as unilateral constraint forces, preventing interpenetration and, to a certain extent in the case of frictional contacts, sliding. These constraints are called unilateral, since they are formulated as inequalities and are just active if the gap between two particles is zero, otherwise they have no effect [161]. Depending on the area of application (granular matter [67, 83, 169, 170], robotics [151, 171], civil engineering or computer graphics and games [167, 168, 172]) different algorithms containing appropriate approximations could be used (see Sec. 4.3). For investigations of e.g. the stress field in granular media, these approximations are prohibitive, though, and thus the *non-smooth contact dynamics* (NSCD) method [154], or commonly just contact dynamics, is widely employed. In the following sections, first an overview on the basic principles of the CD method is given. Next, other methods developed by applying approximations (with respect to the constraints or to the solver) will be introduced briefly in Sec. 4.3.

4.2 Contact Dynamics Method

In the contact dynamics algorithm, in contrast to MD, the contact forces are not calculated according to the particles deformations at the contacts. They are instead calculated according to the non-smooth contact constraints: volume exclusion perpendicular to the contact surface and Coulomb friction parallel to the contact surface. By imposing the constraint conditions, the implicit contact forces are calculated, which are requested to counteract all movements that would cause constraint violation.

For simplicity, in the following we assume that particles are dry, with repulsive (non-cohesive) interactions. Furthermore, we assume perfectly inelastic collisions, after which the particles remain in contact and do not rebounce (for the implementation of non-zero restitution coefficient see [155]). Although polygonal particle shapes are also implemented in our code, here, for simplicity just disks are considered in two dimensions. Some simulations with polygonal particles are presented in [173, 174]. Although most of the simulations deal with round particles in 2D, the extension to 3D is straightforward. In this section, I follow the description of CD method as it was published in our work on developing a distributed memory parallel contact dynamics code [157] (see also chapter 9).

4.2.1 Time Stepping

Applying unilateral constraint conditions leads to discontinuous velocities (Sec. 4.2.2). Thus the use of second (or higher) order schemes to integrate the equations of motion, as in MD, could cause problems. Based on the freshly calculated forces acting on each particle i, the particle velocities and positions have to be updated by applying a first-order Euler scheme with relatively large time steps:

$$\vec{v}_i(t+\Delta t) = \vec{v}_i(t) + \frac{1}{m_i}\vec{F}_i\,\Delta t, \tag{4.1}$$

$$\vec{r}_i(t+\Delta t) = \vec{r}_i(t) + \vec{v}_i(t+\Delta t)\Delta t\,, \tag{4.2}$$

which determines the new velocity $\vec{v}_i$ and position $\vec{r}_i$ of the center of mass of the particle after a time step Δt. The effective force on particle i is denoted by F_i. The scheme is semi-implicit in the sense that the right-hand-side velocities are (necessarily) the ones at time $t+\Delta t$, while forces other than the constraint forces may be treated implicitly or explicitly. The size of the time step Δt is chosen such that the relative displacement of the neighboring particles during one time step is much smaller compared to the size of particles (or more general, to the radius of curvature of contacting surfaces). Similar equations are used for the rotational degrees of freedom, i.e. to obtain the new angular velocity $\vec{\omega}_i(t+\Delta t)$ (caused by the new torque $\vec{T}_i(t+\Delta t)$), and the new orientation of particle i.

4.2.2 Constraint Conditions

Unlike the contact laws in MD, the unilateral constraint conditions in CD deal with inequalities. The two constraints are the impenetrability and the no slip conditions, which could be formulated for dry contacts as follows:

(a) the *impenetrability* condition: the overlapping of two adjacent particles has to be prevented by the contact force between them. Fig. 4.1 (a) expresses this constraint in the so called *Signorini graph*, in which the gap g between the surfaces of two particles (Fig. 4.2) and the normal component of their contact force R_n are related. The important aspects of this graph could be classified as follows: i) To avoid the overlap of perfectly hard particles, $g \geqslant 0$ is requested. ii) For $g>0$ without any contact the contact force vanishes ($R_n = 0$). iii) As soon as a contact is formed ($g=0$) an arbitrary large repulsive force is exerted ($R_n \geqslant 0$). In the algorithm the smallest R_n is applied at a contact, which is just

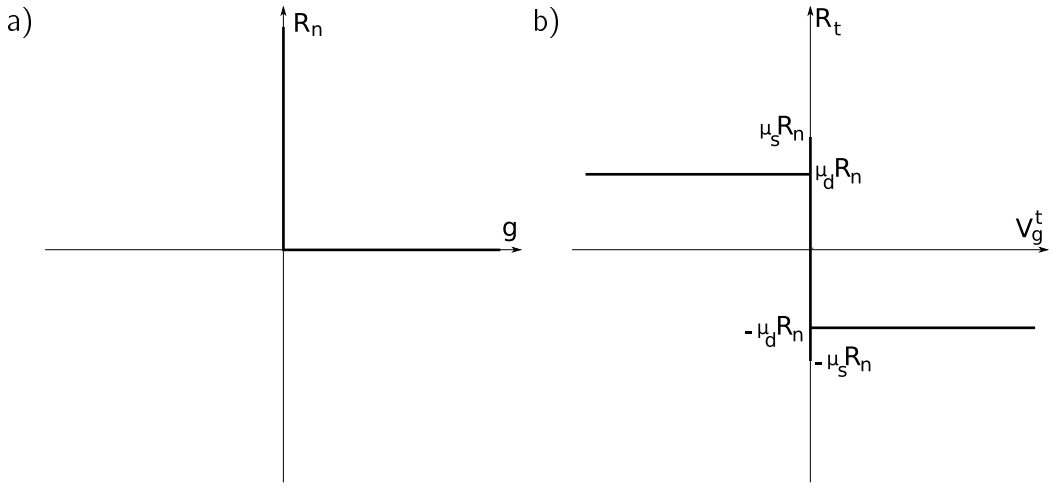

Figure 4.1: (a) Signorini graph and (b) Coulomb graph.

needed to avoid interpenetration at the next time step [175].

(b) the *no-slip* condition: the contact force should keep the contact from sliding, i.e. the tangential component of the contact force cannot be larger than the friction coefficient times the normal force. Fig. 4.1 (b) shows the *Coulomb graph*, in which the tangential component of the contact force R_t is related to the relative tangential velocity v_g^t at the contact. The important features of this graph are as follows: i) The tangential velocity v_g^t at contact could take any value. ii) For a sticking contact ($v_g^t = 0$), the tangential force takes values between $-\mu_s R_n$ and $\mu_s R_n$ (μ_s: static friction coefficient). iii) For a sliding contact the tangential force takes the value $R_t = \mu_d R_n$ (μ_d: dynamic friction coefficient) independent of the value of v_g^t. The direction of R_t is always opposite to v_g^t.

Though static friction ($\mu_s > \mu_d$) was already implemented successfully in CD [176], throughout this work we use the standard Coulomb model [177] of dry friction with identical coefficients for static and dynamic friction ($\mu_s = \mu_d = \mu$).

4.2.3 Contact Force Calculation for a Single Contact

The contact forces should be calculated in such a way that the constraint conditions are satisfied at time $t+\Delta t$, for the current particle configuration [161]. Once the total force and torque acting on the particles, including the external forces and also the contact forces from the adjacent particles, are determined, one can let the system evolve from time t to $t+\Delta t$.

Let us now consider a pair of neighboring rigid particles in contact or with a small gap between them as shown in Fig. 4.2. We define $\vec{n}$ as the unit vector along the shortest path of length g between the surfaces of the two particles. The relative velocity of the closest points is called the *relative velocity of the contact* $\vec{v}_g$. In the case that the particles are in contact, the gap g equals to zero, and $\vec{n}$ denotes the contact normal.

We first assume that there will be no interaction between the two particles at $t+\Delta t$, i.e. the new contact force $\vec{R}(t+\Delta t)$ equals to zero. This allows the calculation of a hypothetical new relative velocity of the two particles $\vec{v}_{g,0}(t+\Delta t)$ through Eq. (4.1), which is only affected by the remaining forces on the two particles. The new gap reads as:

$$g(t+\Delta t) = g(t) + \vec{v}_{g,0}(t+\Delta t)\cdot\vec{n}\Delta t. \tag{4.3}$$

If the new gap stays indeed positive ($g(t+\Delta t)>0$) then no contact is formed and the zero contact force is kept: $\vec{R}(t+\Delta t)=0$.

On the other hand, if the gap turns out to be negative ($g(t+\Delta t) \leq 0$), a finite contact force must be applied. First, we determine the new relative velocity from the condition that the particles remain in contact after the collision,

$$0 \equiv g(t+\Delta t)\vec{n} = g(t)\vec{n} + \vec{v}_g(t+\Delta t)\Delta t. \tag{4.4}$$

Here we assume sticking contacts with no relative velocity in the tangential direction ($\vec{v}_g^t(t+\Delta t)=0$), which implies that the Coulomb condition holds. The new contact force satisfying the impenetrability can be obtained using Eq. (4.1) as

$$\vec{R}(t+\Delta t) = \frac{\mathbf{M}}{\Delta t}\Big(\vec{v}_g(t+\Delta t) - \vec{v}_{g,0}(t+\Delta t)\Big) = \frac{-\mathbf{M}}{\Delta t}\left(\frac{g(t)}{\Delta t}\vec{n} + \vec{v}_{g,0}(t+\Delta t)\right), \tag{4.5}$$

where the mass matrix $\mathbf{M}$, which is built up from the masses and moments of inertia of both particles [161], reflects the inertia of the particle pair in the sense that

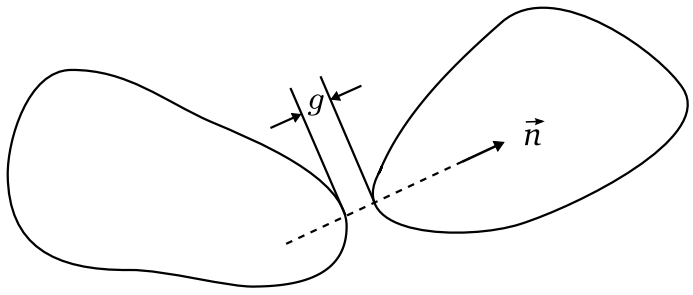

Figure 4.2: Schematic picture showing two adjacent rigid particles [157].

$\mathbf{M}^{-1}\vec{R}$ corresponds to the relative acceleration of the contacting surfaces induced by the contact force $\vec{R}$.

At this point, we have to check for the second constraint: the Coulomb friction. Let us first define the normal and tangential contact forces:

$$\begin{aligned} R_n(t) &\equiv \vec{R}(t)\cdot\vec{n} \ , \\ \vec{R}_t(t) &\equiv \vec{R}(t) - R_n(t)\vec{n} \ . \end{aligned} \tag{4.6}$$

Then the Coulomb inequality reads as

$$\left|\vec{R}_t(t+\Delta t)\right| \leq \mu R_n(t+\Delta t)\,, \tag{4.7}$$

where μ is the friction coefficient (being the same for static and dynamic friction, the standard Coulomb model of dry friction [177]). If the inequality (4.7) holds true, then we have already got the correct contact forces. Otherwise, the contact is sliding, i.e. $\vec{v}_g(t+\Delta t)$ has a tangential component and Eq. (4.4) reads

$$0 \equiv g(t+\Delta t) = g(t) + \vec{n}\cdot\vec{v}_g(t+\Delta t)\Delta t\,, \tag{4.8}$$

which determines the normal component of $\vec{v}_g(t+\Delta t)$. The remaining five unknowns, three components of the contact force $\vec{R}(t+\Delta t)$ and two tangential components of the relative velocity, are determined by the following two equations:

(i) Impenetrability by combining Eqs. (4.4) and (4.5)

$$\vec{R}(t+\Delta t)=\frac{\mathbf{M}}{\Delta t}\left(-\frac{g(t)}{\Delta t}\vec{n} + \vec{v}_g^{\,t}(t+\Delta t) - \vec{v}_{g,0}(t+\Delta t)\right). \tag{4.9}$$

(ii) Coulomb condition

$$\vec{R}_t(t+\Delta t) = -\mu R_n(t+\Delta t)\frac{\vec{v}_g^{\,t}(t+\Delta t)}{\left|\vec{v}_g^{\,t}(t+\Delta t)\right|}. \tag{4.10}$$

In two dimensions and for spheres in three dimensions, these equations have an explicit analytical solution, otherwise one has to resort to a numerical one [154].

Figure 4.3 summarizes the force calculation process for a single incipient or existing contact. Assuming that all other forces acting on the participating particles are known, the Nassi-Shneiderman diagram [178] in Fig. 4.3 enables us to determine the contact force.

<table>
<tr><td colspan="3">$g(t)+\vec{v}_{g,0}(t+\Delta t)\cdot\vec{n}\Delta t \;>\; 0$
Yes / No</td></tr>
<tr><td>$\vec{R}(t+\Delta t)=0$</td><td colspan="2">Evaluation of $\vec{R}^{\text{test}}$ via Eq. (4.5)</td></tr>
<tr><td rowspan="2"></td><td colspan="2">$\left|\vec{R}_t^{\text{test}}\right| \leq \mu R_n^{\text{test}}$
Yes / No</td></tr>
<tr><td>$\vec{R}(t+\Delta t)=\vec{R}^{\text{test}}$</td><td>Evaluation of $\vec{R}(t+\Delta t)$ via Eqs. (4.9) and (4.10)</td></tr>
<tr><td>No Contact</td><td>Sticking Contact</td><td>Sliding Contact</td></tr>
</table>

Figure 4.3: The force calculation process for a single contact [157].

4.2.4 Convergence for more than One Contact

The above process assumes that apart from the contact forces all other interactions are known for the selected two particles. However, in dense granular media, many particles interact simultaneously and form a contact network, which may even span the whole system. In such cases, the contact forces cannot be determined locally, because each unknown contact force depends on the adjacent unknown contact forces acting on the particles. In order to find the unilateral frictional forces throughout the entire contact network, an *iterative* method is mostly used at each time step in CD as follows: At each iteration step, we choose the contacts randomly one by one and calculate the new contact force considering the surrounding contact forces to be already the correct ones. It is natural to update the contact forces sequentially in the sense that each freshly calculated force is immediately used for further force calculations. One iteration step does not provide a globally consistent solution, but slightly approaches it. Therefore, the iteration has to be repeated many times until the forces relax towards an admissible state. To assess whether or not the convergence is achieved, we measure the relative change of each contact force $\vec{R}_i$ at each iteration step j, as well as the relative change in the average contact force $\vec{R}_{\text{avg}}$ at this iteration step. Generally, we choose one of the following convergence criteria to stop the force calculation procedure (more about convergence criteria and the iterative solver could be read in [62]):

(I) *local convergence test*: if, at least for 90% of the contacts, the following condition holds

$$\frac{(\vec{R}_i^{\,j}-\vec{R}_i^{\,j-1})^2}{(\vec{R}_i^{\,j}+\vec{R}_i^{\,j-1})^2} < \alpha,$$

and the rest of contacts fulfill

$$(\vec{R}_i^{\,j} - \vec{R}_i^{\,j-1})^2 < \alpha(\vec{R}_{\text{avg}}^{\,j-1})^2.$$

(II) *Global convergence test*: if the relative change in the average contact force falls below the threshold value α, i.e.

$$\frac{(\vec{R}_{\text{avg}}^{\,j} - \vec{R}_{\text{avg}}^{\,j-1})^2}{(\vec{R}_{\text{avg}}^{\,j} + \vec{R}_{\text{avg}}^{\,j-1})^2} < \alpha.$$

We have chosen α=10^{-6} in all simulations.

The precision of the solution increases smoothly with the number of iterations N_I, with the exact solution being only reached for $N_I \to \infty$. Of course we stop at finite N_I. It is optional to use a fixed number of iterations at each time step, or to prescribe a given precision to the contact force convergence and let N_I vary in each time step. Once the iteration is stopped, one has to update the particle velocities and positions based on the freshly calculated forces acting on each particle using Eqs. (4.1) and (4.2).

Terminating the iteration loop after a finite number of iteration steps is an inevitable source of numerical error in contact dynamics simulations, which mainly results in overlap of the particles and in spurious elastic behavior [179]. Occurring oscillations are a sign that the iterations were not run long enough to allow the force information appearing on one side of the system to reach the other side. This effect should be avoided and the number of iterations should be chosen correspondingly [179]. The question of successful convergence in general is difficult (cf. [180, 181]) but in practice convergence turns out to be given and hence the CD method has been experimentally validated in different instances (see Sec. 4.2.6).

Figure 4.4 concludes this section with a diagram depicting the basic steps of the contact dynamics algorithm.

4.2.5 Implementation of Rolling Friction

The idea behind the implementation of rolling friction in the CD method is related to the interlocking between (essentially round) particles to suppress their rotational degrees of freedom. Rolling resistance is also applied to mimic the effect of angularity or elongated particle shapes [110, 182]. Introducing rolling friction to CD method

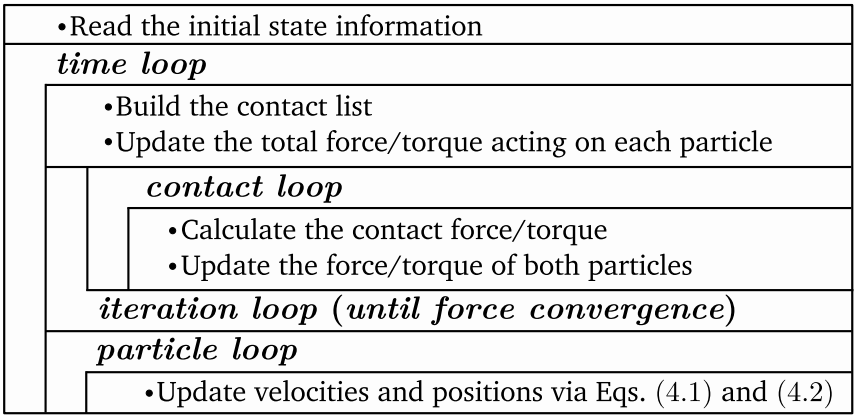

Figure 4.4: The diagram of the main steps of the contact dynamics algorithm [157].

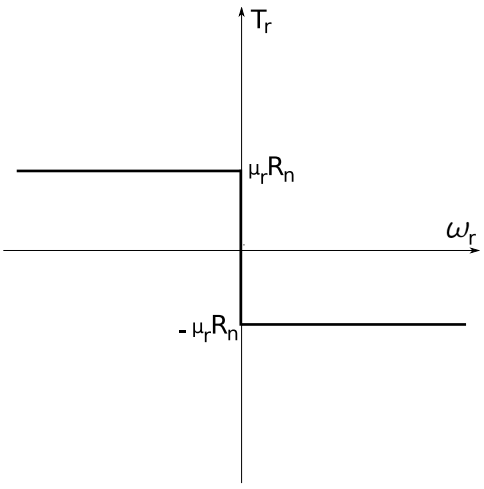

Figure 4.5: Constraint condition relating the relative angular velocity between two particles in contact and the local torque at their contact. The rolling friction μ_r is measured in length unit.

means to allow for a local torque. The constraint condition for this local torque is very similar to that of the Coulomb friction force (see Fig. 4.1 (b)), but here instead of relative tangential velocity (v_g^t) at contact, the relative angular velocity ω_r is the local kinematic variable (Fig. 4.5).

Similar to the friction force, the local torque T_r prevents the two particles from rolling against each other up to a threshold $\mu_r R_n$. Above this threshold the contact becomes rolling. μ_r does not depend on the angular velocity ω_r [183]. Exerting torque at a point contact suffers from the same problems as exerting friction force at such a contact. In both cases the extent of the contact area is regarded as negligibly small compared to the particle size [183].

4.2.6 Experimental Validation

There have been not only several experiments, which were simulated afterwards, but also those confirming predicted results of CD simulations. In this section a short list of such simulations and experiments is presented:

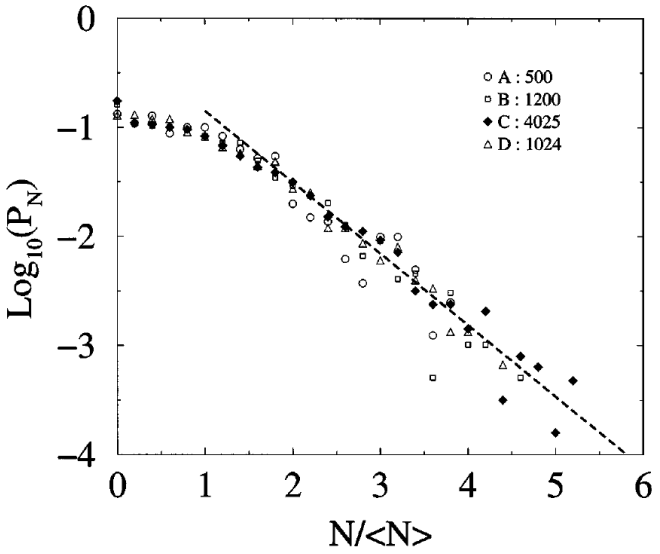

Figure 4.6: Probability density P_N of normal forces N normalized with respect to the mean normal force $\langle N \rangle$, obtained from numerical simulations [67].

1- Several experiments have been performed to measure the normal contact force distribution in static and quasistatically driven packings of granular matter. Examples are carbon-paper method [69, 70], high precision electronic balance method [82], stress-induced birefringence measurements [81], and stress chains visualization by photoelasticity [73]. Most of the experiments are just capable of measuring the contact force distribution of strong forces, which are larger than the mean normal force in the whole system ($N > \langle N \rangle$) [70, 73, 81]. However, there are more sensitive methods, which measure also the contact force distribution of weak forces ($N < \langle N \rangle$) [69, 82]. These experiments show a power law with a negative exponent for weak forces and an exponential decay for strong forces (Eqs. (2.4) and (2.5)). CD [67, 83, 84] and MD simulations confirm the above mentioned results [83, 84] not only in 2D but also in 3D packings (Fig. 4.6).

2- Lanier *et al.* [184, 185] have compared the results obtained by numerical simulations with the LMGC software (based on the contact dynamics method) and those of biaxial compression experiments of a 2D system [186, 187]. They found good agreement between the trends of micromechanical kinematics. Here, not only the statistical data (as in the previous example), but also the local quantities like the mean rotation of the particles and the evolution of the contact orientations are con-

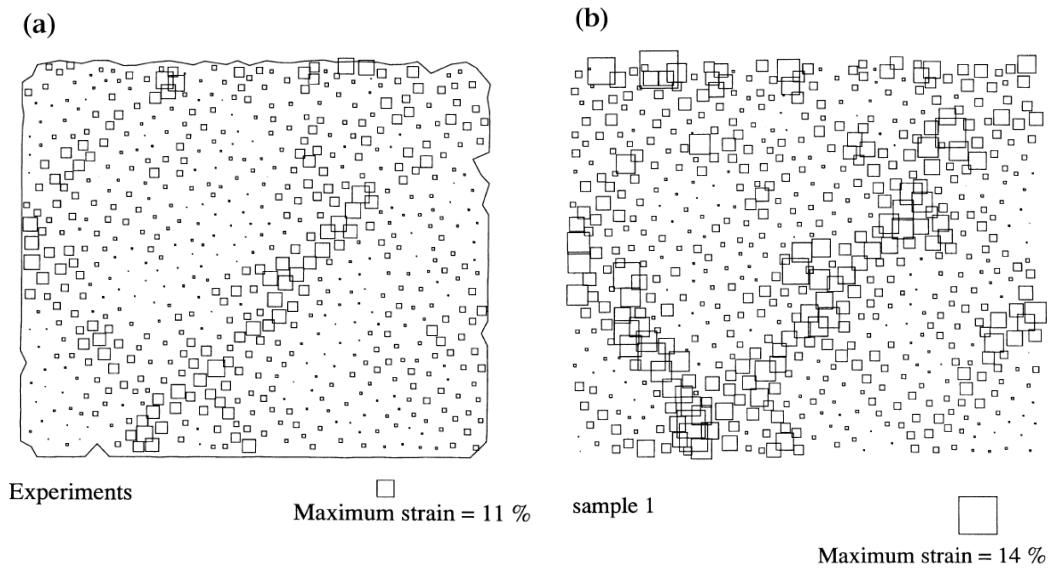

Figure 4.7: Maps of local shear intensity (E) in : (a) experiments, (b) simulations of a dense sample. On these maps the size of each square (centered on each disk), is proportional to the corresponding E-value. The dense sample shows the same pattern as the experimental one, with localization of deformation in shear bands of $3-4$ grains width. The initial configuration for this numerical simulation is exactly the same as in the experimental one [184].

sistent in experiments and CD simulations. The shear banding was also observed in these CD simulations (Fig. 4.7).

3- Kadau *et al.* have implemented a cohesion and a rolling friction model in the CD algorithm [183], which has been successfully used for comparison between the simulations and experiments [169, 188]. A macroscopic and microscopic study on the history dependence of the mechanical behavior of cohesive powders is presented in [169], where the experiments and computer simulations of uniaxial consolidation are compared. Starting with ballistic deposits of varying density, they have investigated how the porosity of the compacted sample depends on the cohesion strength and friction coefficient (Fig. 4.8), which allows to explain different pore stabilization mechanisms. The steady state flow of cohesive and non-cohesive powders in a *true biaxial shear tester* (TBT) has been investigated by means of experiments as well as CD and MD simulations in [188]. The results of the experiments and simulations were in good agreement.

4- Last but not least, by means of a recent variational model of shear zones [134, 136], Unger has lately predicted that the shear zones are refracted at material interfaces in analogy with refraction of light beams in optics [170]. By means of CD simulations in 3D, he has confirmed this prediction [170]. He found that shear zones follow Snell's law of light refraction, where the effective friction coefficient plays the role of the

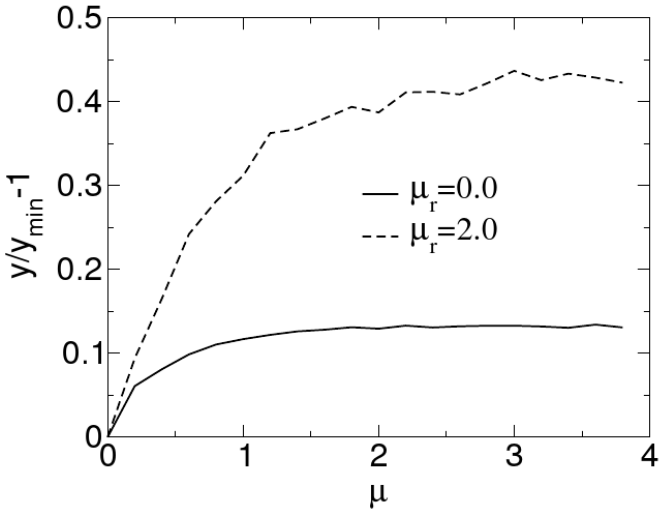

Figure 4.8: Increasing the friction coefficient μ leads to pore stabilization and thus to lower density. Additional rolling friction strengthens this effect. In this figure the final piston position y of different systems, compactified by a constant external force, is scaled by the final piston position without cohesion and friction (y_{min}) [183].

index of refraction in optics. Recently some experiments have confirmed this finding [189, 190] (Fig. 4.9).

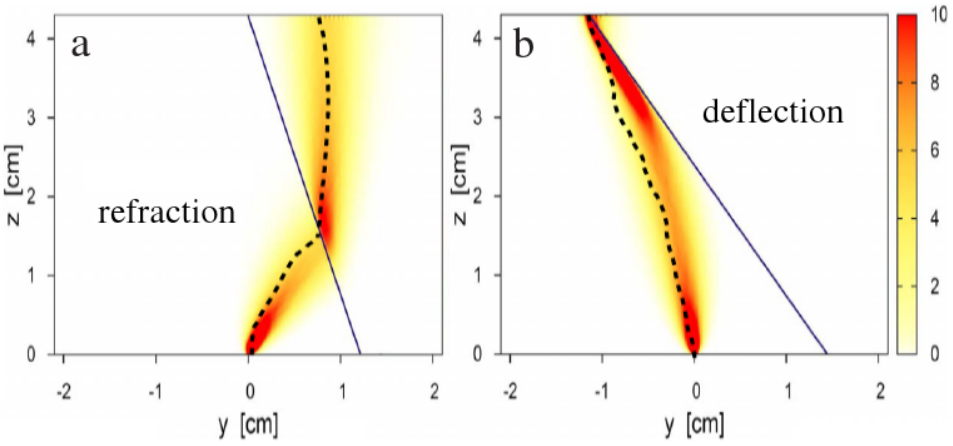

Figure 4.9: Distribution of the shear strain obtained by means of numerical simulations for (a) refraction and (b) deflection based on the fluctuating narrow-band model. The dashed lines show the center of the experimentally achieved shear zones. The solid line separates regions of high (left) and low (right) friction coefficient [190].

4.3 Applying Approximations to the CD Method

The CD method introduced in Sec. 4.2 is based on non-smooth constraints and an iterative solver, which uses the Gauss-Seidel scheme and provides a solution with high precision. By applying appropriate approximations to the original algorithm, some alternative methods have been developed, which are suitable for different purposes. Depending on the field of study and the application of the method, either a high performance speed or a high calculation precision is favored. In the robotics field an accurate prediction of friction forces is important and usually just a few contacts are involved in the problem [151, 171]. In contrast, the simulations of granular media consist of a large number of particles [67, 83, 169, 170, 184, 185, 188, 190]. Here, not only a high performance speed, but also a high precision by determining the contact forces is demanded. In contrast to the two above mentioned fields, in computer graphics for the physics based animations a real time motion of the system ingredients is desired. Here, less accurate models are implemented [191]. In both latter cases, due to the high accuracy or real time conditions, just a maximum number of several thousand particles can fulfill the demands. Some other algorithms go even further and implement algorithms overcoming the limitations arising from the high accuracy of real time conditions [172]. In the following, more insight is provided into the different approaches briefly introduced above.

4.3.1 Friction Models

In addition to the method introduced in Sec. 4.2, there is a wide variety of other approaches, which formulate the dry Coulomb friction constraint condition in a different way. To be able to apply the non-smooth friction constraint more easily, alternative smooth approximations are suggested [62]. Dealing with such regularizations, very small time steps have to be used. However, the appearance of nonphysical artifacts is inevitable [191]. Other models keep the non-smoothness, but formulate it in an easier way, ranging in complexity from frictionless and *simple box friction* to *isotropic Coulomb friction* model.

In three dimensions the friction force vector at a contact is bounded by a circular disc with a radius proportional to the normal force at the contact (Fig. 4.10 (a)):

$$\sqrt{R_{t,x}^2 + R_{t,y}^2} \leqslant \mu R_n, \tag{4.11}$$

where $R_{t,x}$ is the x component of the friction force and $R_{t,y}$ is its y component. At the

same time the direction of the friction force has to be such that sliding is prevented. To reduce the complexity of the problem, approximations may be applied. A popular approach uses a polyhedral friction cone instead of a circular cone [171, 191] (see Fig. 4.10 (b)). Usually the number of vectors (facets) is even and mostly equals to four, i.e. pyramidal cone. Such alternative models aim to use powerful standard techniques for *linear complementary problems* (LCP) [192].

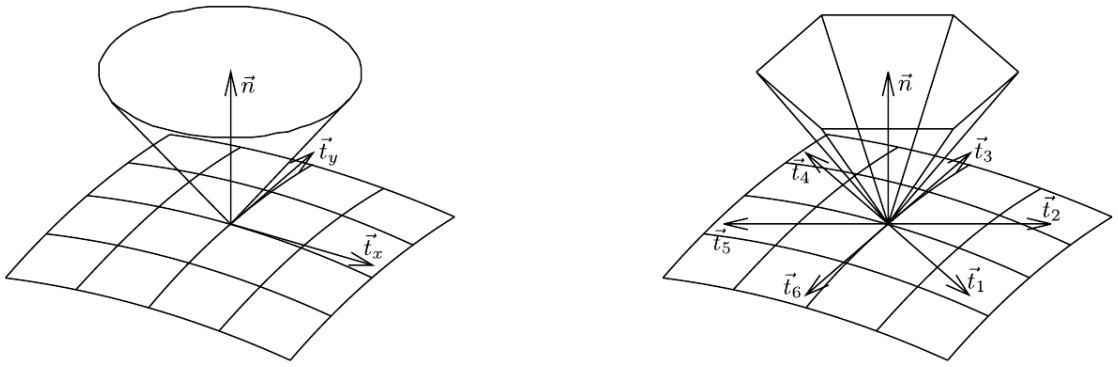

Figure 4.10: (a) The circular friction cone. (b) A polyhedral friction cone [191].

The drawback of using a pyramidal cone is that an anisotropic friction will be introduced into the problem. The anisotropy could be reduced by adding more facets to the pyramidal cone and using a polyhedral friction cone. On the other hand, the disadvantage of using a polyhedral friction cone is that additional constraints and variables have to be introduced to restrict the total friction force to the friction cone and to align the friction force, if sliding is present. Though a pyramidal friction cone does not suffer from this disadvantage, the problem will not be reduced to a LCP in this case, but to a *modified box LCP* [191].

In all three friction models introduced above (circular, polyhedral and pyramidal friction cones) the tangential forces are coupled to the normal forces. This is a consequence of restricting the contact forces to the cones. Another simplification would be to replace the friction cones by friction boxes. This would mean to use a friction cylinder, an axis aligned prism or box. The value of the normal force has to be guessed in this model, using the normal forces from the previous time step as an initial estimate. All box models are reduceable to a *box LCP* problem [191, 192].

The simplest model is to use zero friction and to reformulate the whole problem to a *standard LCP* problem. However, this over simplified model suffers from lack of practical applications [191]. Table 4.1 presents a summary of all different models introduced above, their corresponding mathematical problem and their advantages and drawbacks.

friction model	math. model	properties
circular cone friction 	NCP	- very hard to solve + isotropic friction
polyhedral cone friction 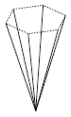	LCP	- anisotropic friction - asymmetric system matrix - hard to solve + adjustable anisotropy
pyramidal cone friction 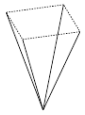	(mod.) box LCP	- non-standard bounds - anisotropic friction + symmetric system matrix
box friction 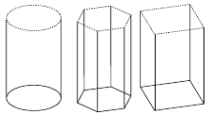	box LCP	- significant simplification (normal force decoupling) - requires estimation of normal forces - anisotropic friction + symmetric system matrix + robust solvers
no friction	LCP	- rare practical use + symmetric system matrix + robust solvers

Table 4.1: List of different friction models, the corresponding mathematical problem and the positive and negative aspects of each model [191, 192].

4.3.2 Alternative Solvers

Because of the complexity of the original non-smooth constraints (isotropic friction cone), many approaches using this model apply alternative solvers as matrix splitting methods, modified conjugate gradient method (CG) and generalized Newton methods (all iterative solvers) [192]. Gauss-Seidel solver is robust and easy to implement. The conjugate projected gradient solver leads to faster convergence, but each iteration step is almost twice as expensive. The CG solver has, however, a better performance [192]. Other methods like Newton method or optimization based approach usually fail on 3D frictional contact problems of large multibody systems. Although the Gauss-Seidel solver occasionally fails as well, it is currently the most

robust approach [193].

There are also solvers based on a modified time stepping scheme leading to a *cone complementary problem* (CCP) for the simulation of frictional contact dynamics, which can be solved by an iterative numerical method and scales linearly with the system size [194–196]. This modified scheme approaches the original scheme [197] as the time step goes to zero. At every step, the optimization-based method solves one convex quadratic program and progresses with a fixed time step. Therefore, once the time step is chosen, the number of quadratic programs that must be solved is determined ahead of time. The polyhedral approximation has been applied to the friction cone in this approach. In this model, as soon as friction is present, there will also be a normal velocity, which separates the contact undesirably [191, 194]. This effect disappears for many interesting examples as the time step goes to zero and the solution of the relaxed time-stepping scheme satisfies the *measure differential inclusion* [180, 194]. CCP is referred in [191] as a trade-off between accuracy and efficient solvability.

4.3.3 Fast Frictional Dynamics

Parallel fast frictional dynamics (PFFD) is a new parallel approach with very impressive results, as for the first time the simulation of millions of rigid bodies with rigid body dynamics simulations becomes possible, which satisfies the real time aspects [167, 168]. The PFFD method is based on the *fast frictional dynamics* (FFD) method, introduced for the first time by Kaufman *et al.* [172] and improved by Wengenroth [198]. In this method, repeated pairwise comparisons between bodies is avoided, which leads to a complexity linear in the total number of contacts detected in each iteration. A new friction model in the configuration space of rigid bodies is also developed in this context, which unifies rolling and sliding friction. While Kaufman *et al.* claim to develop an approach that results in a consistent theory and a robust linear time simulator, Wengenroth [198] argues that the introduced method has some essential weak points, which limit its applicability. FFD algorithm treats every object as a separate, independent problem and other objects only pose static constraints. This is the reason for the major speed improvement of the FFD approach and the cause of some problems as well. FFD algorithm gives perfect results for the collision of two free bodies. If one body collides with several others, however, the simulation is no longer physically accurate. As every contact is treated separately, forces or impulses are not propagated through contacting bodies. Performance is one of the main goals defined by Kaufman and co-workers. Despite the realistic-looking

behavior, the deficiencies are too grave to recommend this algorithm for scientifically motivated simulations.

Part II

New Results

5 Simulation Setup

5.1 Sample, Boundary Conditions and Control Parameters

In this chapter, the two-dimensional simulation setup, which has been used to perform the simulations demonstrated in chapters 6 to 9, is introduced. To carry out the simulations, the contact dynamics method (Sec. 4, see also [62, 154, 161]) is used. The geometry of the system is a planar shear cell with periodic boundary conditions in the shear direction (Fig. 5.1). A polydisperse assembly of particles is confined between two horizontal walls at the top and bottom. The walls are smooth by default, without any roughening particles glued onto their surface. Coulomb friction exists at the interface between the particles and the walls with μ_{W}=0.5, except where explicitly stated differently. The walls move with the same constant velocity V in opposite directions. The external pressure applied to the system is prescribed, via normal inwards oriented forces to the walls and the walls are allowed to fluctuate in the y direction (Fig. 5.1). The particles are hard dry disks, interacting by Coulomb friction forces parallel to, and volume exclusion forces normal to the contact surfaces, with collisions being fully inelastic. The microscopic inter-particle friction coefficient, while being freely adjustable, was also set to μ_{P}=0.5, except where explicitly stated differently.

In order to realize the boundary conditions mentioned above (constant pressure and constant shear velocity), an anisotropic mass matrix is assigned to the walls,

$$M = \begin{pmatrix} M_{xx} & M_{xy} \\ M_{yx} & M_{yy} \end{pmatrix} = \begin{pmatrix} \infty & 0 \\ 0 & M_{yy} \end{pmatrix} .$$

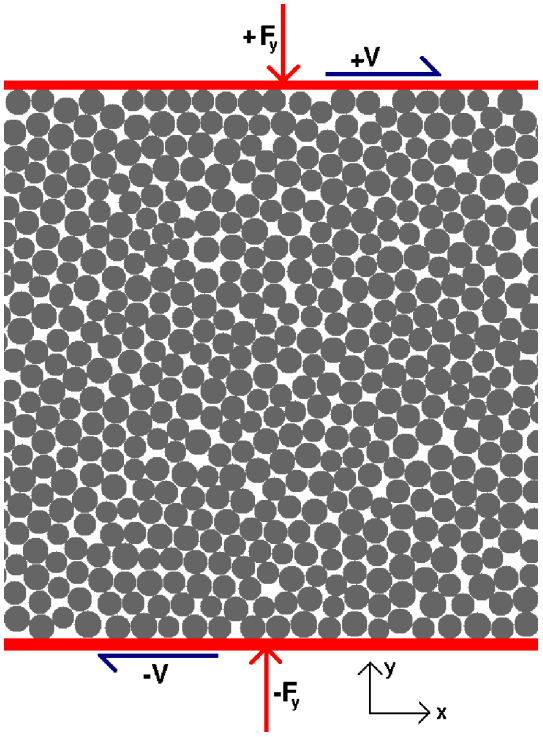

Figure 5.1: A polydisperse system of hard frictional disks in a two-dimensional planar shear geometry with periodic boundary conditions in x direction. A prescribed normal force F_y to the confining walls determines the constant external pressure of the system. The walls move with the same constant velocity V in opposite directions.

5.2 System Preparation

To preserve the symmetry of the top and bottom walls and to avoid segregation (Sec. 2.1.3) [5] during the preparation, the system is horizontally filled: While the distance L_y between the walls is kept fixed, a third, vertical wall is introduced on the left side of the system, on which the grains settle in response to a "gravity" force field parallel to the x axis. At this step, the particles are temporarily rendered frictionless. Then gravity is switched off and the free surface of the material is smoothed and compressed by a piston transmitting $\sigma_{xx} = 0.25$ (the same value as σ_{yy} imposed in shear flow), until the equilibrium is reached. The width of the system L_x is determined at this stage. Then the vertical wall and the piston are removed, the friction coefficients are set to their final values μ_{P} and μ_{W}, and periodic boundary conditions in the x direction are imposed. With constant L_x and variable L_y, the shearing starts with velocities $\pm V$ for the walls and an initial linear velocity profile within the granular layer, extended from $-V$ at the bottom to $+V$ at the top.

5.3 Units

The diameter of the largest particles is taken as the length unit (d=1[L]). Similarly, the mass density of the particles is set to unity (ρ=1[M]/[L]^2). The time unit is chosen such that the pressure (normal forces applied to the walls divided by the length of the walls) have a value P=0.25[M]/[T]^2, which leads to: F_y=5[M][L]/[T]^2. In other words, the following base units for length, mass and time are used:

$$[L] = d,$$
$$[M] = d^2\ \rho,$$
$$[T] = \sqrt{5\, d^3\, \rho / F_y}.$$

To avoid ordering phenomena (crystalization in 2D), the particle diameters are distributed homogeneously between 0.8d and d, giving rise to a polydispersity of about 20%.

In this work, results of different samples with various sizes are presented. System sizes and simulation parameters are listed in Tab. 5.1.

Idx	n	L_y	L_x	σ_{yy}	V	T_{SS}	T_{Sim}
1	511	20	20	0.25	0.005-5.00	620	20000
2	1023	40	20	0.25	0.03-30.00	2500	10000
3	1023	40	20	0.0625	0.03-30.00	9900	10000
4	3199	50	50	0.25	0.01-30.00	4000	8000
5	2047	80	20	0.25	0.01-20.00	10000	4000-12000
6	3071	120	20	0.25	0.01-35.00	22000	6000
7	5119	200	20	0.25	0.01-30.00	64000	13000
8	4097	160	20	0.25	0.01-1.5	10240	10000

Table 5.1: Parameters used in the simulations. n is the number of disks in the sample. T_{SS} denotes the characteristic time to approach steady state according to Eq. (7.12). T_{Sim} is the total (physical) simulation time in each run.

5.4 Measured Quantities

Before presenting the results, the methods used to measure the effective friction coefficient, the velocity profiles, the inertial number and other quantities used troughout chapters 6 to 8 are explained here.

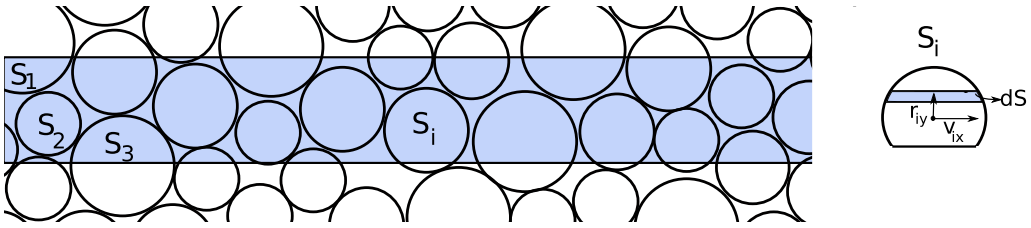

Figure 5.2: Profiles of different quantities are calculated by averaging the partial or complete contribution of each particle, proportional to its area S_i located inside the stripe.

To calculate the x component of the velocity profiles, the system is divided into horizontal stripes of height $\Delta y = 1$ (Fig. 5.2). A velocity is attributed to each horizontal stripe centered at y=y', by averaging the partial or complete contribution of each particle located inside the stripe as (Fig. 5.2, right) [199]:

$$v_x(y') = \frac{\sum_i \int_{S_i} (v_{ix} + \omega_i r_{iy}) dS}{\sum_i S_i}. \tag{5.1}$$

S_i denotes the surface fraction of particle i within the stripe, v_{ix} its center of mass velocity in x direction, ω_i its angular velocity and r_{iy} is the vertical distance between the center of mass of the particle and a differential stripe of vertical position y and area element dS within area S_i (Fig. 5.2). Although the velocity is not constant within the area element dS, considering the symmetry, Eq. (5.1) leads to exact results. The velocity profiles presented here are also averaged over consecutive time intervals of Δt=80.

In the calculation of the profiles of stress tensor, each particle contributes to each stripe in proportion to the area contained in the stripe:

$$\sigma(y') = \frac{\sum_i \sigma^i \, S^i}{\sum_i S^i}. \tag{5.2}$$

Alternatively, one can calculate the contact contribution proportionally to its branch vector length within the stripe. Another possibility is to cut through the particles and add up the contact forces of all cut branch vectors. All these three different methods lead to indistinguishable results in the simulations.

In the dense and quasistatic flow regimes, the stress is dominated by the contact contribution. σ_c^i is the total contact stress tensor calculated for each particle i with

area $A_i = \pi d_i^2/4$ as follows [34, 60, 76, 200]:

$$\sigma_c^i = \frac{1}{A_i} \sum_{j \neq i} \vec{F}_{ij} \otimes \vec{r}_{ij}. \tag{5.3}$$

The summation runs over all particles j having a contact with particle i. $\vec{F}_{ij}$ is the corresponding contact force and $\vec{r}_{ij}$ denotes the vector pointing from the center of particle i to its contact point with particle j. σ_f is the kinetic stress tensor, associated to the velocity fluctuations and is calculated for particle i of mass m_i as follows [34, 60, 76, 200]:

$$\sigma_f^i = \frac{1}{A_i} m_i \delta\vec{v}_i \otimes \delta\vec{v}_i, \tag{5.4}$$

with $\delta\vec{v}_i$ being the difference between the center of mass velocity of particle i and the average particle velocity in the stripe. σ_r is the contribution of rotation to the stress tensor, associated to the rotation of the particles and is calculated for particle i as follows [34, 60, 76, 200]:

$$\sigma_r^i = \frac{1}{A_i} \frac{1}{2} I_i \omega_i^2 I_2, \tag{5.5}$$

where I_i is the moment of inertia of particle i and ω_i its angular velocity. I_2 is the unity matrix in $2D$.

To calculate the effective friction coefficient one could use the components of the global stress tensor of the system, when contact, kinetic and rotational contributions are taken into account [60, 76, 103]. Considering a symmetric stress tensor ($\sigma_{xy} = \sigma_{yx}$) and isotropy in x and y directions, which leads to $\sigma_{xx} = \sigma_{yy}$, one could write:

$$\mu_{eff} = -\frac{\sigma_{cxy} + \sigma_{fxy}}{\sigma_{cyy} + \sigma_{fyy} + \sigma_{ryy}}. \tag{5.6}$$

For a system in steady state, assuming a constant stress tensor in the whole system, an alternative method to calculate the effective friction coefficient is to average the total tangential and normal forces acting on the walls over time t and then calculate their ratio [201]:

$$\mu_{eff} = \frac{\langle |F_T| \rangle_{W,t}}{\langle |F_N| \rangle_{W,t}}. \tag{5.7}$$

The subscript W,t denotes averaging over time and over top and bottom walls.

Finding no significant difference, both methods have been used in this work. In

chapter 7, μ_{eff} is measured in the interior of the system (according to Eq. (5.6)) considering all terms of the stress tensor, although the contact contribution dominates. In chapter 8, μ_{eff} is measured according to Eq. (5.7)

Finally, three additional average velocities are also considered. Let us assume that N^{bottom} and N^{top} particles are in contact with the bottom and top walls, respectively. Then, the corresponding average center of mass velocities

$$v_x^{\text{bottom}} = \frac{1}{N^{\text{bottom}}} \sum_{i=1}^{N^{\text{bottom}}} v_{x,i} \quad , \quad v_x^{\text{top}} = \frac{1}{N^{\text{top}}} \sum_{i=1}^{N^{\text{top}}} v_{x,i} \quad , \tag{5.8}$$

average angular velocities

$$\omega^{\text{bottom}} = \frac{1}{N^{\text{bottom}}} \sum_{i=1}^{N^{\text{bottom}}} \omega_i \quad , \quad \omega^{\text{top}} = \frac{1}{N^{\text{top}}} \sum_{i=1}^{N^{\text{top}}} \omega_i \quad , \tag{5.9}$$

and average surface velocities at particle-wall contact points

$$v_s^{\text{bottom}} = \frac{1}{N^{\text{bottom}}} \sum_{i=1}^{N^{\text{bottom}}} (v_{x,i} + r_i\omega_i) \quad , \quad v_s^{\text{top}} = \frac{1}{N^{\text{top}}} \sum_{i=1}^{N^{\text{top}}} (v_{x,i} - r_i\omega_i) \tag{5.10}$$

can be defined. These are additionally time averaged over the whole duration of the steady state, where the set of contributing particles may change over time. The quantities (5.8) to (5.10) are used in Figs. 8.4 and 8.7.

5.5 Steady State

A system sheared with a certain constant velocity under a prescribed normal stress reaches a steady state after a transient. For instance, in a system of size L_x=50 and L_y=50 with a large shear velocity, V=0.7, the steady state is reached after a shear distance of about $\lambda \simeq 420$, corresponding to a shear strain $\gamma \simeq 8$ (Fig. 5.3). The shear distance in all graphs is calculated by multiplying the total shear velocity ($2V$) by time, in which V is the absolute value of the wall velocity. Due to the existence of slip at smooth walls and because of nonhomogeneous flow, the presented values for the shear distance and shear strain overestimate the real values in the bulk of the material. The transient time before the steady state is estimated in Sec. 7.3.1, based on the constitutive laws.

In the steady state, the velocity profiles fluctuate around the average, with a certain

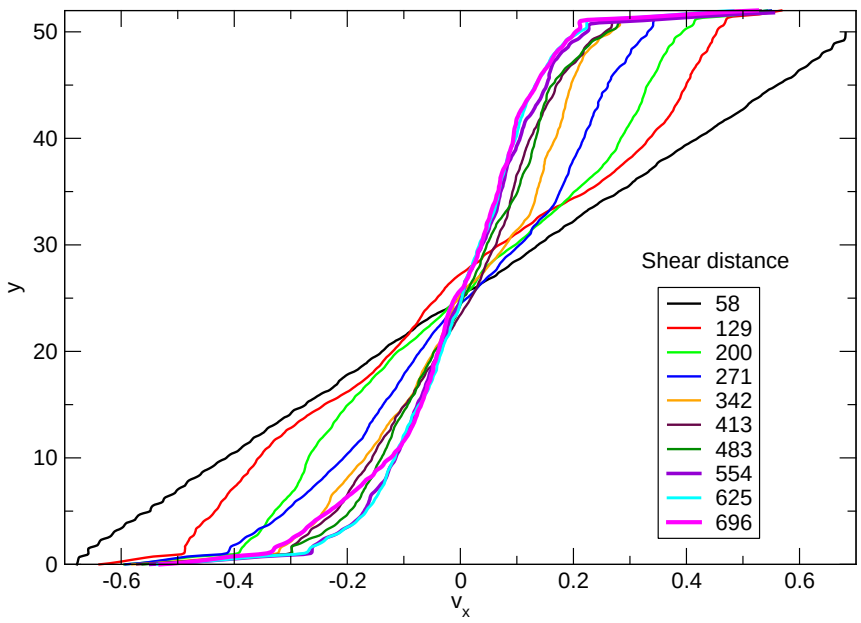

Figure 5.3: Transient to the steady state for $V = 0.70$ in a system with $L_x = 50$ and $L_y = 50$.

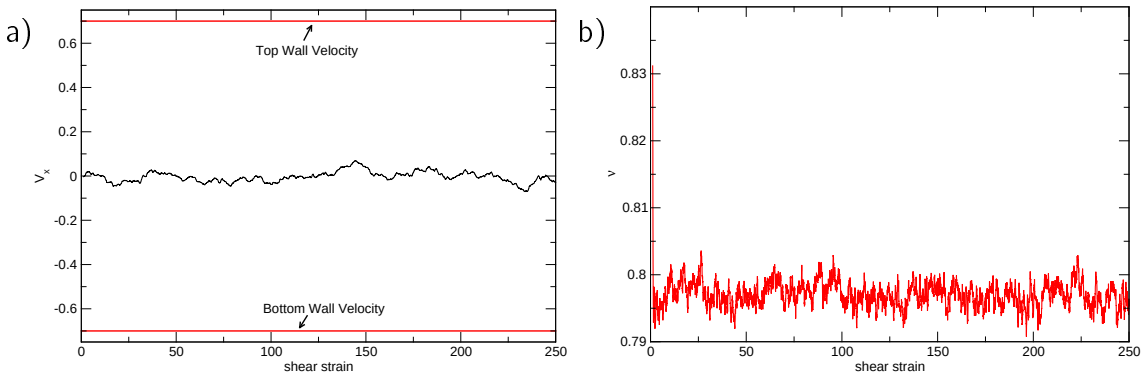

Figure 5.4: (a) Center of mass velocity and (b) solid fraction versus shear strain for $V = 0.70$ in a system with L_x=50 and L_y=50.

correlation time. Although the center of mass velocity in the system of Fig. 5.4 (a) fluctuates with a large amplitude (about 10% of the velocity V), fluctuations of the global solid fraction ν (measured in the whole system) amount to only about 1% of the average after a short transient (Fig. 5.4 (b)).

In the steady state, the profiles of the effective friction coefficient stay almost uniform throughout the system (Fig. 5.5).

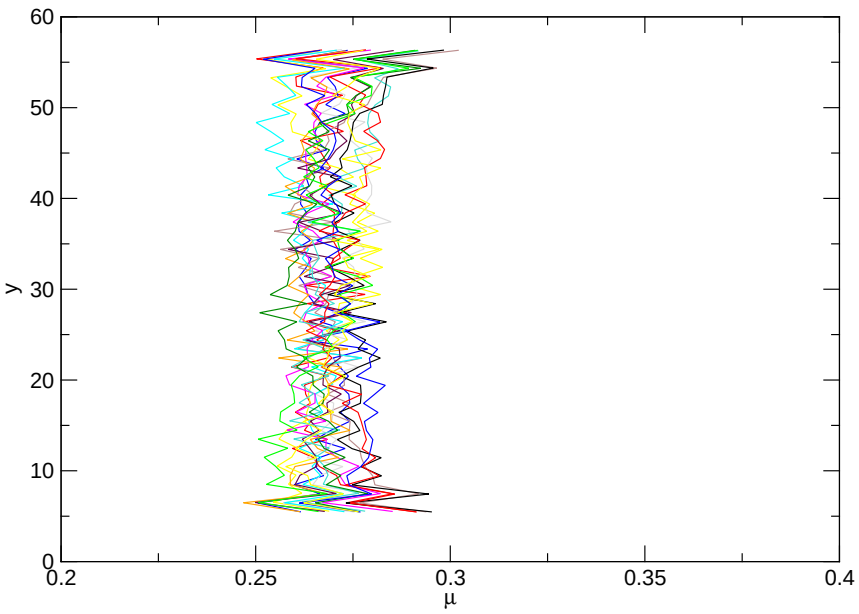

Figure 5.5: Profiles of the measured effective friction coefficient in the steady state for V=0.70 (L_x=50 and L_y=50) at different times (different colors).

6 Velocity and System Size Dependence of Shear Flow

In this chapter, the results of planar shearing of two dimensional dense systems of bidisperse as well as polydisperse, non-cohesive, hard, dissipative and frictional disks are presented. These systems are sheared with smooth, frictional walls at constant shear velocities under a prescribed pressure. The simulations are done using the contact dynamics method. The high initial density $\nu \simeq 0.85$ and the fully inelastic (with restitution coefficient e=0), frictional collisions are special features of all simulated systems. All systems start with a linear initial velocity profile, interpolating between the bottom to the top wall velocity (cf. chapter 5). In the following, the dependency of shear flow behavior on shear velocity and system size has been investigated. The main results of this chapter have already been published in [202, 203].

6.1 Shear Regimes and Strain Localization

Figure 6.1 shows the time evolution of the velocity profiles of a system of initial height L_y=160, as it is sheared with different velocities (a) V=1.5, (b) V=0.2 and (c) V=0.01. There exist some major differences between the behavior of the velocity profiles at these three velocities. If we shear the system with a high velocity of V=1.5, after a transient the velocity profile adopts a symmetric almost linear shape with only weak fluctuations in time. There is symmetric weak shear localization at both walls including slip. In this case, the system is almost homogeneously sheared. This regime is called *the fast or homogeneous shear regime* (regime A in the sequel). If the system is sheared with an intermediate velocity of V=0.2, in the steady state the velocity profiles adopt on average an almost symmetric shape, in which the shear is strongly localized at the walls, and less than ten layers away from the walls there is no more shearing. The velocity profiles have a moderate fluctuation in time. This regime will be referred to as *the intermediate or two-shear band regime* (regime B). In contrast, at the low shear velocity of V=0.01, the velocity profiles fluctuate very strongly and

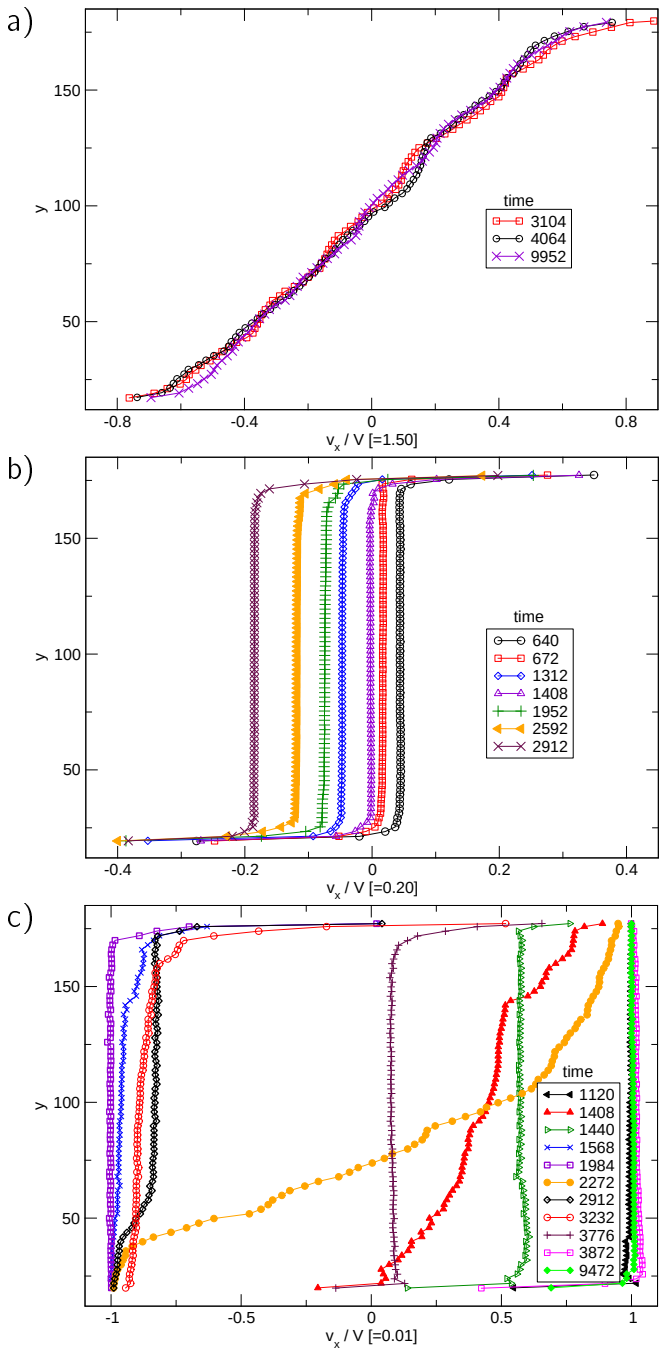

Figure 6.1: Velocity profiles at different times for shear velocities (a) V=1.50, (b) V=0.20 and (c) V=0.01 in a system of height L_y=160. Time t=9952 corresponds to shear strain γ=188 for V=1.50, γ=25 for V=0.20 and γ=1.25 for V=0.01.

are generally asymmetric. In such cases the shear is localized strongly at one wall and most of the filling moves together like one block with the other wall. This is *the slow shear or one-shear band regime* (regime C).

To summarize, concerning the shape of the velocity profiles, we distinguish between three different shear regimes A, B and C, which are separated at velocities V_{AB} and V_{BC}:

A) Fast shearing ($V > V_{AB}$=0.5): Symmetry preserved, homogeneous shearing, weak fluctuations.

B) Intermediate shearing ($V_{BC} < V < V_{AB}$): Symmetry preserved, shear localization at both walls, moderate fluctuations.

C) Slow shearing ($V < V_{BC}$=0.1): Symmetry broken, shear localization at one wall, strong fluctuations.

In the following, I address the question, how to characterize these three regimes and the transitions between them. In order to be able to observe all three regimes, sample height L_y should be large enough. In smaller systems ($L_y \lesssim 80$), the effects of the boundary layers on the central region are strong enough to preclude the observation of a clearly developed intermediate regime. Sheared granular layers of smaller thickness (smaller L_y) most often appear to exhibit a direct transition from regime A to regime C on decreasing velocity V.

Starting from regime B, no shearing in the bulk and strong shear localization at both walls is observed. The fluctuations of the velocity profiles decrease with increasing shear velocity. At V_{AB}, the shear rate in the bulk raises obviously and increases afterwards continuously with increasing V. Simultaneously, the shear localization at the walls becomes weaker.

In regime A the sheared layer behaves similarly to the one reported by da Cruz *et al.* [29, 60], in a numerical study of steady uniform shear flow of a granular material between rough walls. However, with rough walls the homogeneous shear regime persists down to very low velocities. The smooth walls in the present system, allowing for slip and rotation at the walls, are responsible for the more complex behavior [202, 203].

Upon reducing the shear velocity in the intermediate shear regime towards V_{BC} growing fluctuations in the velocity fields are observed. Slightly above V_{BC} the approach to a steady state becomes problematic, even after the largest simulated shear strain (or wall displacement) intervals. Then below V_{BC} the width of the distribution of the bulk region velocities reaches its maximum value, $2V$, and the velocity profile stays for longer and longer time intervals in the localized state with one shear band at a wall (regime C). Such localized profiles can be regarded as quasi-steady states – as switches from one wall to the opposite one occur ever more seldom at lower velocities.

Figure 6.2 is a plot of the center of mass velocity V_x in the flow direction versus

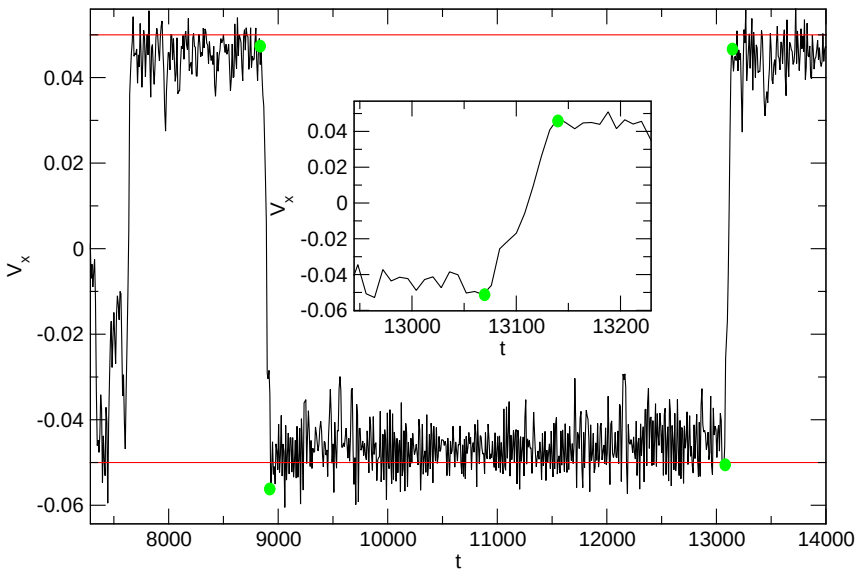

Figure 6.2: Center of mass velocity fluctuations in steady state for V=0.05 in a system with L_x=20 and L_y=20. The transition time (magnified in the inset) is measured at both ends of direct transitions from one wall to the other, between the full circles.

time in regime C. Most of the time, it is slightly fluctuating around the value of either one of the velocities of the walls, $\pm V$. Transition times as the shear band switches directly from one wall to the other are measured as indicated. Those times are recorded to be discussed in Sec. 7.3.1.

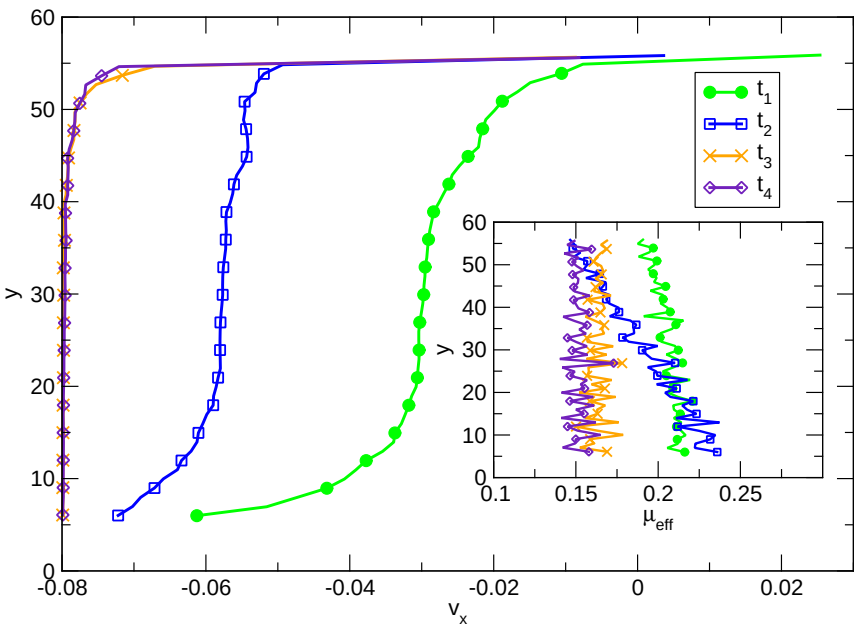

Figure 6.3: Profiles of velocity and effective friction coefficient (inset) in steady state and in the transient states for V=0.08 in a system with L_x=50 and L_y=50.

As an indication for the states with asymmetric velocity profiles, being in steady state, they exhibit uniform stress profiles, contrarily to the nonuniform ones in the

transient states, as the localization pattern is switching to the other side (Fig. 6.3).

6.1.1 Profiles of Angular Velocity

The angular velocity profiles of a system of height L_y=160 in the steady state for different shear velocities in fast, intermediate and slow shear regimes are plotted in Fig. 6.4. In fast and intermediate shear regimes the angular velocity profiles are symmetric (Figs. 6.4 (a) and (b)). The particles rotate faster near the walls. The comparison of these two profiles shows, that the rotation in the bulk of the intermediate shear regime is much smaller than in the fast shear regime. One may speak about frustration of the rotational degrees of freedom. In the slow shear regime (Fig. 6.4 (c)) the angular velocity profile is asymmetric. The particles rotate in the shear band at one wall. In the block, which extends to the other wall, the rotational degrees of freedom are frustrated. These results agree with those of J. P. Bardet and J. Proubet [101, 102]. In their study, they show that the rotation of particles is concentrated in the shear bands. They use this fact to determine the width of the shear bands.

6.1.2 Profiles of Effective Friction Coefficient

Figure 6.5 presents the profiles of the measured effective friction coefficient μ_{eff} in steady state. With increasing shear velocity, the mean effective friction coefficient increases, while the width of its distribution around the mean value decreases. For V=0.01 (Fig. 6.5 (c)), $\langle\mu_{\text{eff}}\rangle$=0.166 with a standard deviation of 0.044. For V=0.10 (Fig. 6.5 (b)), $\langle\mu_{\text{eff}}\rangle$=0.190, while the standard deviation is reduced to 0.020 and for V=0.70 (Fig. 6.5 (a)), $\langle\mu_{\text{eff}}\rangle$=0.269 with a very small standard deviation of 0.009.

6.2 Transition Velocity V_{BC}

6.2.1 Center of Mass Velocity

The center of mass velocity V_S divided by V, m=V_S/V, seems to be a good parameter to describe the symmetry breaking. For a symmetric profile m is zero, whereas for the

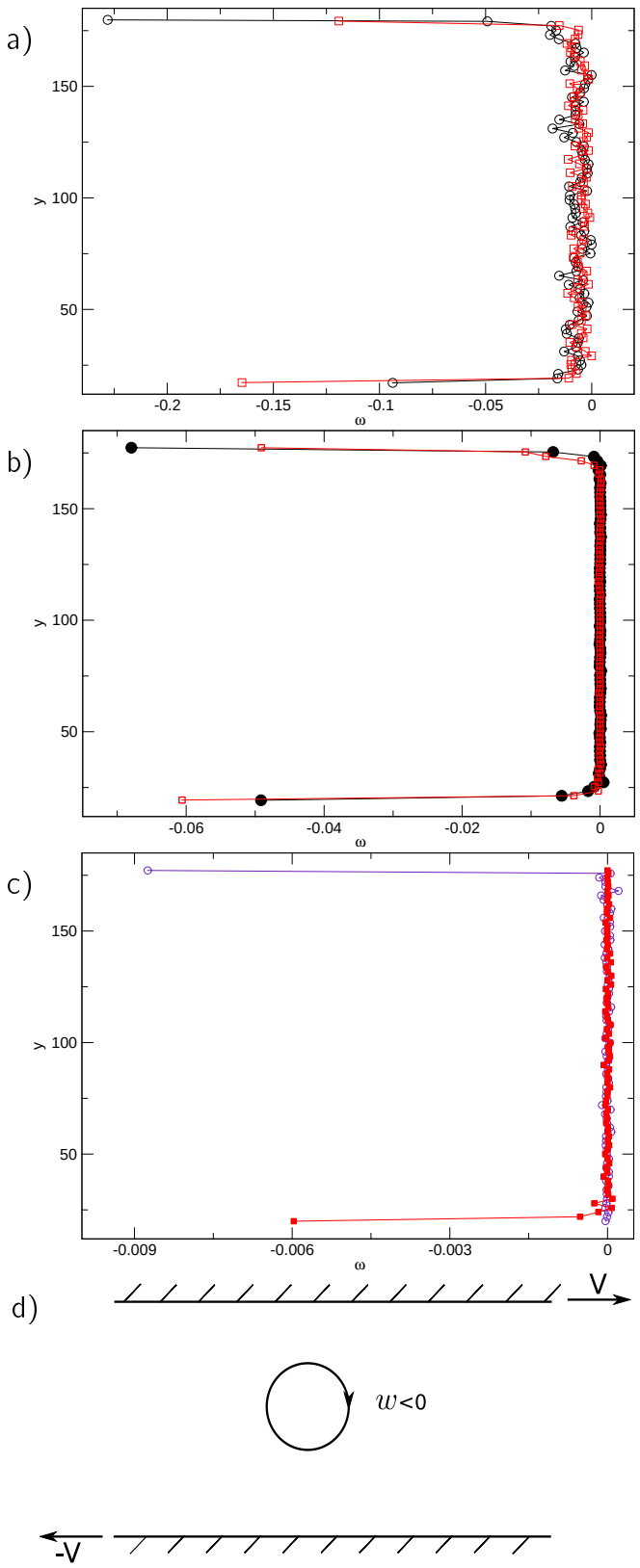

Figure 6.4: Angular velocity profiles at different times for shear velocities (a) V=1.50, (b) V=0.20 and (c) V=0.01. The profiles in graph (c) are asymmetric. (d) Sign convention of ω in relation to wall velocities.

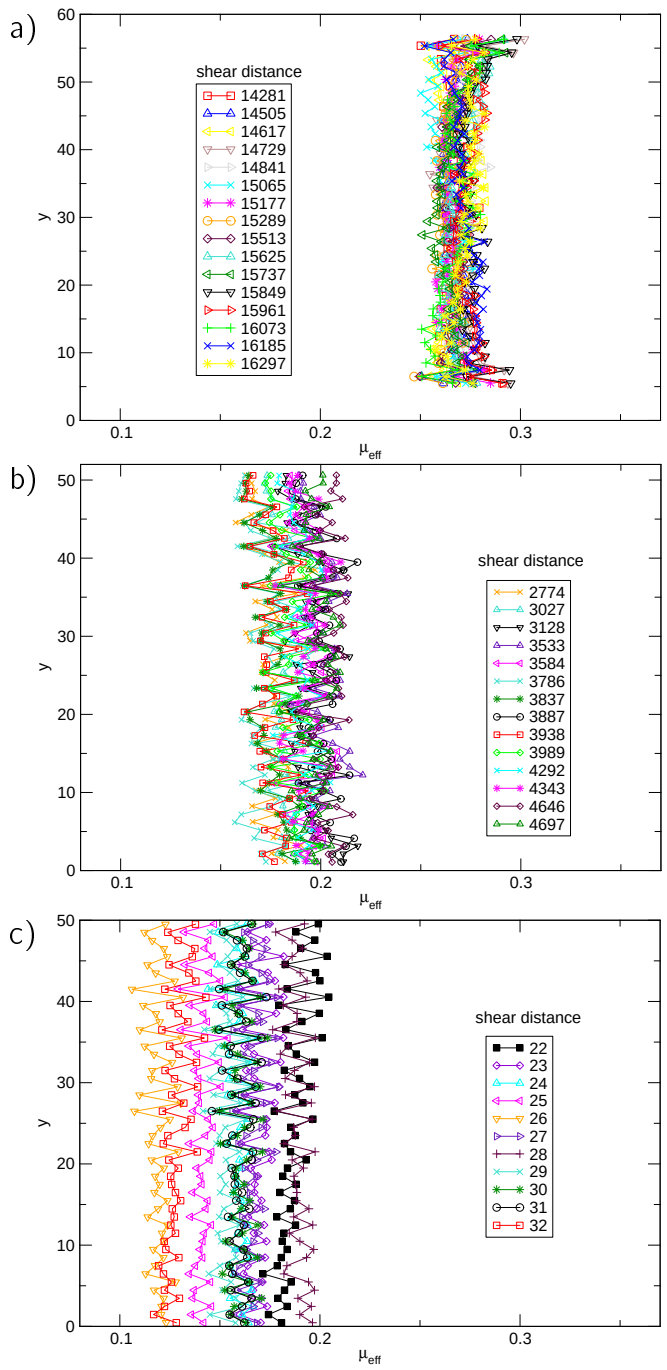

Figure 6.5: Local shear to normal stress ratio, or effective friction coefficient μ_{eff} in steady state for (a) V=0.7, (b) V=0.10 and (c) V=0.01 in a system with L_x=50 and L_y=50.

asymmetric block-like motion described above it is close to ± 1.

Note that for a finite system a spontaneously broken symmetry is restored dynamically, i.e. m switches back and forth between $m \approx 1$ and $m \approx -1$ with a characteristic switching time τ that should diverge with system size (cf. Sec. 6.2.4). As a consequence, $\langle m \rangle \to 0$ also in the symmetry broken phase, if one averages over

long enough times $t \gg \tau$, and even more so, if one averages over the ensemble of equivalently prepared random samples as well ($\langle . \rangle$ denotes both averages).

6.2.2 Order Parameter

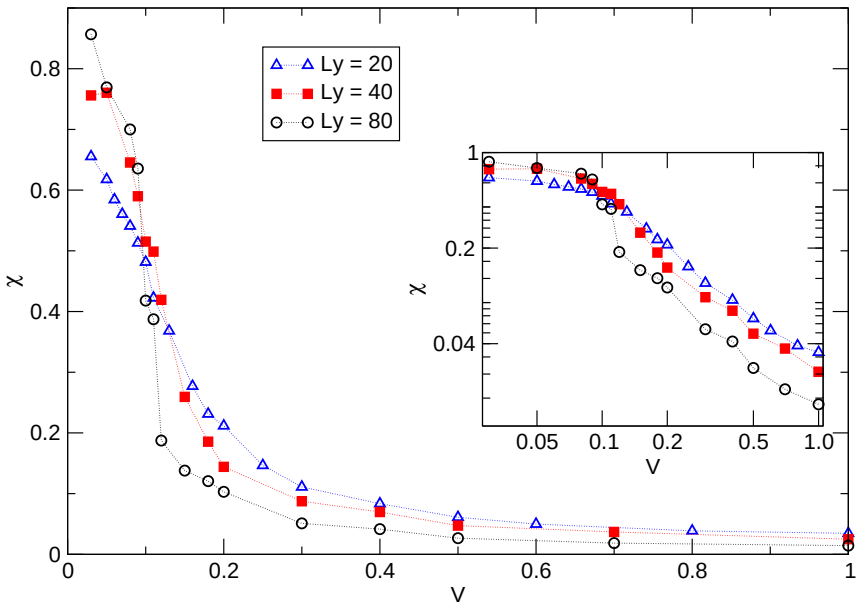

Figure 6.6: Order parameter χ vs. shear velocity for systems of different initial heights L_y=20, L_y=40 and L_y=80. The inset shows the same data semi logarithmically.

The fluctuations of the normalized center of mass velocity m seem to be a good measure to define an order parameter, which describes different system behavior in shear regimes B and C. To quantify these fluctuations, the order parameter χ is defined as the standard deviation of m as follows:

$$\chi = \sqrt{\langle m^2 \rangle - \langle m \rangle^2}. \tag{6.1}$$

The averaging was done over a time t=20000 and 10 different runs so that $\langle m \rangle \approx 0$ in all cases. Figure 6.6 shows the order parameter χ as a function of shear velocity V for different system sizes L_y. Since $\langle m \rangle \approx 0$, χ approaches a constant value, which should be approximately $\langle |m| \rangle^2$ in the low velocity regime.

Interestingly, for increasing system size, the fluctuations decrease for velocities $V > V_{BC} \approx 0.1$, while they increase below V_{BC}. Consequently, χ becomes steeper at V_{BC}, for increasing system size. This behavior indicates a phase transition at $V_{BC} \approx 0.1$ (cf. also Sec. 6.2.3). Furthermore, right at V_{BC} the order parameter does not depend on system size noticeably.

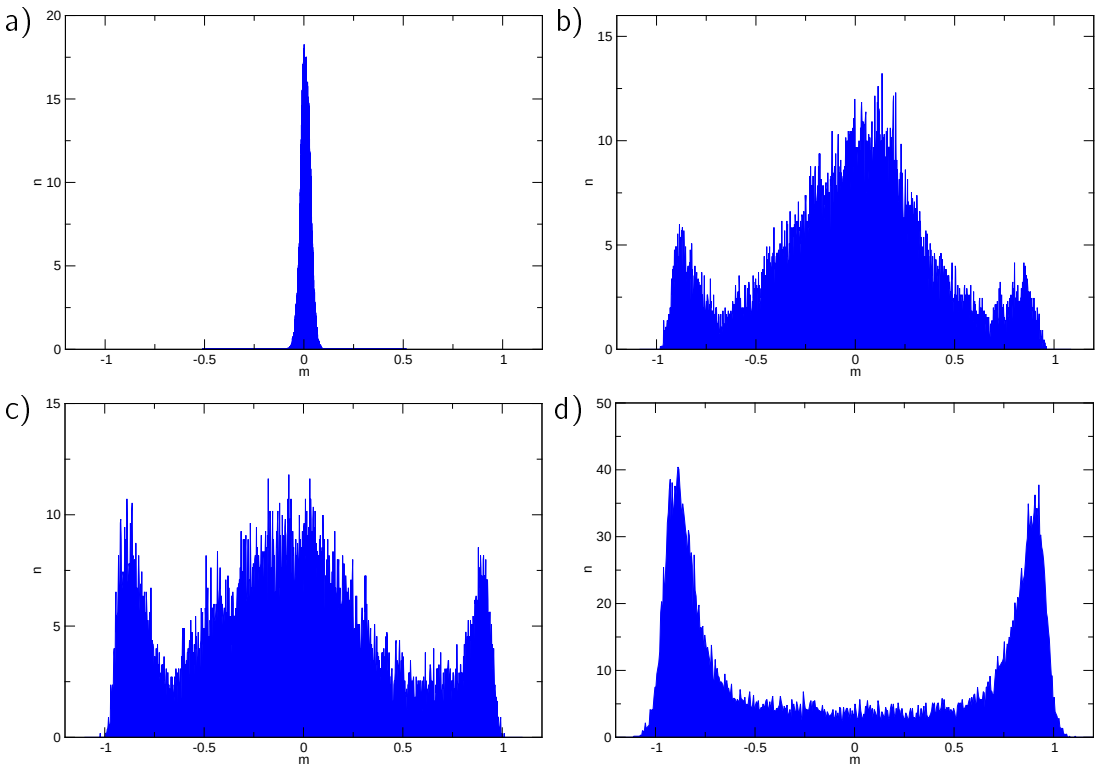

Figure 6.7: Histograms of the normalized center of mass velocity in a system of height L_y=40 with shear velocities (a) V=0.5, (b) V=0.12, (c) V=0.1 and (d) V=0.05.

da Cruz *et al.* [29] show in their study of a plane shear flow of a dense assembly of dissipative disks (prescribing pressure and shear rate and using rough walls to shear the system) that the continuous flow becomes intermittent in the quasistatic regime. In this case, the filling of the system oscillates between two localized states near the moving or the fixed wall. In contrast to my results, those two localized states have a very short duration and most of the time the system is in an intermediate state, where the shear is approximately uniform in the whole system.

6.2.3 Histograms of m

Fig. 6.7 shows four histograms of the normalized center of mass velocity $m(t)$, accumulated over a long time. For large velocities (Fig. 6.7 (a)) m values are concentrated at m=0. For small velocities (Fig. 6.7 (d)), there exist two peaks close to m=±1. They are symmetric as a result of ensemble averaging. For large systems the histograms for individual runs remained asymmetric, because the reversal of the center of mass velocity became too rare to restore the symmetry within the recording time. Close to the transition velocity V_{BC}, the central peak widens and decreases, while the

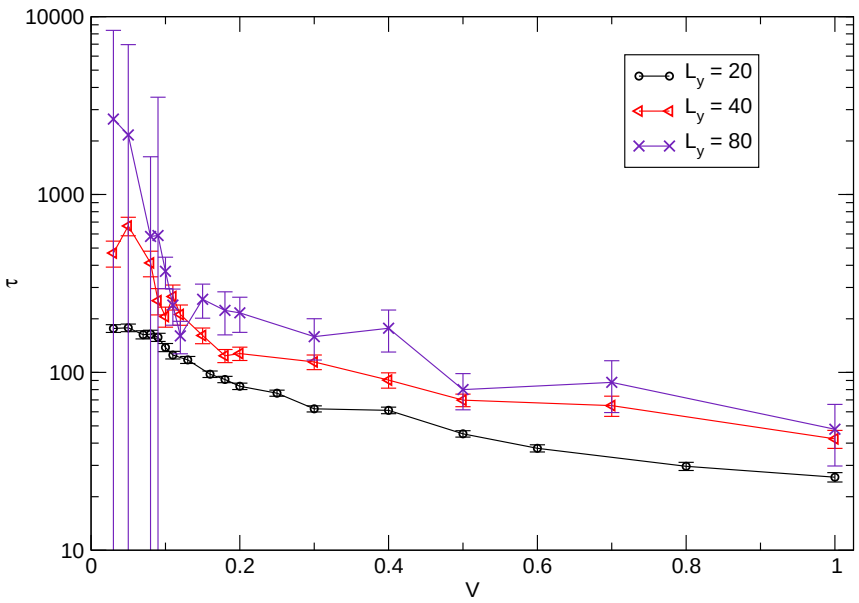

Figure 6.8: Ergodic time against shear velocity for systems of different heights L_y=20, L_y=40 and L_y=80.

outer peaks grow in place, i.e. without moving continuously outwards from the center (Figs. 6.7 (b) and (c)). With increasing system size, the interval of shear velocities, for which the histogram shows three peaks, becomes narrower. This behavior is the phenomenology of a first order phase transition (cf. also Sec. 6.2.2).

6.2.4 Ergodic Time τ

The ergodic time τ is the average time until a jump between the two outer histogram peaks (in general, from positive to negative side and vice versa for shear velocities larger than V_{BC}) happens. This quantity is plotted against shear velocity for different system sizes in Fig. 6.8. τ increases with system size L_y and is expected to grow to infinity for an infinite system below the critical shear velocity V_{BC}, which corresponds to symmetry breaking in the thermodynamic limit. Hence, the lifetime of the one-shear band asymmetric steady shear profiles increases with system height L_y, similar to ergodic time in magnetic systems [174, 202].

6.3 Transition Velocity V_{AB}

6.3.1 Formation of Blocks

It is illuminating to study the transition from fast to intermediate shearing more closely: In an initially linear velocity profile (cf. system setup in chapter 5) zones of almost no shear (*blocks*) appear (cf. Fig. 6.9) in the transient state. If their width is small enough and their lifetime short enough, they are perceived (especially when employing temporal averaging) as a homogeneous profile. But for smaller and smaller velocities, their number decreases, while their width increases, until at a certain velocity V_{AB} (≈ 0.5 in our two-dimensional case) only one block of width almost equal to L_y remains (Fig. 6.10). Then, the velocity profile is almost like a step function and we have reached the regime of intermediate shear.

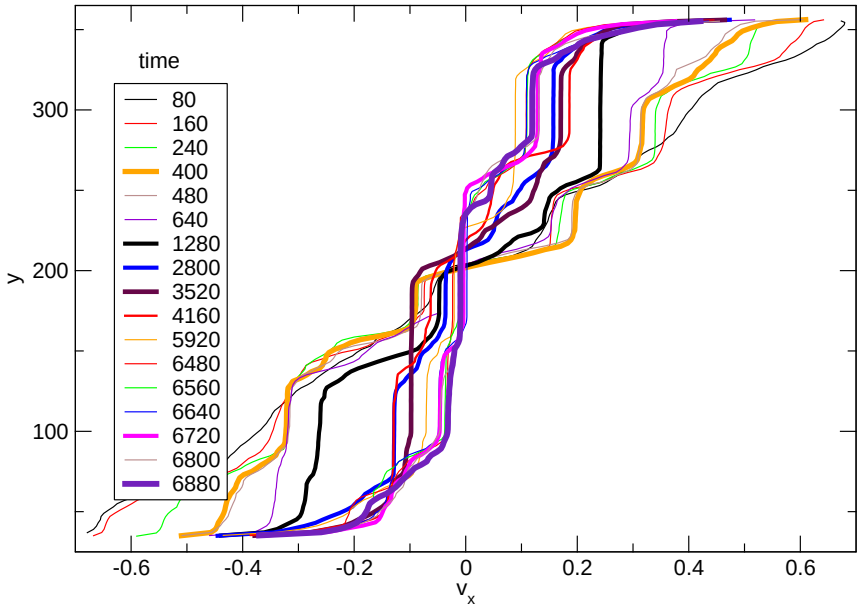

Figure 6.9: The time evolution of the velocity profile for V=0.7 (fast shearing regime) in a system of size L_y=320.

If we, within the intermediate shear regime, reduce the driving velocity further, the system needs less and less time to build up a step like profile from the initial linear profile. In contrast, in the fast shear regime, the system needs a very long time to reach the steady state with homogeneous shear and free of the blocks (cf. Sec. 7.3.1).

As very large systems need a long time to reach the steady state, the system properties in the transient have also been studied to distinguish between the different shear regimes. In Tab. 6.1, the number of shear bands (including the internal ones) in the late transient states has been presented as a function of shear velocity and system

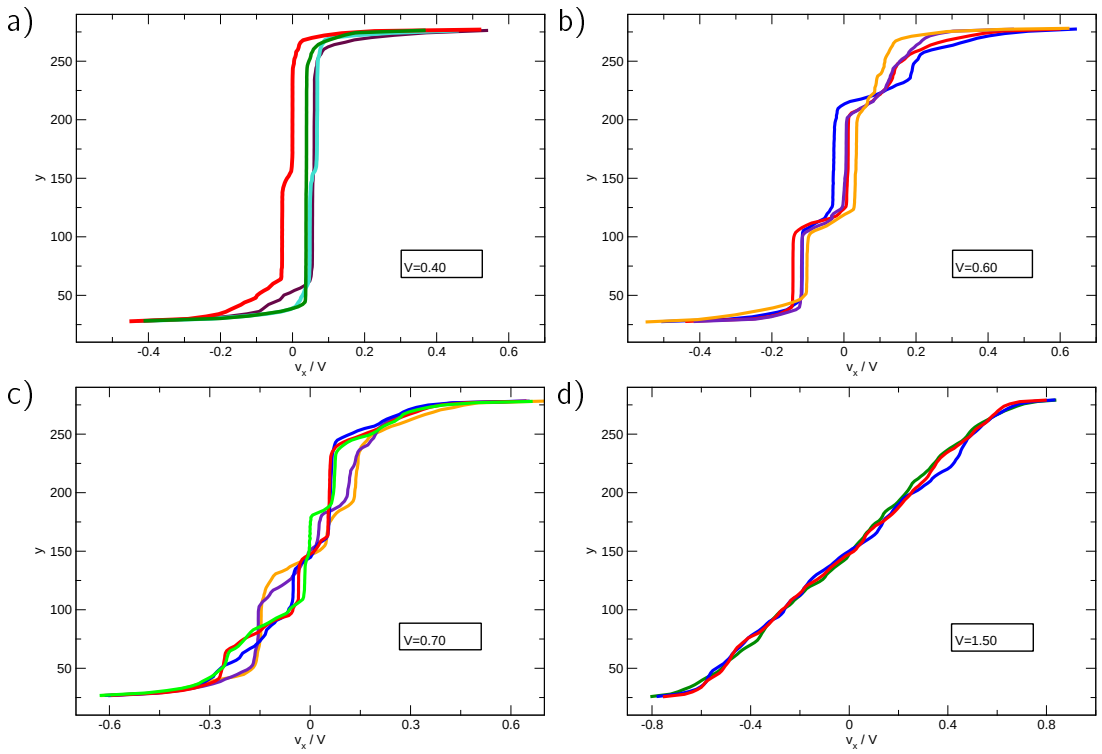

Figure 6.10: The velocity profiles in the transient time in a system of height L_y=250 at different velocities: (a) V=0.4, (b) V=0.60, (c) V=0.70 and (d) V=1.50.

size. For $V_{BC} < V < V_{AB}$, the system exhibits two wall shear bands after a short transient (Fig. 6.10 (a)), which may overlap in too small systems. For $V > V_{AB}$, the number of internal shear bands grows with V (Figs. 6.10 (b) to (c)) but can be suppressed due to a small system size. For larger systems shear band overlap (perceived as continuous shear) occurs at higher shear velocities. Especially, the large systems show clearly the tendency to have just two shear bands at the walls for $V < V_{AB} \simeq 0.5$. For smaller systems ($L_y \leqslant 80$), the intermediate shear regime could hardly be observed.

6.3.2 Shear Rate Measurements

A quantity, which allows to check, whether a single block is formed in the system, in other words, whether we are below the fast shear regime, is the average shear rate $\bar{\dot{\gamma}}$ in the bulk of the system. For that, I have measured the inverse of the slope of the velocity profiles within a region of width $2\Delta < L_y$ centered at y=$L_y/2$ (to exclude

V \ Ly	20	80	160	200	250	320
0.03	1	1	1	1	1	1
0.05	1	1	1	1	1	1
0.08			2	1	2	2
0.10	1	1	1	2	2	2
0.12	1		2	1	2	
0.15	2-C	2	2	2	2	
0.18	2-C		2	2	2	2
0.20	2-C	2-C	2	2	2	2
0.25	C	2-C	2	2	2	2
0.30	C	2-C	2	2	2	2
0.40	C	2-C	2	2	3	2
0.50	C	2-C	2	2	2	2
0.60	C	C	3-C	3-C	4	5
0.70	C	C		C	4-C	5-C
0.80	C	C	C	C	C	
0.90	C	C	C	C	C	
1.00	C	C	C	C	C	C
1.20	C	C	C	C	C	C
1.50	C	C	C	C	C	C

Table 6.1: Number of shear bands in the late transient states for different system sizes and shear velocities. C denotes continuous shearing.

the shear zones at the walls) averaged over time,

$$\bar{\dot{\gamma}} = \left\langle \frac{v_x(L_y/2+\Delta,t) - v_x(L_y/2-\Delta,t)}{2\Delta} \right\rangle_t . \tag{6.2}$$

Figure 6.11 shows $\bar{\dot{\gamma}}$, averaged in a central region of height 2Δ=40, plotted against the shear velocity in a system of initial height L_y=160. In this graph a sharp bent of $\bar{\dot{\gamma}}$ at $V_{AB}\approx$0.5 is observed. At this point, coming from higher velocities, the shear in the bulk vanishes. With increasing size of Δ, the sharpness of the bent at V_{AB} could vary, depending on the number of additional internal shear bands and blocks, which are considered by averaging.

At this point the question arises, whether or not the difference between the intermediate and fast shearing regimes is simply a finite size effect. Figure 6.12 shows that this is not the case. The upper three curves are in the fast shearing regime, where $\bar{\dot{\gamma}}$ is inversely proportional to L_y as expected. The lower three curves are in the intermediate, respectively the slow shearing regime. Here $\bar{\dot{\gamma}}$ decreases faster than the trivial $1/L_y$ with increasing system size, i.e. the "quality" of the block improves for large systems.

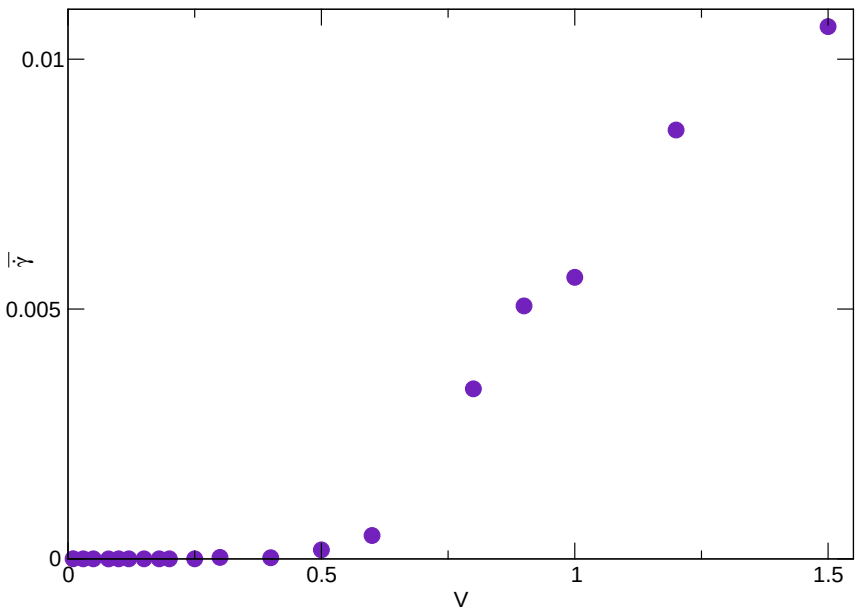

Figure 6.11: Average shear rate in the bulk of a system of height L_y=160 plotted against shear velocity ($2\Delta = 40$). The error bars are smaller than the symbol size.

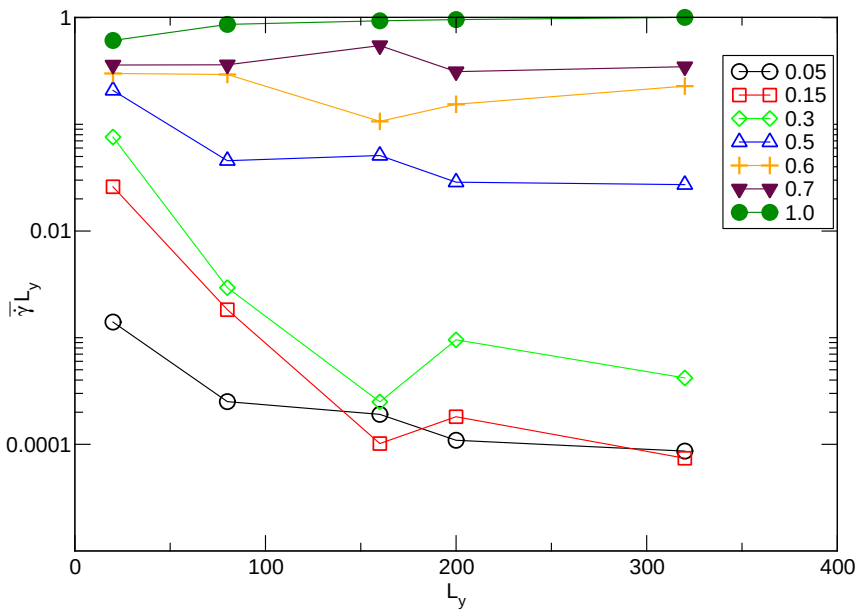

Figure 6.12: $\bar{\dot{\gamma}}L_y$ for different shear velocities as a function of system size. The error bars are smaller than the symbol size.

6.3.3 Friction Mobilization

The three different shear regimes should manifest themselves in a different type of overall reaction of the system on the driving, i.e. the shear resistance or macroscopic wall friction μ_{eff}. This is confirmed by Fig. 6.13, where there exist two linear sections of different slopes in the fast and intermediate shearing regimes, which cross at

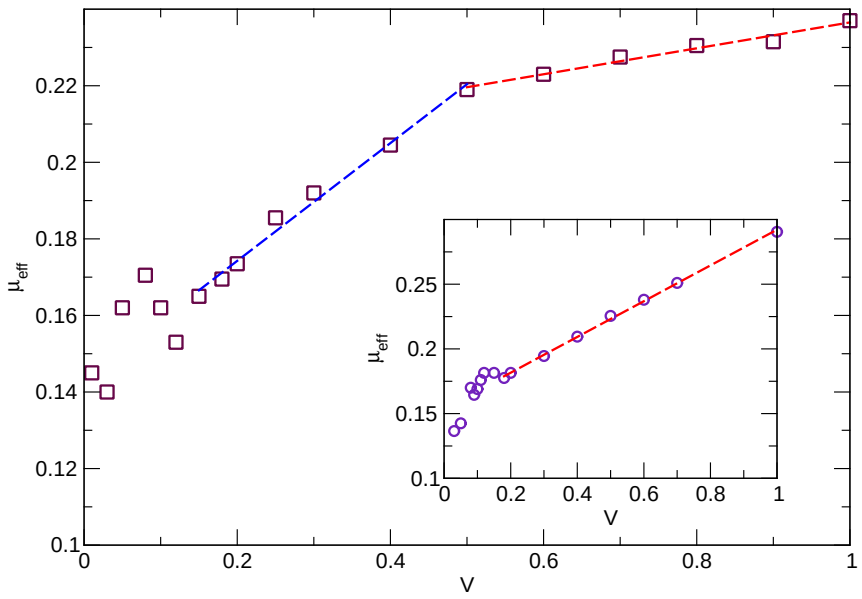

Figure 6.13: Friction as a function of shear velocity in a system of height L_y=200. The inset shows the absence of the intermediate regime in a small system of height L_y=20. The error bars are smaller than the symbol size.

V_{AB}. This feature is consequently missing for a small system of L_y=20, where, as already discussed above, the intermediate regime is absent. Towards the slow shearing regime, the fluctuations of μ_{eff} grow stronger and impede a confirmation of the extension of a linear $\mu_{\text{eff}}(V)$ with the same slope to these small velocities.

In [29] the macroscopic friction was found to depend linearly on the inertial number, which is proportional to the shear rate. In the always homogeneous shearing in [29], this shear rate is the global one and thus μ_{eff} depends linearly on V there. On the other hand, in our case the heterogeneity of the velocity profile implies a more complex relationship between the inertial number and V. Moreover, the wall friction does not depend directly on the contact density at the wall but is governed by the ability of particles to rotate.

An important characteristic of the fast shearing regime is that shear is no longer a surface property but occurs everywhere in the bulk. In the blocks, the relative translational and rotational velocities of the particles are negligible compared to those in the shear bands. Hence, moving away from shear bands, one expects that the density of contacts increases, while the density of sliding contacts decreases. Consequently, the ratio of sliding contacts, $M=\frac{N_s}{N}$ (*friction mobilization*) will increase towards the walls. The graphs in Fig. 6.14 confirm this argument (Compare this figure with Fig. 6.1).

One sees obviously the asymmetric shape of the mobilization profiles in the slow

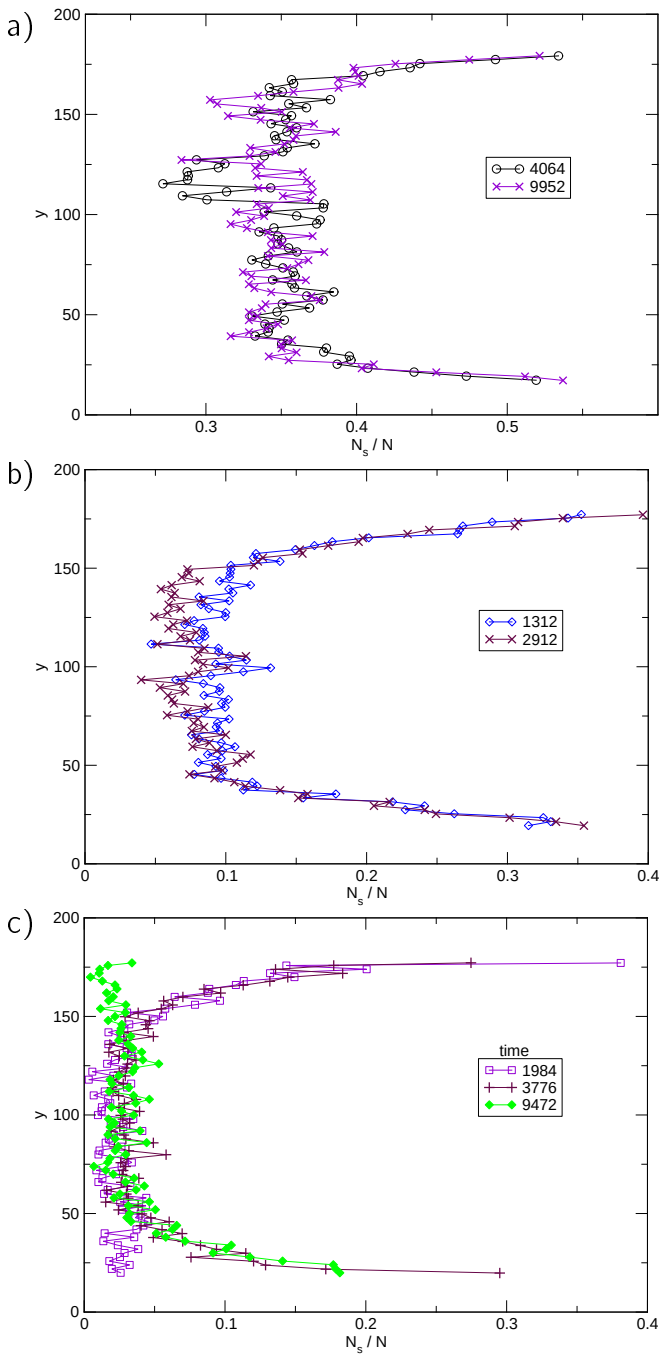

Figure 6.14: Profiles of friction mobilization at different times for shear velocities (a) V=1.50, (b) V=0.20 and (c) V=0.01 in a system of height L_y=160. In graph (c), the profile at time 3776 belongs to a transient state with a symmetric velocity profile.

shear regime and the small value of this parameter in the blocks. In the fast shear regime, where we have no blocks, the value of M in the central part of the system away from the walls is as large as this value in the slow and intermediate regimes in shear bands at the walls.

Averaging M in the bulk of the system for different shear velocities, indeed a kink of

M at V_{AB} could be observed (Fig. 6.15).

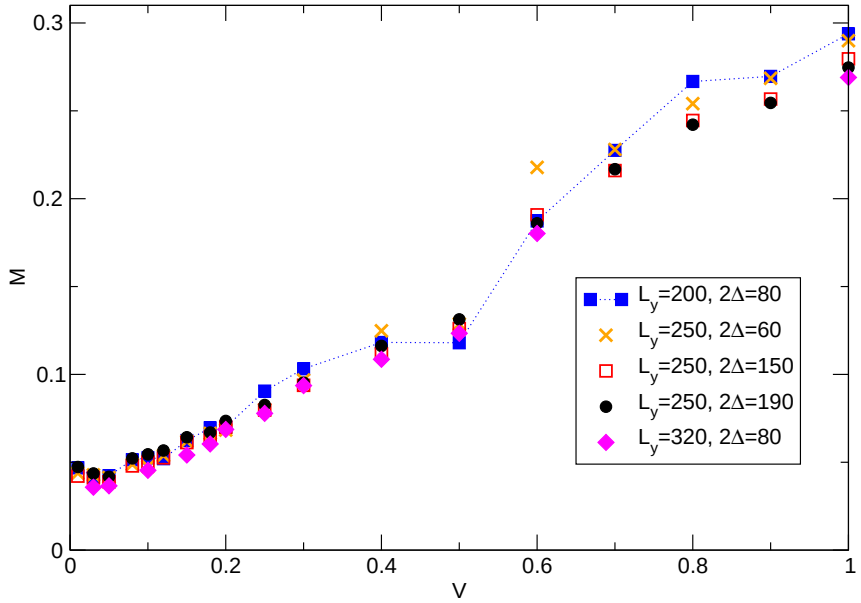

Figure 6.15: Mean mobilization in the bulk as a function of shear velocity for different system heights, measured in a central region of height 2Δ (see legend). The error bars are smaller than the symbol size. In the system with $L_y = 250$, the kink of M at V_{AB} becomes less sharp with increasing Δ, but does not disappear.

6.4 Slip Velocity

The slip at smooth walls is a characteristic feature of the boundary region behavior.

To evaluate the slip velocity at the walls one needs to calculate the average of the surface velocity of particles in contact with the walls at their contact point. The slip velocity in this work is defined as the absolute value of the difference between the wall velocity and the average particle surface velocity at the corresponding wall, v_0^{slip} at the bottom, respectively $v_{L_y}^{\text{slip}}$ at the top wall. To this end all particles in contact with the walls over the whole simulation time in steady state should be considered, and contribute

$$v_0^{\text{slip}} = V + \langle v_{\text{ix}} + \omega_{\text{i}} r_{\text{i}} \rangle_{\text{i , t}} \quad , \tag{6.3}$$

$$v_{L_y}^{\text{slip}} = V - \langle v_{\text{ix}} - \omega_{\text{i}} r_{\text{i}} \rangle_{\text{i , t}} \quad , \tag{6.4}$$

where v_{ix} is the x component of the center of mass velocity of particle i of radius r_{i} with angular velocity ω_{i}.

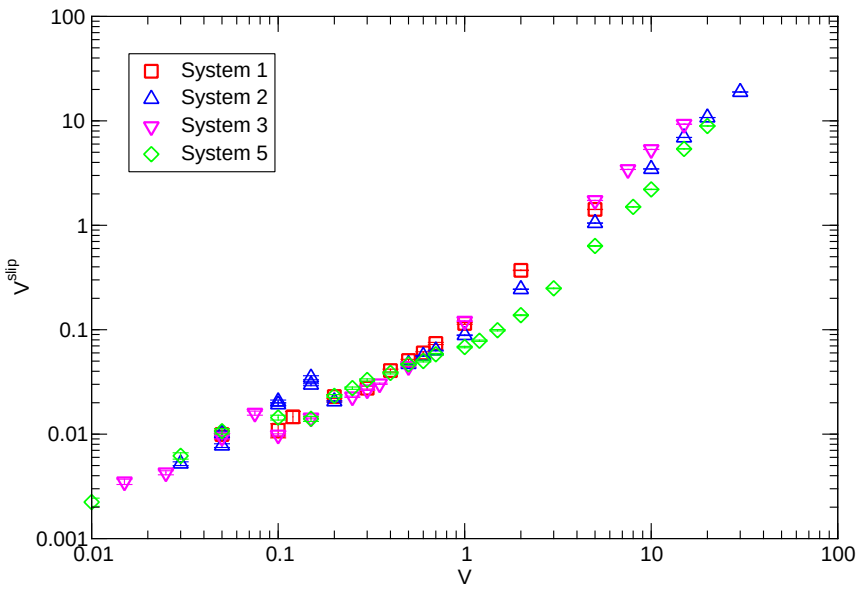

Figure 6.16: Slip velocity v^{slip} (averaged over v_0^{slip} and $v_{L_y}^{slip}$) measured as a function of shear velocity (systems specified in Tab. 5.1). Slip velocity is independent of system size in interval $0.2 \lesssim V \lesssim 1.0$.

My observations show that the slip velocity in a certain shear velocity interval $0.2 \lesssim V \lesssim 1.0$ does not depend on the system size (Fig. 6.16). For larger shear velocities, though the general tendency is the same, slight deviations are observable.

6.5 Conclusion and Discussion

The planar shearing of dense systems of bidisperse as well as polydisperse, non-cohesive, hard, round, dissipative and frictional particles is simulated in two dimensions using contact dynamics. The system is sheared by smooth, frictional walls at constant shear velocities, subjected to a constant normal force. Depending on the shear velocity, the system behavior belongs to one of the three different regimes (from high to low shear velocities): (A) a fluid like state with almost homogeneous shearing, (B) a block like state with symmetric velocity profiles and fluidization only at the walls, (C) a state of broken symmetry, where a block moves essentially with one wall while possessing a shear zone at the other.

System size analysis shows a first order transition from regime C to B, at $V_{BC} \simeq 0.10$ and a continuous transition between regimes B and A starting at $V_{AB} \simeq 0.50$. While I found V_{BC} to be independent of the system size L_y [202], the other boundary of the intermediate shear regime, V_{AB}, is more subtle. For large enough systems it is also

independent of L_y. However, for small system sizes ($L_y < 80$) it becomes hard to determine the boundary between the fast shearing regime (allowing for shear bands in the bulk in the long lasting transient states), and the intermediate regime (with shear bands pinned at the walls).

It should be noted that the characteristics of all three regimes have reached a steady state during all our measurements. For the fast and intermediate regimes this implies a stationary width of the shear zones. For the slow regime, where jumps between the two symmetry related states occur, it means at least a constant histogram of the center of mass velocity. Moreover, after each jump, a constant width of the single shear band is quickly reached and is always the same.

7 Constitutive Laws for Dense Granular Flow Driven by Smooth Walls

An active field of research over the last three decades [204, 205] is the rheology of dense granular flows, which recently benefitted from the introduction of robust and efficient constitutive laws. First identified in planar homogeneous shear flow [29], those laws were successfully applied to various flow geometries [27], such as inclined planes [205], or annular shear devices [76], both in numerical and experimental works [206]. A crucial step in the formulation of these laws is the characterization of the internal state of the homogeneously sheared material in steady flow under given normal stress by the *inertial number* [27, 29], expressing the ratio of shear time to rearrangement time. Hereby the material state is regarded as a generalization of the quasistatic critical state, which corresponds to the limit of $I \to 0$. Once identified in one geometry, those constitutive laws prove to be able to predict velocity fields and various flow behaviors in other situations, with no adjustable parameter [30].

However, assuming a bulk constitutive law to be available, in general, one needs to supplement it with suitable boundary conditions in order to solve for velocity and stress fields in given flow conditions. Recent studies, mostly addressing bulk behavior, tended to use rough boundary surfaces, both in experiments (as in [32, 33, 207]) and in simulations [29, 76, 115, 141, 208], in order to induce deformation within the bulk material and study its rheology. Yet, in practical cases, such as hopper discharge flow [209], granular materials can be in contact with smooth walls (i.e., with asperities much smaller than the particle diameter), in which case some slip (tangential velocity jump) is observed at the wall [20, 21, 35], and the velocity components parallel to the wall can vary very quickly over a few grain diameters. The specific behavior of the layer adjacent to the wall should then be suitably characterized in terms of a boundary zone constitutive law in order to be able to predict the velocity and stress fields.

Constitutive laws were previously studied, in similar model materials, in homogeneous shear flow [29, 31, 60, 140, 210]. In my system, I separate the boundary regions near both walls, from the central one (or bulk region). Unless otherwise specified, the boundary regions have thickness $h = 10$. Near the walls, the internal state of the granular material is different, and separate constitutive laws for the boundary layers and for the bulk material are demanded. While the latter is expected to abide by constitutive laws that apply locally, and should be the same as the ones identified in other geometries or with other boundary conditions [29, 76], the boundary constitutive law is expected to relate stresses to the global velocity variation across the layer adjacent to the wall.

The main results of this chapter have already accpeted to be published in Physical Review E [211].

7.1 Constitutive Laws in the Bulk Region

7.1.1 Friction Law

The steady state values of the inertial number (I_{bulk}) and of the effective friction coefficient μ_{eff} are measured, as averages over time and over coordinate y within the interval $h < y < L_y - h$. μ_{eff} is plotted as a function of I_{bulk} for all different system sizes in Fig. 7.1, showing data collapse for different sample sizes.

The apparent influence of the choice of h on the measured effective friction coefficient and inertial number in the bulk region is presented in Fig. 7.2 for two different system sizes and for two different h values.

One can see that the points with $\mu_{\text{eff}}<\mu_0=0.25$ depend on h. They are shifted to smaller values of I_{bulk} upon increasing h: compare the open and full symbols in Fig. 7.2. This effect is apparent in regimes B and C. It is due to the creep phenomenon (as was also observed in the annular shear cell in [34, 76]), which causes some amount of shearing at the edges of the bulk region, adjacent to the boundary layer. Although the local shear stress is too small for the material to be continuously sheared, the ambient noise level, due to the proximity of the sheared boundary layer, entails slow rearrangements that produce macroscopic shear [212]. Upon increasing h the central bulk region excludes the outer zone that is affected by this creep effect. The critical friction coefficient, from Fig. 7.2, is $\mu_0=0.25$ (below

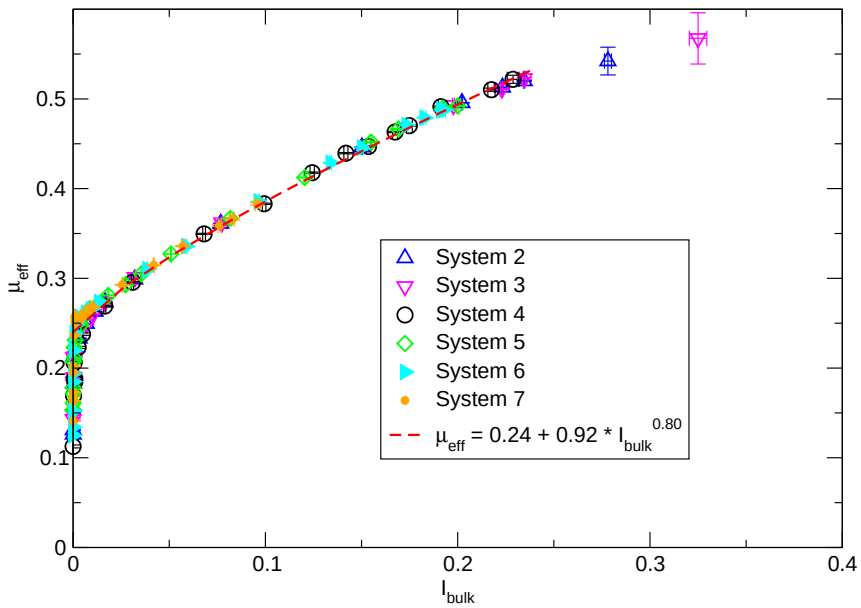

Figure 7.1: μ_{eff} as a function of inertial number in the bulk region for different system sizes (see Tab. 5.1). The error bars are much smaller than the size of the symbols. The fit function is calculated according to Eq. 7.1 for μ_0=0.25. The error bars are much smaller than the size of the symbols.

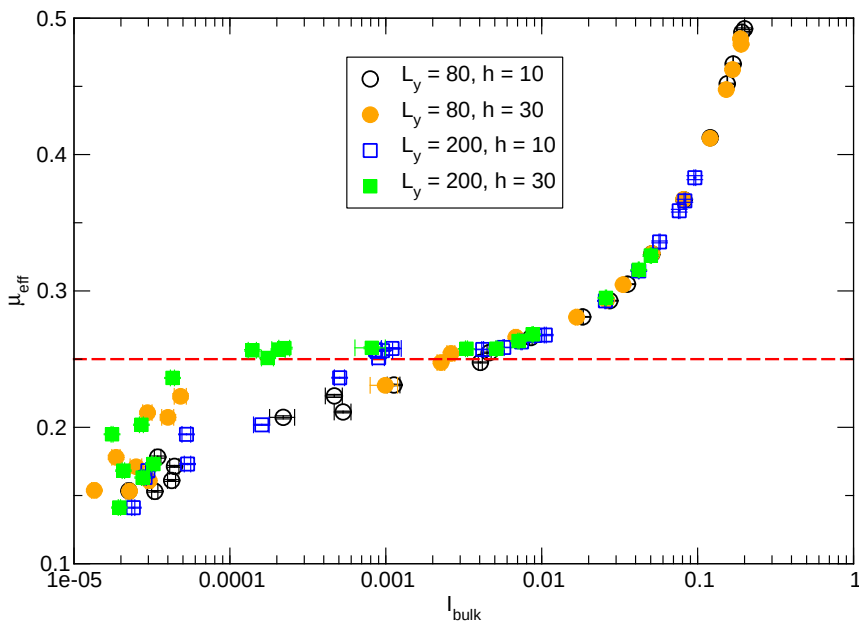

Figure 7.2: Influence of h on μ_{eff} as a function of inertial number in the bulk region (data from systems 5 and 7 in Tab. 5.1).

which the data points are sensitive to the value of h), which is consistent with the results of the literature [29, 34, 60, 76].

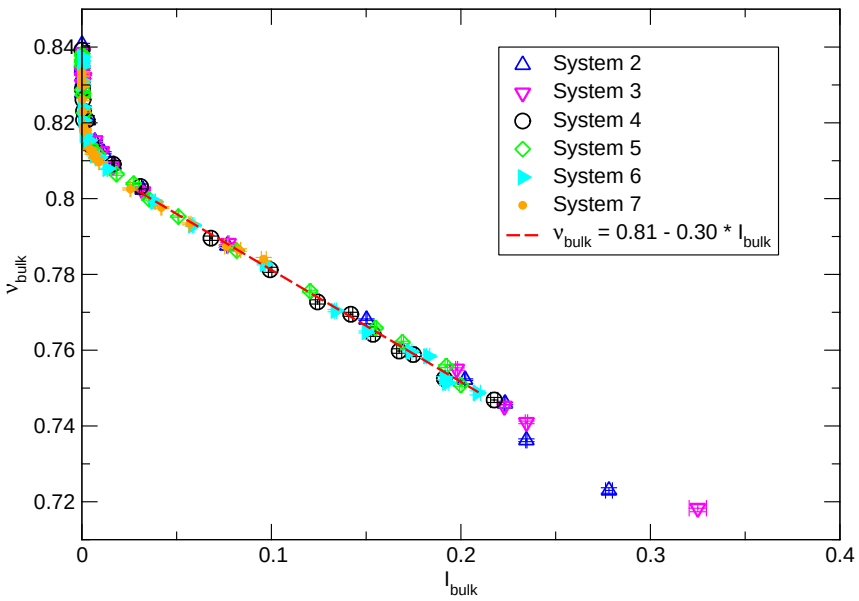

Figure 7.3: ν as a function of inertial number in the bulk region. The error bars plotted are much smaller than the size of the symbols (systems specified in Tab. 5.1).

Fitting $\mu_{\text{eff}} - \mu_0$ with a power law function, as in [127, 213]

$$\mu_{\text{eff}} - \mu_0 = A \cdot I_{\text{bulk}}^B \tag{7.1}$$

the following coefficient values yield good results (see Fig. 7.1):

$$\mu_0 = 0.24 \pm 0.01,$$
$$A = 0.92 \pm 0.05,$$
$$B = 0.80 \pm 0.05.$$

7.1.2 Dilatancy Law

I focus now on the variation of solid fraction ν as a function of inertial number within the bulk region. ν is averaged over time, once a steady state is achieved, within the central region, $h < y < L_y - h$. Function $\nu_{\text{bulk}}(I_{\text{bulk}})$ is plotted in Fig. 7.3 for different system sizes, leading once again to a good data collapse. The $\nu_{\text{bulk}}(I_{\text{bulk}})$ is fitted for all data sets in the interval $0.03 < I_{\text{bulk}} < 0.20$ with the following linear function:

$$\nu_{\text{bulk}} = 0.81 - 0.30 \cdot I_{\text{bulk}} \tag{7.2}$$

which is consistent with the linear fit in [29, 34, 60, 76].

7.2 Constitutive Laws in the Boundary Layer

In order to characterize the state of the boundary layer of width h adjacent to the wall (recall $h = 10$ by default), a local inertial number I_{boundary} is used, which is defined as follows:

$$I_{\text{boundary}}^{\text{top/bottom}} = \sqrt{\frac{m}{\sigma_{yy}}} \times \left\langle \frac{\Delta v^{\text{top/bottom}}}{h} \right\rangle_t , \tag{7.3}$$

with

$$\begin{aligned} \Delta v^{\text{top}} &= V - v_x(L_y - h) \\ \Delta v^{\text{bottom}} &= v_x(h) + V \end{aligned} \tag{7.4}$$

7.2.1 Friction Law

Figure 7.4 is a plot of μ_{eff} as a function of the inertial number I_{boundary} in the boundary layer for all different system sizes.

In steady state the value of μ_{eff} in the boundary layer has to be equal to the averaged one in the bulk (see Fig. 6.5). The observed shear increase (in regime A) or localization (in regimes B and C) near the smooth walls entails larger values of inertial numbers in the boundary region. An equal value of μ_{eff} in the bulk and in the boundary zone requires that the graph of the function $\mu_{\text{eff}}(I_{\text{boundary}})$ is below its bulk counterpart in the inertial number interval measured.

In Sec. 7.1 we have seen that the friction law can be identified in the bulk independently of h (see Fig. 7.2), as an intrinsic constitutive law. According to the definition of I_{boundary} in Eqs. (7.3) and (7.4) any constitutive relation involving I_{boundary} should trivially depend on h. In shear regimes B and C, there is no shearing in the bulk region, and consequently Δv in the numerator of Eq. (7.3) does not change with h. On multiplying the measured I_{boundary} with the corresponding value of h, thus it is expected that the data points belonging to shear regimes B and C coincide (Fig. 7.5). In regime A, in contrast, the existence of shear in the bulk region leads to an apparent h dependence of the measured Δv. Accordingly, after multiplying I_{boundary} with h, the curves do not merge. The critical effective friction coefficient at which the deviation of the curves begins corresponds to μ_0=0.25 (the dashed horizontal line in Fig. 7.5), in agreement with the results in Sec. 7.1.1. This makes it more difficult to identify a

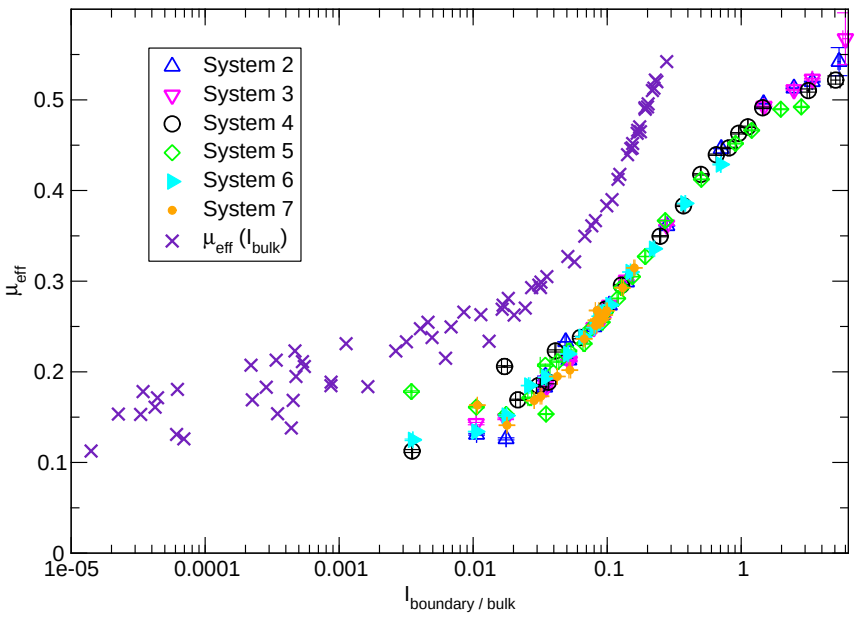

Figure 7.4: μ_{eff} as a function of inertial number in the boundary layer. The error bars plotted are much smaller than the size of the symbols. As $I_{\text{boundary}} > I_{\text{bulk}}$ (shear localization at smooth walls) $\mu_{\text{eff}}(I_{\text{boundary}})$ lies always beneath $\mu_{\text{eff}}(I_{\text{bulk}})$ (systems specified in Tab. 5.1).

constitutive law for the boundary layer, when the bulk region is sheared in regime A.

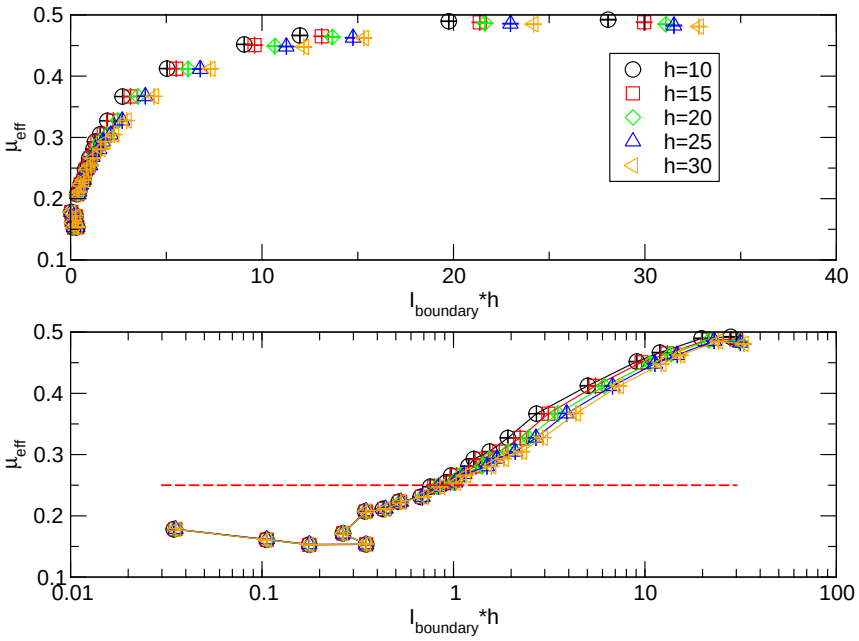

Figure 7.5: μ_{eff} versus $h \times I_{\text{boundary}}$ on linear (top graph) and semi-logarithmic (bottom graph) plots. The dashed horizontal line indicates the critical state value $\mu_{\text{eff}} = \mu_0$=0.25 (data from system 5 in Tab. 5.1).

The behavior of μ_{eff} shown in Fig. 7.5 is apparently anomalous in two respects:

(i) the Δv dependence of μ_{eff} does not seem to follow a single curve (suggesting

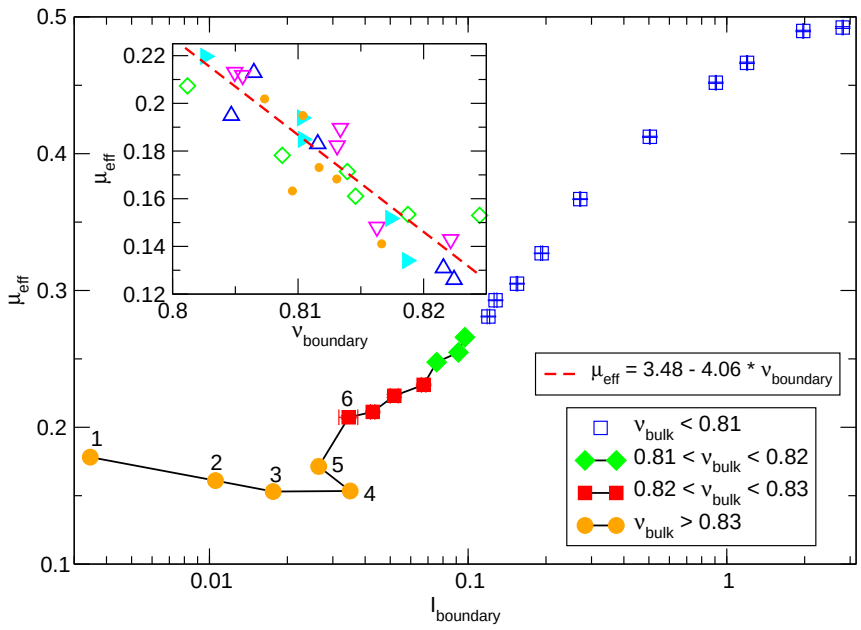

Figure 7.6: μ_{eff} as a function of l_{boundary} (data from system 5 with h=10).The full symbols belong to the states with bulk densities larger than the critical value ν_c=0.81 (see Eq. (7.2)). The full diamonds have a density between 0.81 and 0.82, full squares have a density between 0.82 and 0.83 and full circles have a density larger than 0.83. Inset: μ_{eff} is a decreasing function of solid fraction ν_{boundary} in the sheared boundary layer.

μ_{eff} depends on other state parameters than the velocity variation across the boundary zone).

(ii) μ_{eff} is a decreasing function of l_{boundary} for the first data points, as $h \times l_{\text{boundary}} < 0.2$.

In Fig. 7.6, a closer look is taken at the low l_{boundary} data points, which bear number labels 1 to 6 in the order of increasing shear velocity V. The transition from regime C (one shear band) to regime B (two shear bands) occurs between points 4 and 5, resulting in a decrease of l_{boundary}, as the velocity change across the sheared boundary layers changes from $2V$ to merely V.

In an attempt to identify one possible other variable influencing boundary layer friction, the symbols on Fig. 7.6 also encode the value of the bulk density. One could see then that points 4 and 6, which have different friction levels, although approximately the same l_{boundary}, correspond to different bulk densities. As to issue (*ii*), the decrease of μ_{eff} before the zig-zag pattern on the curve of Fig. 7.6 (data points 1 to 3) is associated to an increase in the boundary layer density with l_{boundary}. This is not the case in all of the systems and these features strongly depend on the preparation and the initial packing density (compaction in the absence of friction). Independent of whether μ_{eff} in regime C increases or not as l_{boundary} increases, μ_{eff} is a decreasing

function of solid fraction ν_{boundary} around a master curve in the sheared boundary layer (the inset of Fig. 7.6), just like μ_{eff} and ν vary in opposite directions in bulk systems under controlled normal stress, as shown in Ref. [29], or as expressed by Eqs. (7.1) and (7.2).

7.2.2 Dilatancy Law

After averaging the profiles of solid fraction ν and inertial number over the whole simulation time in steady state in the boundary region, $\nu_{\text{boundary}}(I_{\text{boundary}})$ graphs are then plotted in Fig. 7.7 for different system sizes. In the bottom graph, $\nu_{\text{bulk}}(I_{\text{bulk}})$ and $\nu_{\text{boundary}}(I_{\text{boundary}})$ are compared for all data sets.

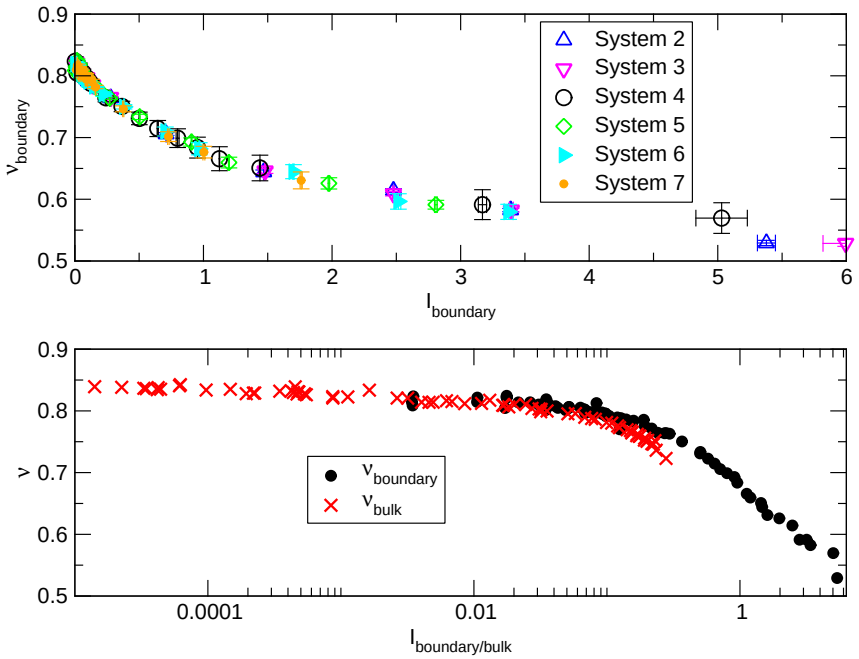

Figure 7.7: ν as a function of inertial number in the boundary layers. The error bars plotted are much smaller than the size of the symbols (systems specified in Tab. 5.1).

7.3 Applications

I now exploit the constitutive relations and other observations reported in the previous sections to try and deduce some features of the global behavior of granular samples sheared between smooth walls.

7.3.1 Transient Time

Transient to Steady State in Regime A

The bulk friction law of Sec. 7.1.1 can be used to evaluate the time for a system to reach a uniform shear rate in regime A, if we assume constant and uniform solid fraction ν and normal stress σ_{yy}, and velocities parallel to the walls at all times. The following momentum balance equation can be written down as:

$$\frac{\partial(\rho\nu v_x)}{\partial t} = \frac{\partial\sigma_{xy}}{\partial y}, \tag{7.5}$$

looking for the steady solution: $v_x = \dot{\gamma}y$. Assuming constant ρ, ν and σ_{yy} one can write:

$$\rho\nu\frac{\partial v_x}{\partial t} = \frac{\partial}{\partial y}\left[\mu_{\text{eff}}(\dot{\gamma})\right]\sigma_{yy}, \tag{7.6}$$

which leads by derivation to:

$$\rho\nu\frac{\partial\dot{\gamma}}{\partial t} = \frac{\partial^2}{\partial y^2}\left[\mu_{\text{eff}}(\dot{\gamma}) - \mu_0\right]\sigma_{yy}. \tag{7.7}$$

Separating the shear rate field into a uniform part $\dot{\gamma}_0$ and a y-dependent increment $\Delta\dot{\gamma}$, and assuming as an approximation just a linear dependency of μ_{eff} on $\dot{\gamma}$, one can rewrite Eq. (7.7) as follows:

$$\rho\nu\frac{\partial\Delta\dot{\gamma}}{\partial t} = \sigma_{yy}\frac{\partial\mu_{\text{eff}}}{\partial\dot{\gamma}}\frac{\partial^2}{\partial y^2}\Delta\dot{\gamma}, \tag{7.8}$$

which is a diffusion equation with diffusion coefficient

$$D = \frac{\partial\mu_{\text{eff}}}{\partial\dot{\gamma}}\frac{\sigma_{yy}}{\rho\nu}. \tag{7.9}$$

The characteristic time to establish the steady state profile (uniform $\dot{\gamma}$ over the whole sample height L_y) is then:

$$T_{\text{SS}} = \frac{L_y^2}{D}. \tag{7.10}$$

A linear fit of function $\mu_{\text{eff}}(I_{\text{bulk}})$ (see Fig. 7.1) in interval $(0.03 < I_{\text{bulk}} < 0.20)$ is:

$$\mu_{\text{eff}} = 0.27 + 1.16 \cdot I_{\text{bulk}}. \tag{7.11}$$

According to Eqs. (3.3), (7.9), (7.10) and (7.11) this leads to:

$$T_{\mathrm{SS}} \simeq 1.56 L_y^2. \tag{7.12}$$

The estimated values T_{SS} for different system sizes are listed in Tab. 5.1. As T_{SS} grows like L_y^2, very long simulation runs become necessary to achieve steady states in tall (large L_y) samples, and some unstable, but rather persistent, distributions of shear rate can be observed [1, 127]. The data for L_y=120 and L_y=200 may still pertain to slowly evolving profiles, even though the constitutive law can be measured in approximately homogeneous regions of the sheared layer over time intervals, in which profile changes are negligible.

Transition from One Wall to the Other in Regime C

As stated in Sec. 6.1, in regime C the asymmetric velocity profiles can be regarded as steady states and the switching stages in which the shear band changes sides are transient states in which the shear stress is not uniform throughout the granular layer. I now try to estimate the characteristic time for such transitions. Taking the whole bulk region as a block of mass M moving with the velocity of the top wall V, a transition to a block of velocity $-V$ with acceleration A will take:

$$T_{\mathrm{transition}} = \frac{2V}{A}, \tag{7.13}$$

in which the acceleration A is equal to:

$$A = \frac{(\sigma_{xy}^{top} - \sigma_{xy}^{bottom}) L_x}{M}. \tag{7.14}$$

Substituting M=$\rho\nu L_x L_y$ and $\sigma_{xy}^{top} - \sigma_{xy}^{bottom}$=$\Delta\mu\sigma_{yy}$ with $\Delta\mu$=$\mu^{top} - \mu^{bottom}$ one gets:

$$T_{\mathrm{transition}} = \frac{2\rho\nu V L_y}{\Delta\mu\sigma_{yy}}. \tag{7.15}$$

Accordingly, the transition time increases proportionally to the shear velocity and to system height L_y. Using $\nu \simeq 0.84$, $\sigma_{yy} = 0.25$ and taking $\Delta\mu \simeq 0.05$ as a plausible value in shear regime C (see Figs. 6.3 and 7.5) I calculate $\frac{T_{\mathrm{transition}}}{V}$ as a function of system height L_y. In Fig. 7.8 these calculated times are compared to transition times that are measured as explained in the caption of Fig. 6.2.

Admittedly, one does not observe only direct, sharp transitions in which localization

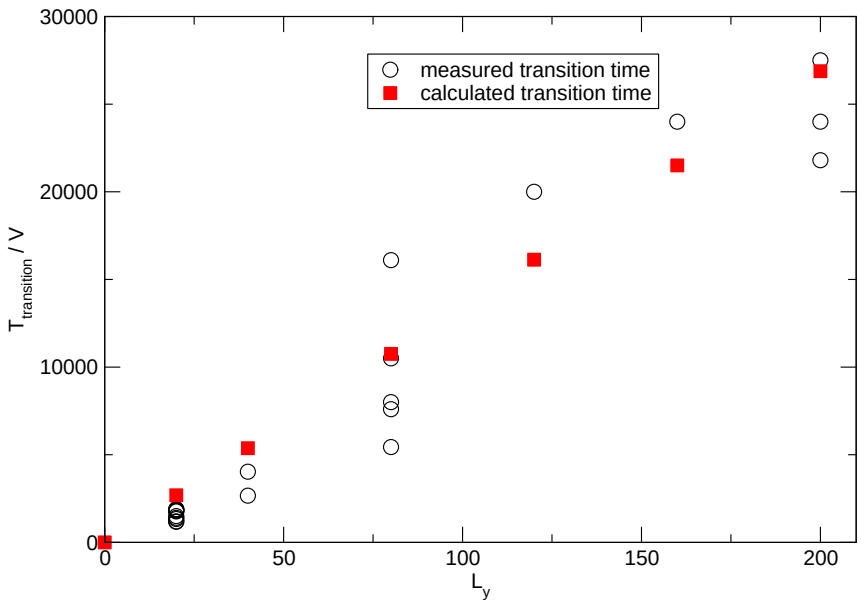

Figure 7.8: Transition time divided by the shear velocity as a function of system height. The full symbols show the calculated data point and the empty ones the measured ones.

changes from one wall to the opposite one. Some transient states are more uncertain and fluctuating, and the system occasionally returns to a localized state on the same wall after some velocity gradient has temporarily propagated within the central region. The data points of Fig. 7.8 correspond to the well-defined transitions. The comparison between estimated and measured transition times is encouraging, although the value of $\Delta\mu$ in (7.15) is of course merely indicative (it is likely to vary during the transition), and the origin of such asymmetries between walls is not clear.

7.3.2 Transition Velocity V_{AB}

μ_0=0.25 from the power law fit in Eq. (7.1) corresponds to the minimal value of the bulk effective friction coefficient, the critical value below which the granular material cannot be continuously sheared (except for local creep effects in the immediate vicinity of an agitated layer).

Fig. 7.9 gives the value of the inertial number in the boundary region, such that the boundary friction coefficient matches μ_0=0.25:

$$\mu_0 = 0.25 \Rightarrow I_{\text{boundary}}=0.086 \pm 0.005. \tag{7.16}$$

Thus for $I_{\text{boundary}} \lesssim 0.086$ no shearing is expected in the bulk. According to Eqs. (7.3) and (7.4) this results in V=0.485 $\pm$ 0.028, in very good agreement with the obser-

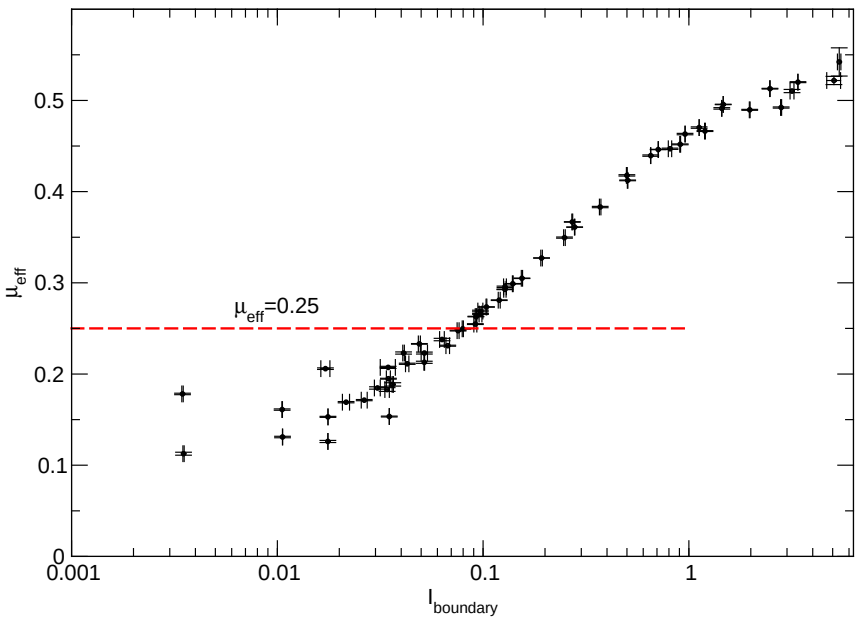

Figure 7.9: The critical I_{boundary}, which corresponds to μ_0=0.25 and determines the critical velocity V_{AB} for the transition from regime A to regime B.

vations reported in Sec. 6.1 ($V_{\text{AB}} \simeq 0.50$).

The explanation of the transition from regime A to regime B is simple: the boundary layer, with a smooth, frictional wall, has a lower shear strength (as expressed by a friction coefficient) than the bulk material. Thus for uniform values of stresses σ_{yy} and σ_{xy} in the sample, such that their ratio σ_{xy}/σ_{yy} is comprised between the static friction coefficient of the bulk material and that of the boundary layers, shear flow is confined to the latter.

7.3.3 Transition to Regime C at Velocity V_{BC}

Although it is not systematically observed, the decreasing trend of μ_{eff} in the boundary layer as a function of Δv or of I_{boundary}, as apparent in Figs. 7.5 and 7.6, provides a tempting explanation to the transition from regime B to regime C. Assuming μ_{eff} for given, constant σ_{yy}, to vary in the boundary layers as

$$\mu_{\text{eff}} = \mu_0 - \alpha|\Delta v|, \quad \text{with } \alpha > 0, \tag{7.17}$$

one may straightforwardly show that the symmetric solution with $\Delta v = \pm V$, and solid bulk velocity $v_s = 0$, is unstable. A simple calculation similar to the one of Sec. 7.3.1 shows that velocity v_s, if it differs from zero by a small quantity δv_s at

$t = 0$, will grow exponentially,

$$v_s(t) = \delta v_s \exp\left(\frac{2\alpha L_x \sigma_{yy} t}{M}\right), \tag{7.18}$$

until it reaches $\pm V$, with the sign of the initial perturbation δv_s. Transition velocity V_{BC} would then be associated to a range of velocity differences Δv across the boundary layer with softening behavior (i.e., decreasing function $\mu_{\text{eff}}(I_{\text{boundary}})$).

In view of Fig. 7.6, where the BC transition takes place between points 4 and 5, this seems plausible, as the slope of function $\mu_{\text{eff}}(I_{\text{boundary}})$ appears to vanish in that region.

7.4 Conclusion and Discussion

In this chapter, I have investigated shear localization at smooth frictional walls, by means of derived constitutive laws. These constitutive laws are measured separately in the bulk of the system and in the walls' neighboring regions, for a wide variety of system sizes. For this purpose, stress tensor, inertial number and solid fraction were measured locally in the whole system. The constitutive laws in the bulk agree with those in the literature. Data collapse is observed for all different system sizes. Changing the width of the boundary region h, the influence of h on the measured effective friction and solid fraction has been studied. In the last part of this chapter, using the constitutive laws in the bulk, supplemented by an elementary stability analysis, the transition time to steady state in regime A is calculated, which is compared with the simulation time for different system sizes in Tab. 5.1. Afterwards, the transition time from one wall to the other in regime C is estimated. The estimated times are then compared to measured ones. Using the constitutive laws both in the bulk and boundary regions, the transition velocity V_{AB} is predicted, which agrees nicely with the observed one in chapter 6. A second stability analysis explains the symmetry breaking in regime C.

8 Block Formation and Suppression of Slip by Rolling Friction

The study of the boundary effects on granular flow has been an important part in the research field of granular media [18–21, 32–34]. In this chapter, I would like to point out some unusual behavior, when shearing dense granular packings with smooth walls. Performing the same simulations with rough walls in the limit of small size of the roughening particles, I show that such effects are no artifact of shearing with absolutely smooth walls. Attention must be paid to the different definitions of "rough walls" in the literature [21] (cf. Sec. 3.4.2). In this work, *rough* in contrast to *smooth* means that particles are glued to the wall, in some cases with gaps and in the others without any gaps between them. On top of that, both cases can be frictional or frictionless, depending on the Coulomb friction coefficient of the surface exposed to the system's inside. Throughout this chapter, only round particles are considered.

In Refs. [29, 60], the dimensionless inertial number I is defined as a reduced form of shear rate $\dot{\gamma}$ ($I{=}\dot{\gamma}\sqrt{\frac{m}{P}}$) and is used to characterize the global state of the granular material in steady shear flow (cf. Sec. 3.6). Shearing with smooth walls, $\dot{\gamma}$ is not necessarily uniform in the flowing material, and in general it is different from $\frac{2V}{L_y}$, because of wall slip and of stronger gradients near the walls. The shear rate has to be measured locally in such cases (chapter 7). In the following, the macroscopic $I_{\text{global}}{=}\frac{2V}{L_y}\sqrt{\frac{m}{P}}$ is used, which naturally corresponds to the local I for homogeneous shear. In this chapter, I_{global} varies typically between $1.8 \cdot 10^{-3}$ and $1.8 \cdot 10^{-1}$. Here, $V{\lesssim}0.10 \mathrel{\hat{=}} I_{\text{global}}{\lesssim}0.02$ is considered as the quasistatic regime, and for $V{\simeq}0.5 \mathrel{\hat{=}} I_{\text{global}}{\simeq}0.10$, more homogeneous shear could be observed in a small system with $L_y{=}20$.

The main results of this chapter have already been accepted to be published in Physical Review E [214].

8.1 Role of Friction at Smooth Walls

In this section, the effect of the Coulomb friction coefficient between the particles (μ_P) and at smooth walls (μ_W) as well as the effect of rolling friction at smooth walls (μ_{rW}) on the shear behavior of the system are studied. In contrast to shearing with rough walls, the slip velocity leads to inhomogeneous shear in my system. The degree of this inhomogeneity depends on the shear velocity and the system size; while shearing with moderate shear velocities ($I_{global}\simeq 0.1$) leads to almost homogeneous shear, in the slow shear regime ($I_{global}\lesssim 0.02$) persistent shear localization could be observed just at one wall (cf. chapter 6). I would like to emphasize here that the results presented in this chapter belong to a system of height L_y=20, where the shear bands at both walls in the moderate shear regime overlap and give rise to an almost homogeneous shear rate in the bulk. With increasing system size, homogeneous shear sets in at ever larger shear velocities. Slip is present in all shear regimes, though, and the shear bands are localized at the walls [174, 202, 203, 211].

Shearing with walls of large roughness and moderate velocities, almost homogeneous shear without slip has been reported, i.e. possessing just one wide shear band (Fig. 8.10). Shearing much more slowly ($I\lesssim 0.02$), even in such systems shear is localized near just one wall, but the shear bands are wider (Fig. 8.19, see also [60]). In most of the works with rough walls, the time averaging is done over a long period

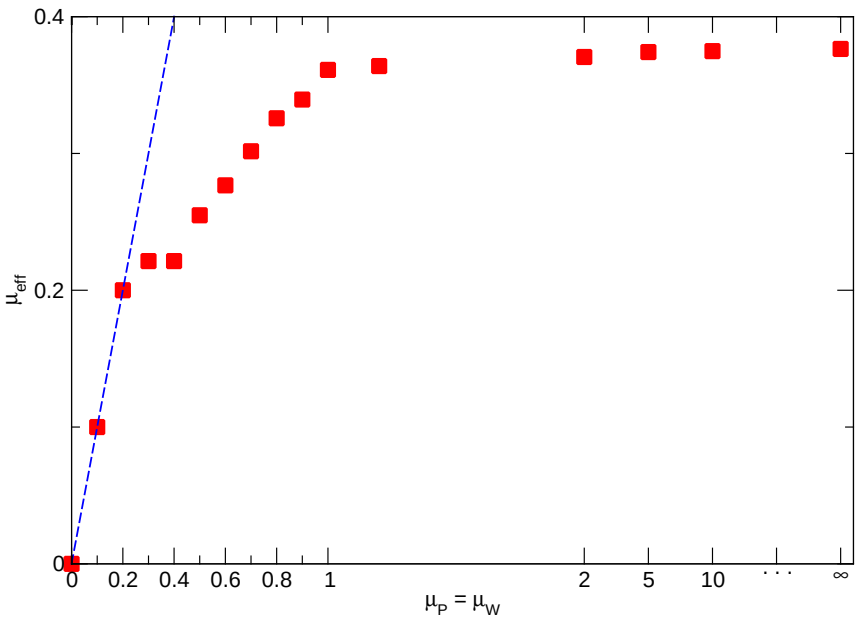

Figure 8.1: The effective friction coefficient μ_{eff} as a function of the microscopic friction coefficient (μ_P=μ_W). The dashed line is μ_{eff}=μ_P. The error bars are smaller than the symbol size.

of time [29], sometimes even up to the whole simulation time [110]. This method leads to an almost linear velocity profile, showing that the filling is sheared on average homogeneously even at very small inertial numbers in the quasistatic regime. Performing the time average with a shorter window reveals the collective behavior of the sheared granular material clearly, even with rough walls for $I \lesssim 0.02$. However, my analysis shows that in a system with smooth walls more persistent blocks are built, which break the symmetry and prevent homogeneous shearing over long shear distances [174, 202, 203].

In a planar system with smooth walls, the rotational velocity of the filling increases towards the walls. The latter drive not only the center of mass velocity, but also the angular velocity of the particles.

8.1.1 Varying Coulomb Friction Globally

Changing the microscopic friction coefficient in the whole system ($\mu_P = \mu_W$), the effective friction coefficient μ_{eff} has been measured, as shown in Fig. 8.1. At a first glance this graph is very similar to the plot presented in other works [29, 110, 170]. Although the shape of the curves are very similar in all of these works, the value of μ_{eff} is slightly different, as it depends not only on μ_P, but also on the inertial number [29, 60, 211] (though all authors claim to measure μ_{eff} in the quasistatic regime), other particle properties like their elasticity [29, 60], and the polydispersity of the filling [215]. The saturation value of μ_{eff} reported in [29, 110] of approximately 0.3 is considerably smaller than the limit of about 0.37 shown in Fig. 8.1. This is due to most simulations in the present chapter not being in the quasistatic regime (except where stated explicitly). The second important difference is the linear increase of μ_{eff} in my simulations, which will be explained later in this section. Consequently, one gets $\mu_{eff}=0$ for $\mu_P=\mu_W=0$, which is not the case in [29, 110, 170]. In all of these works the measured μ_{eff} at $\mu_P=\mu_W=0$ is greater than 0.10. However, I confirm the experimental results stating that μ_{eff} increases with μ_P, but saturates rapidly to a limit value, which is independent of μ_P [110].

8.1.2 Varying Coulomb Friction at Smooth Walls

While I kept $\mu_P=\mu_W$ in the previous part, I now study the effect of only μ_W (contact between particles and the smooth walls) on the shear behavior of the system. Thus,

the effective friction coefficient μ_{eff} has been measured as a function of μ_{W}, while keeping μ_{P} constant. The velocity profiles of the system in steady state and the behavior of the particles directly in contact with the walls for different values of μ_{W} have been also investigated in detail. This is not to be confused with the study [115], where for the flow down a bumpy inclined surface, the sidewalls confine the flow and their friction influences the stability of the steep pile. There, sidewalls confine the system but do not drive it (see also [108]).

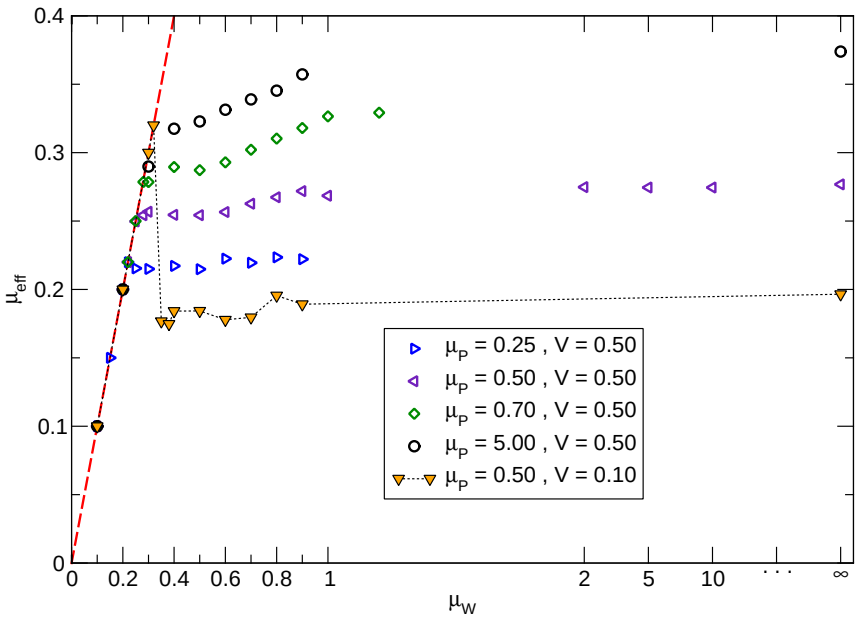

Figure 8.2: The effective friction coefficient μ_{eff} as a function of the microscopic wall friction μ_{W} for different microscopic bulk friction μ_{P} and two different shear velocities V. The dashed line is $\mu_{\text{eff}}=\mu_{\text{W}}$. The error bars are approximately as large as the symbols.

Changing just μ_{W}, the measured μ_{eff} shows a nontrivial reaction (Fig. 8.2). Starting from small values ($\mu_{\text{W}}=0.1<\mu_{\text{P}}$), the effective friction first grows as $\mu_{\text{eff}}=\mu_{\text{W}}$. For $V=0.50$ (moderate shear velocity, i.e. neither quasi-static nor fluidizing), this is terminated by a μ_{P}-dependent critical wall friction coefficient $\mu_{\text{W}}^{\star}$, at which μ_{eff} flattens considerably and finally saturates (pay attention to the abscissa scales in Fig. 8.2). Both $\mu_{\text{W}}^{\star}$ and the saturation value of μ_{eff} grow with increasing μ_{P}, as the different graphs in Fig. 8.2 show. A more interesting behavior is observed for slower shear velocities ($V=0.10$ in Fig. 8.2): While $\mu_{\text{W}}^{\star}$ is here larger than any value for $V=0.50$, the effective friction μ_{eff} drops for $\mu_{\text{W}}>\mu_{\text{W}}^{\star}$ sharply to much smaller values than the corresponding ones for $V=0.50$.

To understand the μ_{eff}-behavior, I check the change of the steady state velocity profiles with μ_{W} (Fig. 8.3), which is in accordance with the shape of the $\mu_{\text{eff}}(\mu_{\text{W}})$ graph (Fig. 8.2). For $\mu_{\text{W}}<\mu_{\text{W}}^{\star}$, this graph shows that the walls are not able to shear the system. Consequently, the whole filling, starting with a linear velocity profile, freezes

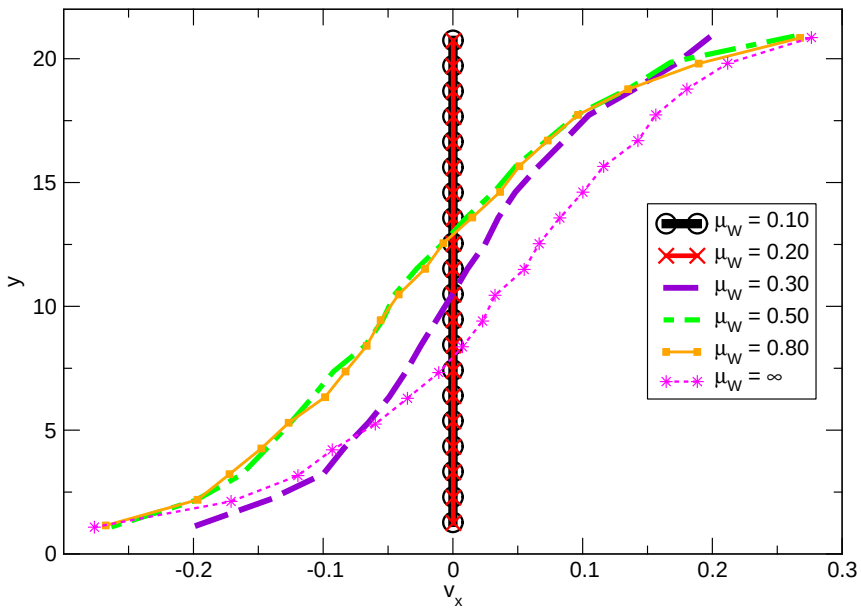

Figure 8.3: Velocity profiles for different values of μ_W with μ_P=0.50 and V=0.50. For $\mu_W<\mu_W^\star$ the walls are not able to shear the system. For $\mu_W>\mu_W^\star$ the width of the velocity profiles increases slightly with μ_W.

after a short shear path into a single block with a very small velocity compared to the shear velocity, leading to pure sliding contacts at the walls, which explains that $\mu_{eff}=\mu_W$ in this interval. Only for $\mu_W>\mu_W^\star$ the walls are able to shear the system, and with increasing μ_W the "quality of shear" improves slightly (the filling is sheared more homogeneously, i.e. the shear localization at the walls becomes weaker), which is reflected in the increasing width of the velocity profiles (Fig. 8.3). For $\mu_W>0.50$ this effect is very small, in agreement with the slight increase of μ_{eff} in this interval. With decreasing shear localization at the walls, the mean shear rate increases in the system and consequently, μ_{eff} increases [29, 60]. The same explanations are valid also for V=0.10. The reason for the sharp drop beyond $\mu_W=\mu_W^\star$ in this case (Fig. 8.2) is not only the increase of $\mu_W^\star$ with decreasing shear velocity but also the decrease of the effective friction coefficient with decreasing inertial number [29, 34, 60, 76, 211]. I conjecture that the increase of $\mu_W^\star$ with decreasing shear velocity is a consequence of low energy transfer to the system at small shear velocities, which requires larger values of μ_W to compensate this deficit [216]. This is valid as long as the block has not yet formed. Otherwise, $\mu_{eff}=\mu_W$ holds true, independently of the shear velocity. As soon as the system starts to shear, the dependency of μ_{eff} on the inertial number ($I \propto \dot{\gamma}$) enters. As for smaller shear velocities, the shear rate ($\dot{\gamma}$) and consequently the inertial number (I) are smaller, the effective friction coefficient is also smaller. Campbell [18, 19] and G. Koval [34] have referred briefly to blocking effects towards small $\mu_W^\star$ values in their works. In both of these works the critical wall friction coefficient $\mu_W^\star$ was considered to be equal to μ_P. The above results show that, while

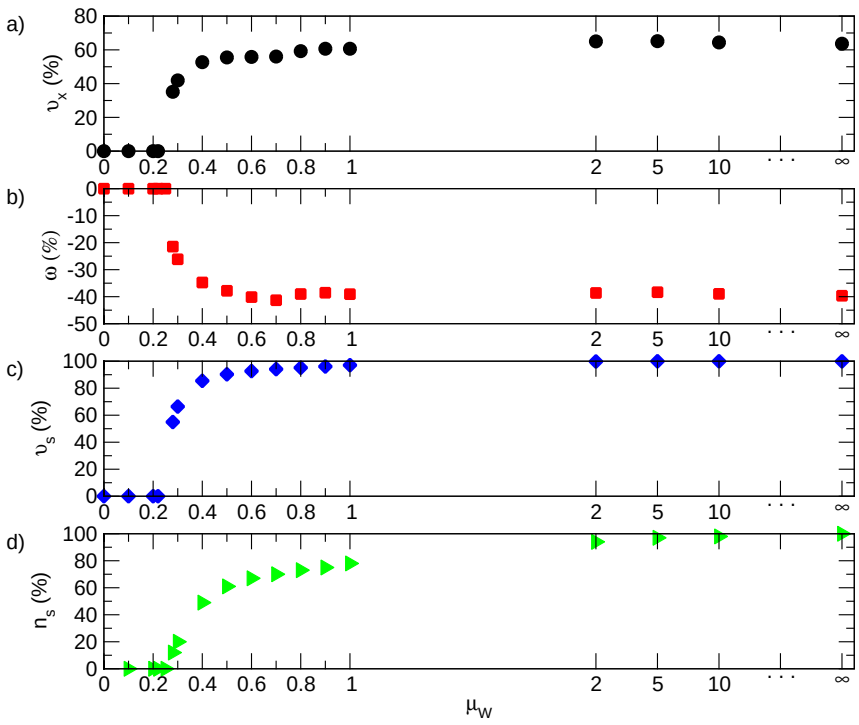

Figure 8.4: For $\mu_W > \mu_W^\star$, with increasing μ_W the averaged center of mass velocity (Eq. (5.8)) (a) and the rotational velocity (Eq. (5.9)) (b) of the particles at the walls grow in such a way, that the surface velocity of their wall contacts (Eq. (5.10)) approaches gradually the shear velocity (c). υ_x and υ_s are expressed in units of the shear velocity (V=0.50) and ω in units of $\frac{2V}{d}$. For $\mu_W > \mu_W^\star$, the fraction of the sticking wall contacts n_s increases with μ_W and saturates to 100% for $\mu_W \to \infty$ (d). The error bars are smaller than the symbol size.

indeed $\mu_W^\star$ increases with growing μ_P, it does so with decreasing shear velocity, but does not reach μ_P in Fig. 8.2. (This turned out to hold true down to $\mu_P \approx 0.32$ in the quasistatic regime and $\mu_P \approx 0.22$ in the intermediate shear regime.).

With 100% sliding contacts at the walls for $\mu_W < \mu_W^\star$, $\mu_{eff} = \mu_W$ is inevitably the result. As soon as the system starts to shear for $\mu_W > \mu_W^\star$, not only the translational but also the rotational movement of particles appears. The rotation of the particles against each other and the walls prevents a pure sliding character of the contacts and keeps the effective friction coefficient at a lower level. My observations show that in the interval $\mu_W > \mu_W^\star$, with increasing μ_W the center of mass and the angular velocity (υ_x and ω respectively) of the particles directly at the walls adapt themselves in such a way, that the surface velocity of the particles at their wall contacts (υ_s) approaches the wall velocity on average (Fig. 8.4 (a)-(c)). Therefore, the amount of sticking contacts at the walls increases, leading to weaker increase of μ_{eff} (Fig. 8.4 (d)). υ_x, ω and υ_s are calculated according to Eqs. (5.8) to (5.10).

The results in Sec. 8.1.1 of this chapter (Fig. 8.1) are in accordance with the results

in the current part. The only difference is that changing μ_P and μ_W simultaneously does not allow to distinguish between the wall and bulk effects. Comparing the graphs in Figs. 8.1 and 8.2, I definitely conclude that the linear behavior of μ_{eff} for $\mu_W<\mu_W^\star$ is not a consequence of $\mu_W<\mu_P$. For $\mu_W>\mu_W^\star$ the saturation value of μ_{eff} is larger in the case $\mu_W=\mu_P$.

Summarizing, increasing the Coulomb friction of smooth walls, the shear rate of the filling increases only slightly when being already above a critical threshold. As the particles at the walls rotate freely, their center of mass velocity does not adopt the shear velocity of the walls.

8.1.3 Rolling Friction at Smooth Walls

Regarding the fact that the rotation of particles at smooth walls facilitates the formation of sticking contacts, leading to suppression of the effective friction coefficient (Sec. 8.1.2), the question arises how the restriction of the rotational degree of freedom of the particles directly at the walls influences the shear behavior of the system. For this purpose, I activated rolling friction μ_{rW} at the walls. In general rolling friction between particles at contact provides a resistance to the relative rolling motion of them [110, 217, 218]. The restriction of the rotational degree of freedom of the particles adjacent to the walls hinders the free adaption of their rotational velocity to make sticking contacts to the wall (Fig. 8.4). Consequently μ_{eff} increases compared to the case without rolling friction at the walls (Fig. 8.5).

Fig. 8.6 shows how far the rolling friction influences μ_{eff} in the system. Here, I chose a system with $\mu_P=\mu_W=0.5$, in which, as shown in Fig. 8.2, the saturation of μ_{eff} with increasing μ_W is almost reached. Increasing now the rolling friction between the particles and the walls μ_{rW}, μ_{eff} increases very rapidly and reaches the saturation value already at $\mu_{rW}\simeq1.0$. The saturation value is about 35% larger than in the case without rolling friction ($\mu_{rW}=0$) at the walls (Fig. 8.6).

The comparison of the saturation value of μ_{eff} measured in Fig. 8.6 and those measured in the work done by N. Estrada *et al.* (Fig. 7 in [110]) show that they have measured much larger values for the effective friction coefficient. The reason is that they shear not only with rough walls, leading to better shearing even with $\mu_W=0$ (see Sec. 8.2), but they also have activated rolling friction in the bulk of the system.

Figure 8.7 (a) shows how the average angular velocity of the particles ω at the walls

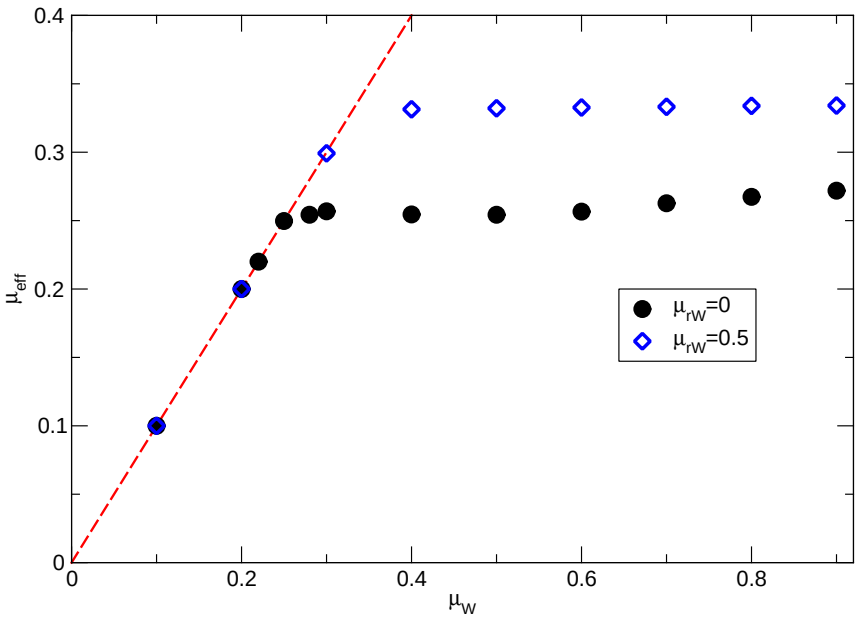

Figure 8.5: The activation of rolling friction (μ_{rW}=0.5) at the walls increases the effective friction coefficient in the system. The results belong to a system with V=0.50 and μ_P=μ_W=0.5. The error bars are smaller than the symbol size.

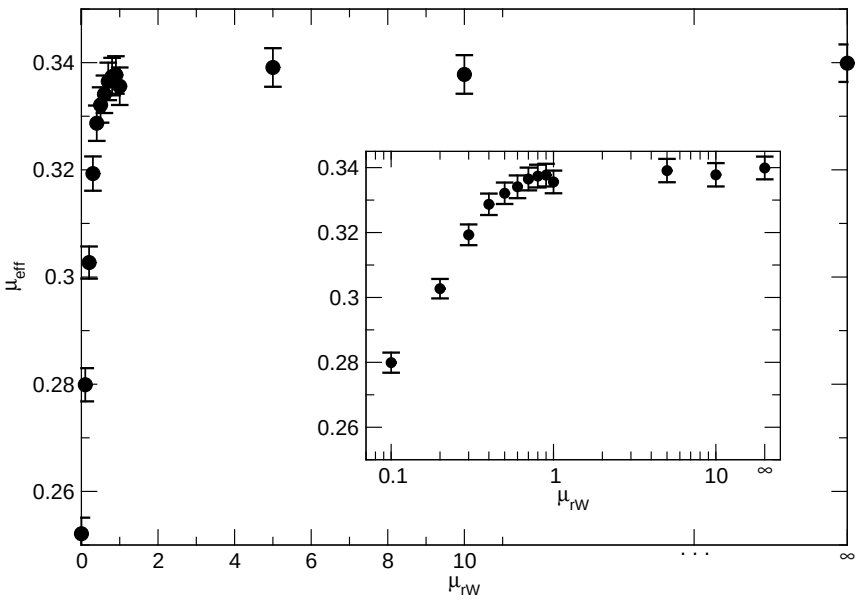

Figure 8.6: The effective friction coefficient increases with μ_{rW} and saturates already at μ_{rW}≃1.0 (inset shows the same data semi logarithmically). The saturation value is about 35% larger than in the case without rolling friction at the walls. The system is sheared with V=0.50 and μ_P=μ_W=0.5.

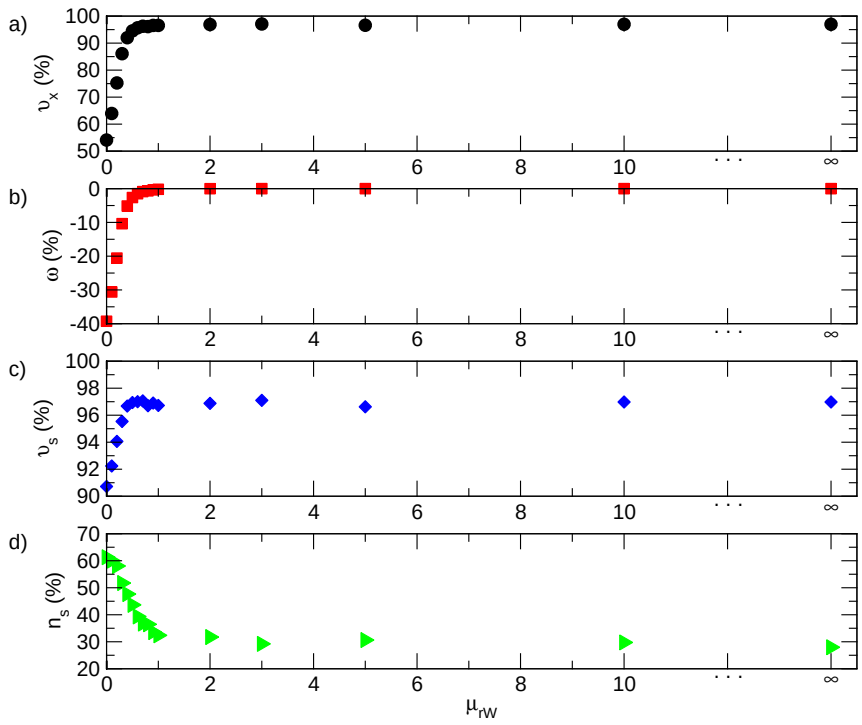

Figure 8.7: With increasing μ_{rW} the angular velocity of the particles at the walls (Eq. (5.9)) drops gradually to zero (b). The average center of mass velocity of these particles (Eq. (5.8)) (a) and the surface velocity at their wall contacts (Eq. (5.10)) (c) increase gradually and approach the shear velocity, but never reach it. υ_x and υ_s are expressed in units of the shear velocity (V=0.50) and ω in units of $\frac{2V}{d}$. The fraction of the sticking contacts at the walls n_s decreases with increasing μ_{rW}, explaining the increase of the effective friction coefficient (d). The error bars are smaller than the symbol size.

decreases with μ_{rW} and finally drops to zero for $\mu_{rW} \gtrsim 1.0$. Simultaneously, the average center of mass velocity υ_x in the same region grows and takes much larger values compared to the case with no rolling friction, but reaches never the shear velocity of the walls (Fig. 8.7 (b)). Consequently, the surface velocity of the particles at their wall contacts υ_s gets very close to, but never reaches the shear velocity (Fig. 8.7 (c), pay attention to υ_s axis.). This small deviation leads to the strong reduction of the fraction of sticking contacts at the walls, as shown in Fig. 8.7 (d). This indicates that the distribution of the particles' center of mass velocities at the wall gets narrower with increasing μ_{rW} and hence the granular temperature at the walls decreases strongly as it is the case at rough walls. As shown in Fig. 8.4 (d), for μ_{rW}=0 and μ_P=μ_W=0.5, more than 60% of the contacts at the walls are sticking. This fraction decreases gradually with increasing rolling friction μ_{rW} at the walls and saturates to about 30%.

Fig. 8.8 demonstrates the effect of the rolling friction on the velocity profiles of a system sheared with a velocity of V=0.50. The velocity profiles for each value of μ_{rW} are measured in the steady state. One can see, how the increase of rolling friction

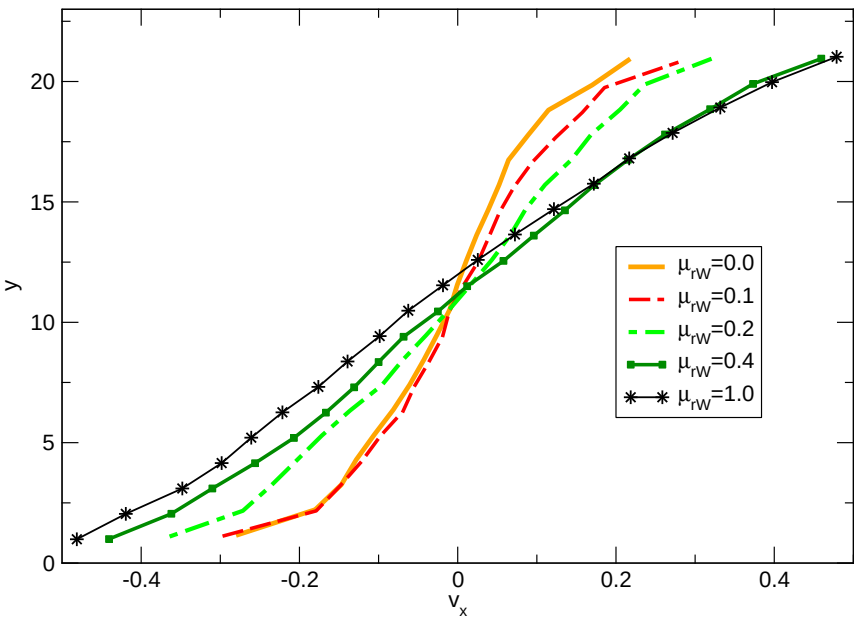

Figure 8.8: Velocity profiles for different values of μ_{rW} in a system sheared with a shear velocity of V=0.50 with μ_P=μ_W=0.50. With increasing rolling friction at the walls, the shear homogeneity improves. The slip velocity essentially vanishes at $\mu_{rW} \approx 1.0$.

at the walls improves the "quality of shear" in the whole system, i.e. the filling is sheared more homogeneously and the shear localization at the walls becomes weaker (compare Fig. 8.8 to Fig. 8.3), reminding of homogeneous shearing with rough walls (see Fig. 8.10 and refer to [3, 19, 34]). Note that the slip velocity essentially vanishes at $\mu_{rW} \approx 1.0$ (cf. also Fig. 8.7.).

To conclude this part of the work, we have observed that the suppression of the rotational degree of freedom of particles at smooth walls by means of activating rolling friction in this region, makes a better adoption of the wall velocity possible. This in turn reduces the slip velocity and improves the shear homogeneity of the filling.

8.2 Rough versus Smooth Walls

8.2.1 Rough Wall Construction

The results presented in Fig. 8.8 raise the question, whether it is possible to make a direct translation between shearing with rolling friction at smooth walls and shearing with rough walls with Coulomb friction (both in addition to usual Coulomb friction).

Therefore, I constructed a system with rough walls with different roughness sizes trying to match different values of rolling friction at the walls (Fig. 8.9).

To construct rough walls, I have covered the inner side of the smooth walls with particles with the same polydispersity as in the bulk of the system, once without any gaps between them and once with gaps of random size (uniformly) between zero and the diameter of the smallest roughness particle (the second construction seeming more realistic). The particles stick to the walls and posses an infinitely large moment of inertia, which prevents their rotation. The diameter of the largest roughness particle d_w varies between $0.01d$ and $3.50d$, where d is the largest particle diameter in the bulk of the polydisperse system (cf. chapter 5). In the limit $d_w \to 0$, I expect the same shear behavior as with smooth walls and for $d_w > d$, I expect the saturation of the effective friction coefficient, corresponding to an essentially unchanging shear behavior in this regime.

8.2.2 The Effective Friction Coefficient

Figure 8.10 shows that with increasing roughness size the filling is sheared more homogeneously and the shear localization at the walls becomes weaker (compare to Fig. 8.8). Simultaneously, the slip velocity at the walls decreases (cf. also [3, 19, 34, 108, 112]) until all particles next to the walls adopt the wall velocity ($d_w \geq 1.0$). Thereafter, the velocity profiles do not change noticeably, except in the region nearest to the walls. With increasing roughness size (and consequently increasing gap size, if present), the particle trapping increases. The trapped particles adopt the velocity of the roughening particles, which is equal to the shear velocity, and hence the shear rate near the walls decreases with increasing roughness size.

Figure 8.11 shows the effective friction coefficient as a function of d_w for V=0.50,

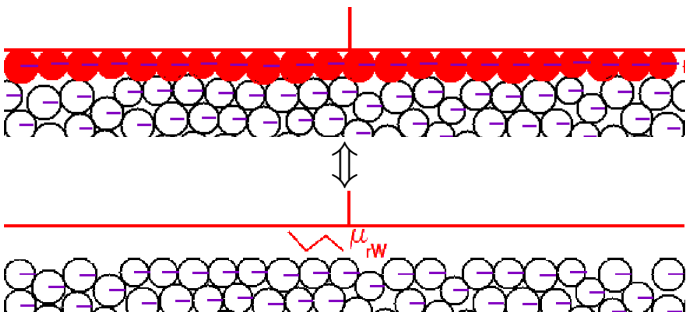

Figure 8.9: The main question is, whether the activation of rolling friction at smooth walls mimics the role of the wall roughness.

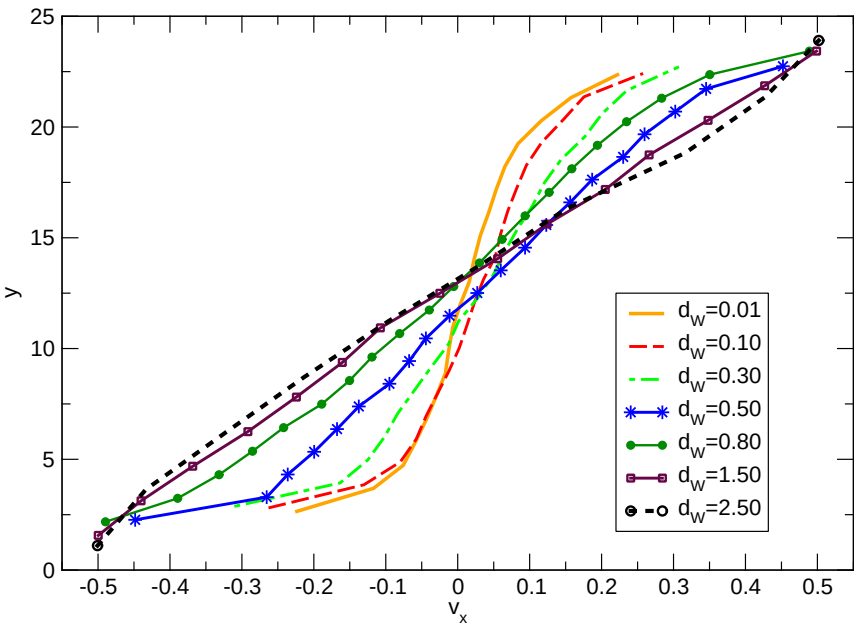

Figure 8.10: Velocity profiles for different values of d_W in a system sheared with a shear velocity of V=0.50 with μ_W=μ_P=0.50. The results belong to a system, where there are no gaps between the particles. With increasing roughness size the slip velocity decreases and the shear homogeneity quality improves. The curvature of the velocity profiles for $d_W \geq 1.50$ at the walls is an indication of particle trapping at rough walls.

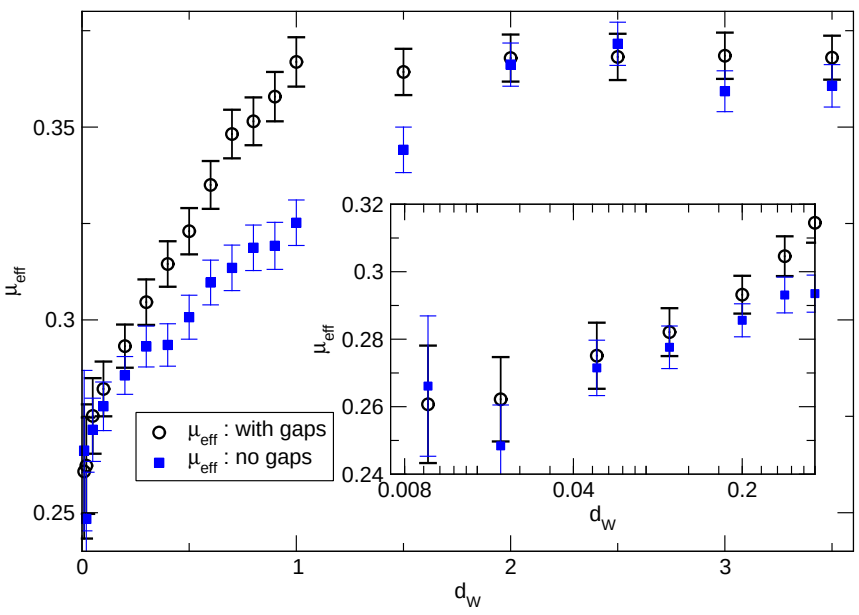

Figure 8.11: The effective friction coefficient grows with increasing roughness diameter (inset shows the same data for $d_W < 0.40$ semi logarithmically). The system parameters are: V=0.50, μ_P=μ_W=0.5 and μ_{rW}=0.

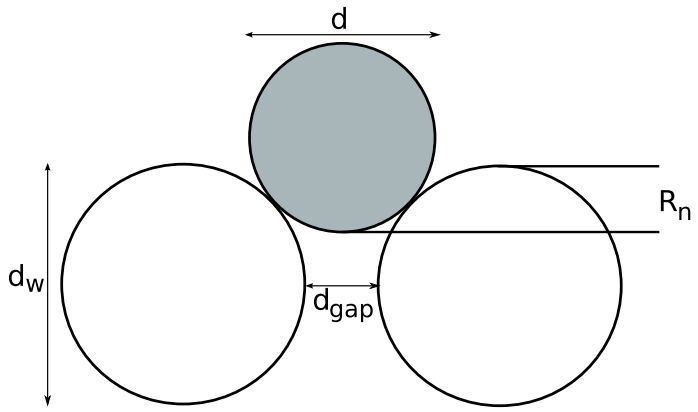

Figure 8.12: For rough walls with gaps, the gap width has to be taken into account in the calculation of the penetration depth.

μ_P=μ_W=0.5 and μ_{rW}=0. With increasing roughness size, μ_{eff} grows gradually and saturates for $d_W \gtrsim 1.0$. For d_W<0.10, the relation is essentially the same with or without gaps between the roughening particles and also the saturation value is about the same. Towards very small roughness size, μ_{eff} approaches the value measured for shearing with smooth walls ($\mu_{eff}\simeq 0.25$) (see the saturation of μ_{eff} in this interval in the inset of Fig. 8.11). For $0.10<d_W<1.0$, the absence of gaps causes a much weaker increase of μ_{eff} and the saturation is not reached before $d_W \gtrsim 2.0$

The linear increase in the interval $0.10 \lesssim d_W \lesssim 1.00$ and the subsequent saturation are consistent with the reported experimental results [34, 219, 220] in the so called *intermediate rough* and *very rough* regimes respectively. In most of the experimental works as well as in the simulations the roughness is expressed in a normalized way, characterizing the extent of penetration of the flowing particles into the roughening layer [21, 34, 219].

To compare my results with those in [34], I extend their expression for the normalized roughness R_n to include gaps (Fig. 8.12):

$$R_n(d_W, d_{gap}) = \frac{1}{2}\left(1 + d_W - \sqrt{(1+d_W)^2 - (d_{gap}+d_W)^2}\right). \tag{8.1}$$

For the case without gaps, we simply have d_{gap}=0. With gaps, as mentioned in Sec. 8.2.1, d_{gap} varies between 0 and the smallest roughening diameter, which is equal to $0.8d_W$ according to chapter 5. As the mean roughness in this case, I thus use

$$\tilde{R}_n(d_W) = \frac{1}{0.8d_W}\int_0^{0.8d_W} R_n(d_W, x)dx, \tag{8.2}$$

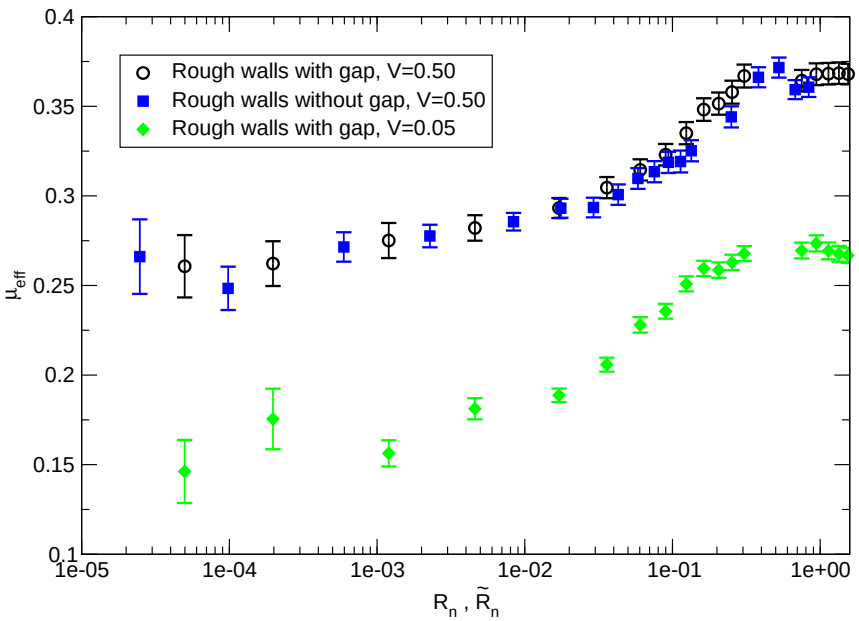

Figure 8.13: The effective friction coefficient as a function of normalized roughness R_n (Eqs. (8.1) and (8.2)). The discrepancy between the two graphs in Fig. 8.11 disappears in this formulation. The system parameters are: V=0.50, μ_P=μ_W=0.5 and μ_{rW}=0. The results in the quasistatic shear regime (V=0.05) are also presented.

in the following. Since the polydispersity of roughening particles is small (20%), for both $R_n(d_W, d_{gap})$ and $\tilde{R}_n(d_W)$, I do not average over d_W.

Fig. 8.13 presents the data from Fig. 8.11 as a function of the normalized roughness, using $\tilde{R}_n(d_W)$ and $R_n(d_W, 0)$ for the cases with and without gaps, respectively. One can see how this leads to a nearly perfect match of the two graphs.

I have included the graph of μ_{eff} as a function of roughness in the quasistatic regime (V=0.05 $\equiv$ I_{global}≃0.01) in Fig. 8.13 as well. The general trend of all μ_{eff} graphs in Fig. 8.13, i.e. the saturation of μ_{eff} in the regimes of small ($R_n \lesssim 0.01$) and large ($R_n \gtrsim 0.5$) roughness and the increase of μ_{eff} in between, is in good agreement with those presented in [34]. Moreover, my results shows that the impact of roughness on μ_{eff} is independent of the shear velocity (in the sense that μ_{eff} for V=0.50 and for V=0.05 differ essentially just by a constant factor). My results meet with high accuracy the ranges defined by the classification of the roughness at the shear interface proposed in some previous works [34]. According to this classification, for R_n<0.01 there is no influence of R_n on the effective friction coefficient (smooth interface), for 0.01<R_n<0.50 the effective friction coefficient grows roughly linearly with R_n (intermediate roughness), and for R_n>0.50 the critical roughness is exceeded and the effective friction coefficient saturates (rough interface). I have to note here that there are several factors influencing the real roughness, which is almost always ne-

glected by calculating R_n: (i) The polydispersity of the roughening particles, (ii) if spheres/disks or hemispheres/semicircles are used and finally (iii) the curvature of the plane or line the roughening particles are glued on.

8.2.3 Roughness versus Rolling Friction

Now let's turn to comparing μ_{eff} in the case of rough walls to the case of smooth walls with rolling friction. For $\mu_{\text{rW}} \to 0$ as well as for $d_{\text{W}} \to 0$, μ_{eff} equals (within the error bars) to the value of the effective friction coefficient at smooth walls, as expected (Fig. 8.14). As Fig. 8.6 shows, the effective friction coefficient saturates for $\mu_{\text{rW}} \gtrsim 1.0$:

$$\mu_{\text{eff}}(\mu_{\text{rW}} = 1) \simeq \mu_{\text{eff}}(\mu_{\text{rW}} \to \infty). \tag{8.3}$$

On the other hand, it is expected that $\mu_{\text{rW}} \to \infty$ induces similar shear properties as the case d_{W}=1, because for $\mu_{\text{rW}} \to \infty$ the particles at the walls loose completely their rotational degree of freedom and behave like roughness particles (albeit their position can change). This allows the conjecture:

$$\mu_{\text{eff}}(d_{\text{W}} = 1) \simeq \mu_{\text{eff}}(\mu_{\text{rW}} \to \infty). \tag{8.4}$$

Eqs. (8.3) and (8.4) give:

$$\mu_{\text{eff}}(\mu_{\text{rW}} = 1) \simeq \mu_{\text{eff}}(d_{\text{W}} = 1), \tag{8.5}$$

which is roughly fulfilled as shown in Fig. 8.14 for the case of rough walls without gaps. Despite the good agreement in the limits μ_{rW}=0 and d_{W}=0 as well as $\mu_{\text{rW}}\simeq$1.0 and $d_{\text{W}}\simeq$1.0, the discrepancy in between is obvious (Fig. 8.14): In the whole interval $0<\mu_{\text{rW}}, d_{\text{W}}<1$ the graph $\mu_{\text{eff}}(\mu_{\text{rW}})$ lies above the $\mu_{\text{eff}}(d_{\text{W}})$. Considering the case (8.5) essentially as equivalence, making the wall particles gradually smaller has a stronger impact than allowing them to roll while keeping their size. One contributing effect could be the possibility of gaps opening in the latter case.

8.2.4 The Role of Roughness Geometry

The question, how just the geometry of the roughness at the walls, independent of the Coulomb friction between the roughening particles and the free particles, influences the effective friction coefficient and thereby the shear behavior of the system, will be

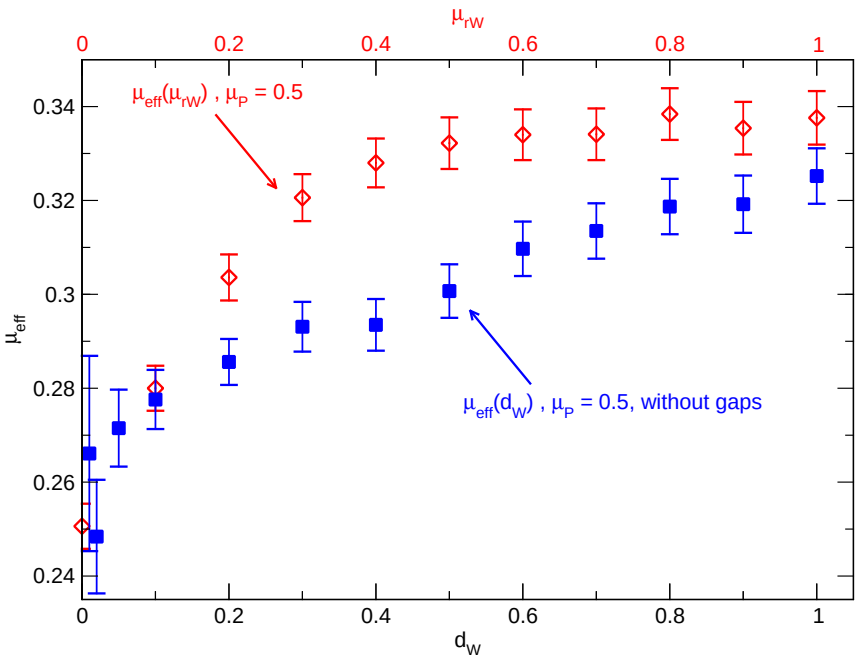

Figure 8.14: A comparison of the effective friction coefficient as a function of the wall roughness size and as a function of the rolling friction coefficient.

investigated in this section. The Coulomb friction between the roughening particles and their free contact partners will be switched off in this part. The microscopic friction coefficient between the particles in the bulk keeps the value μ_P=0.5. Thus, the effective friction coefficient is just a consequence of the wall roughness. As presented in Fig. 8.15, the roughness contributes strongly to the effective friction coefficient at large roughness sizes ($R_n \gtrsim 5 \cdot 10^{-2}$). For $R_n \to 0$, $\mu_{\text{eff}} \to 0$ and with increasing R_n the influence of roughness on μ_{eff} becomes stronger and for $R_n \gtrsim 5 \cdot 10^{-2}$, μ_{eff} takes almost the same values as for the case with μ_P=0.50. This is true for rough walls with gaps as well as those without gaps. For $R_n \lesssim 5 \cdot 10^{-2}$ there is a perfect agreement between the data points of simulations with gaps and those without gaps. For $R_n \gtrsim 5 \cdot 10^{-2}$, the improved particle trapping at rough walls with gaps leads to slightly higher μ_{eff}. These results are in good agreement with those of Koval (Fig. 3.21 in [34]).

8.2.5 Quasistatic Shear in the Limit of Small Roughness

Fig. 8.16 presents the influence of the microscopic friction coefficient at rough walls (μ_W) on the effective friction coefficient in the quasistatic shear regime ($I_{\text{global}} \simeq 0.01$). The interesting effect in this graph is that for R_n<0.01 the curve for μ_W=0.5 lies *between* the ones for μ_W=0.1 and μ_W=0.2.

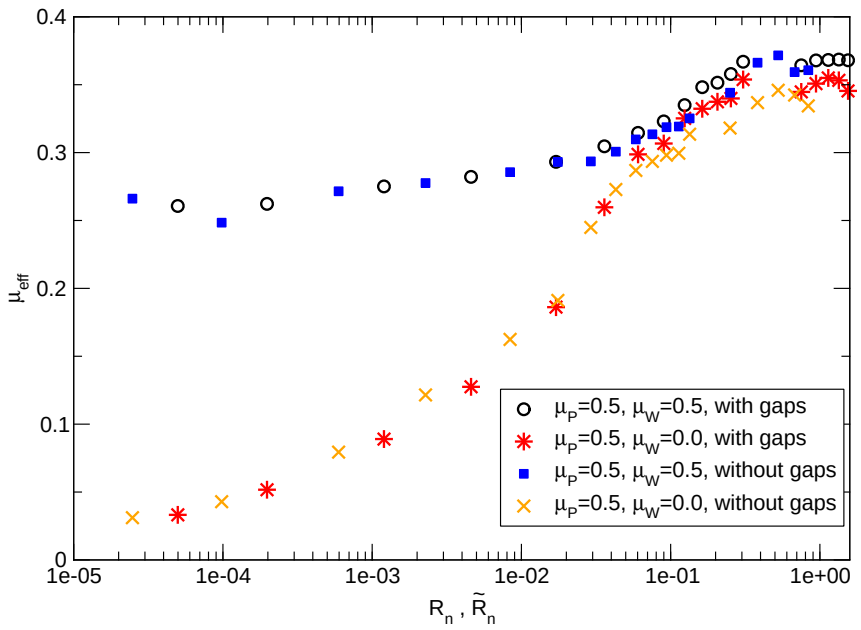

Figure 8.15: The contribution of the wall roughness to the effective friction coefficient with μ_W=0 and μ_P=0.50 has been studied for V=0.50. For large roughness μ_W seems to play almost no roll in determining μ_{eff}. For small roughness in contrast, this parameter plays an eminent role.

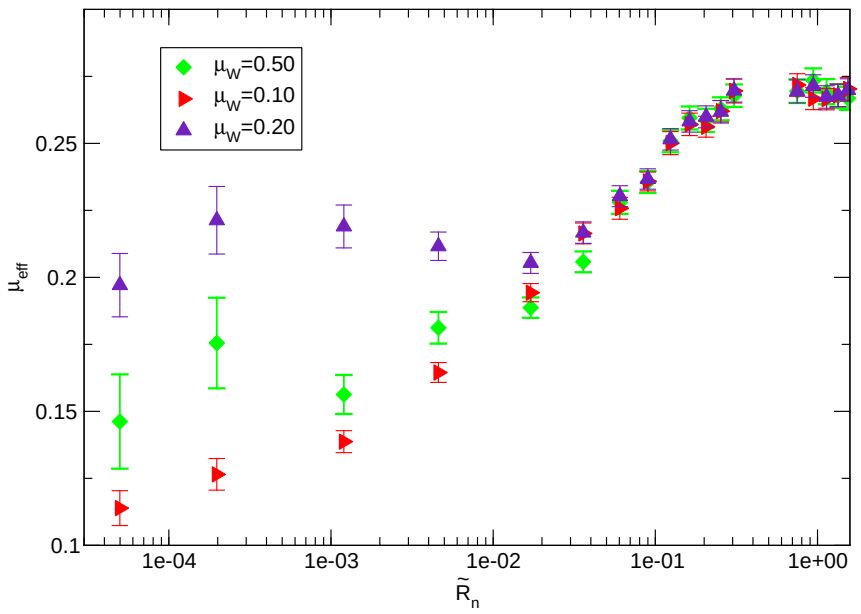

Figure 8.16: While μ_W seems to have no influence on μ_{eff} for $\tilde{R}_n \gtrsim 5 \cdot 10^{-2}$, for $\tilde{R}_n \lesssim 5 \cdot 10^{-2}$ some distinctive features could be observed ($\mu_{eff}(\mu_W$=0.20, 0.30)>$\mu_{eff}(\mu_W$=0.50)).

Plotting μ_{eff} as a function of μ_W for different roughness sizes (see Fig. 8.17) reveals this as the same phenomenon as found for smooth walls (Sec. 8.1.2), albeit less pronounced (Fig. 8.2). Even though with increasing wall roughness the transition at the critical wall roughness $\mu_W^\star$ becomes more and more smeared and disappears gradually, a maximum in μ_{eff} could be observed. Hence, I infer that the results

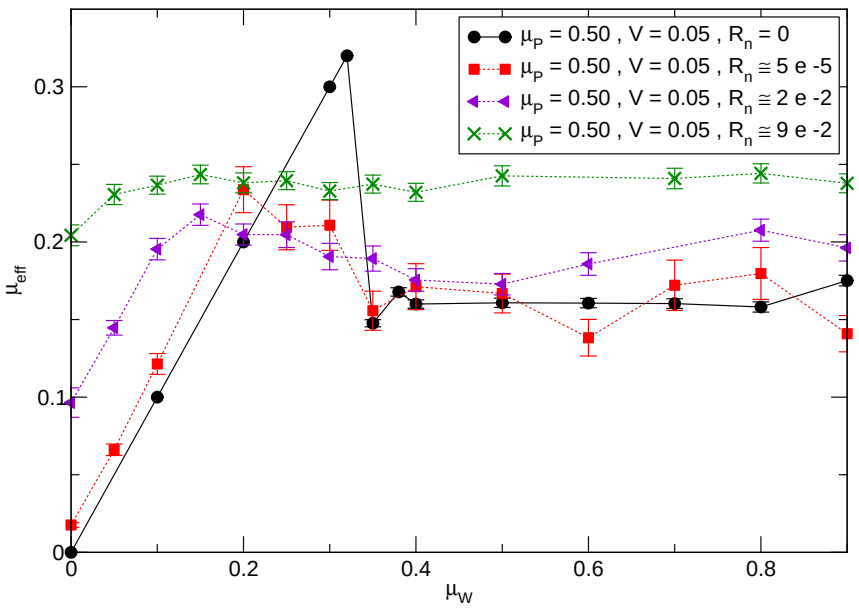

Figure 8.17: Varying μ_W rough walls with small roughness exhibit the same effect as smooth walls in the quasistatic regime (confer Fig. 8.2). With increasing roughness size, the peak disappears and there is no influence of wall friction on the effective friction coefficient.

presented in Fig. 8.2 are no artifact of simulating with perfectly smooth walls.

8.2.6 Rough Walls against Block Formation

One feature of shearing with smooth walls is the persistent symmetry breaking in dense systems in the slow shear regime in the sense, that the velocity profiles stay over a long period of time (and large shear strain) asymmetric [174, 202, 203, 211]. In such cases, almost the whole filling freezes to a block moving with one wall and at the opposite wall there exists a shear band. After a while, the shear band switches to the other wall and consequently the rest of the filling moves again like a block, albeit with the opposite one (Fig. 8.18).

My analysis has shown that the effective friction coefficient in this shear regime is smaller than the critical effective friction coefficient needed to shear the system homogeneously (chapter 7) [211]. Using rough walls, the effective friction coefficient increases in the same regime [29, 34, 76] and no stable block formation has been yet reported. There are some other contributions, reporting on spontaneous shear localizations with very short duration [29, 127] or intermittent particle motion [221–223] in the limit of slow shear. In none of these works, the persistent behavior referred to in this work (see also [174, 202, 203]) is reported. As in a system with rough walls the particles next to the walls are moving with them (the slip velocity is not

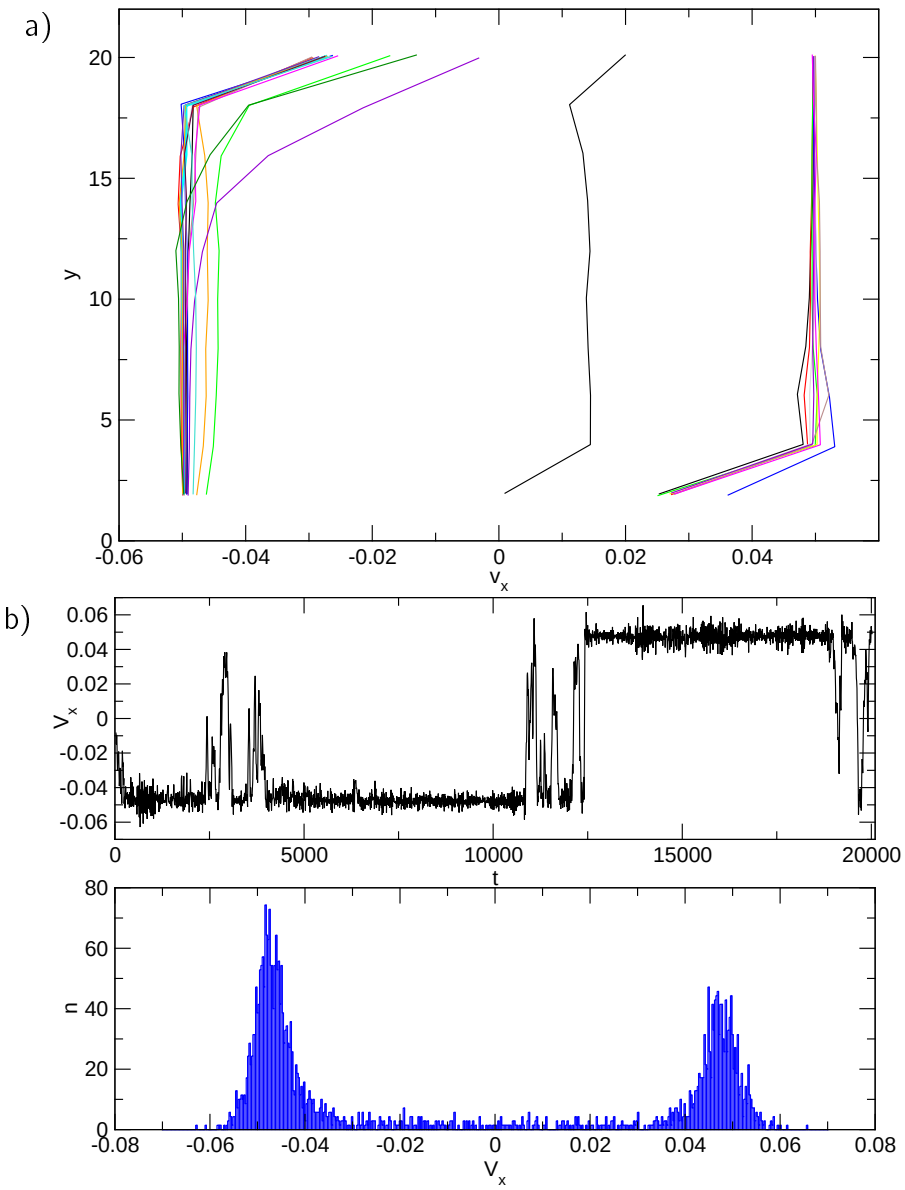

Figure 8.18: (a) Shearing with smooth walls in the slow shear regime leads to block formation. the velocity profiles are asymmetric and mostly there exist just one shear band at one wall or at the other. (b) Center of mass velocity of the filling as a function of time and its Histogram. The two peaks localized at V_x=V and V_x= $-V$ (V is the shear velocity), show that the block moves mostly with the walls.

freely adjustable and the global shear rate increases), I expect that block formation becomes more difficult, which is in fact the case (Fig. 8.19). The tendency to make blocks is observable (some of the velocity profiles in Fig. 8.19 show that one part of the filling moves like a block with the velocity of the adjacent wall), but they are not stable and as the size of the single shear band starting at one wall is large, there does not remain enough space for a large block comparable to those in systems with smooth walls.

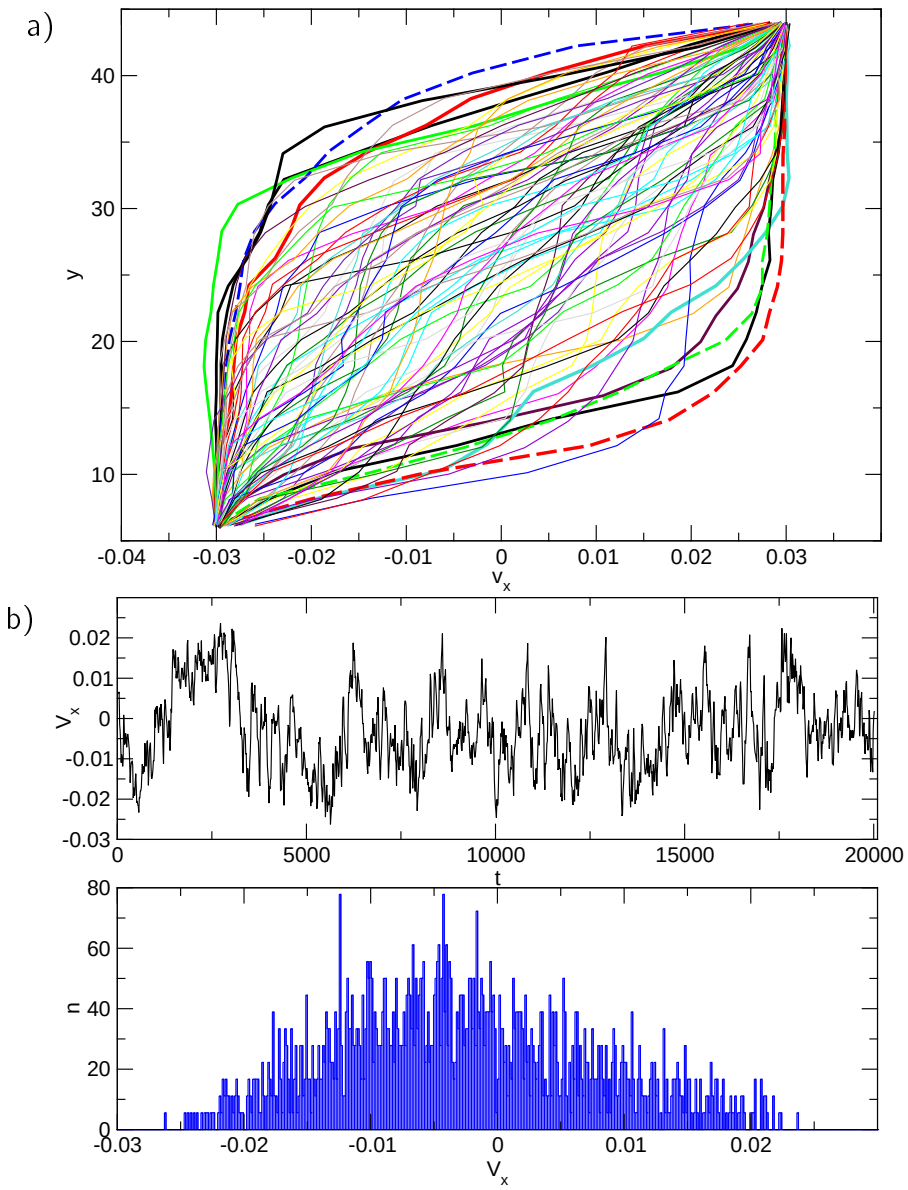

Figure 8.19: (a) Shearing with rough walls in the slow shear regime make the formation of block more difficult. Besides, the shearing penetrates deeper in the system. (b) Histogram of the center of mass velocity of the filling. No apparent localization at V_x=V and V_x= $-V$ exists as in Fig. 8.18.

Here, in contrast to shearing with smooth walls the histogram of the center of mass velocity of the filling does not build two peaks at the V_x=V and V_x= $-V$, but has a wide distribution (Fig. 8.19). Activating the rolling friction at the walls leads to the same system behavior.

8.3 Conclusion and Discussion

In the first part of this chapter, the special features of shearing dry frictional cohesionless granular matter in a planar shear cell with absolutely smooth frictional walls have been presented. Varying the Coulomb friction μ_W at the walls, the slip velocity decreases with increasing μ_W and disappears in the limit of $\mu_W \to \infty$ (see Fig. 8.4). Beneath a critical friction coefficient, the walls are not able to shear the system and the whole filling moves as a block with very small velocities compared to the shear velocity (Figs. 8.1 to 8.4). In this interval μ_{eff} increases linearly with μ_P and μ_W. Beyond this critical value after a short transient saturation could be observed. The critical microscopic friction at the walls $\mu_W^\star$ as well as the saturation value of the effective friction coefficient depend not only on μ_P, but also on the shear velocity (inertial number): While $\mu_W^\star$ increases with decreasing shear velocity and increasing μ_P, the saturation value of the effective friction coefficient decreases with decreasing shear velocity and μ_P. The inertial number dependency of μ_{eff} leads to a sharp drop of μ_{eff} at $\mu_W^\star$ in the slow shear regime ($I_{global} \lesssim 0.02$) (more about the dependency of the effective friction coefficient on the inertial number could be found in [29, 60, 211]). As the velocity profiles reveal, this effect is a consequence of block formation for $\mu_W < \mu_W^\star$ and the reduced μ_{eff} for $\mu_W > \mu_W^\star$ in the quasistatic regime. Interestingly, the measured μ_{eff} before $\mu_W^\star$, where there is no shear, is larger than μ_{eff} after $\mu_W^\star$ in the quasistatic regime. Hence, I conclude that the magnitude of μ_{eff} is not the decisive measure identifying the ability of the interfaces to shear the filling (in contrast to [123]). Campbell has referred briefly to block formation for small friction coefficients at smooth walls, though his simulated systems were not dense. Though he presents some examples on the influence of the microscopic friction coefficient on the shear properties, this issue has not been addressed in his work extensively.

Regarding the fact that the rotation of the particles keeps μ_{eff} at a low level (see Fig. 8.4), rolling friction has been activated directly at the walls (μ_{rW}). The results confirmed my expectations: With increasing μ_{rW} the frustration of the rotation of the particles in contact with the walls increases (Fig. 8.7) and consequently, μ_{eff} increases (Figs. 8.5 and 8.6), leading to more and more homogeneous shearing (Fig. 8.8).

In the second part of this chapter, the results of simulations with rough walls have been presented and I have shown just briefly that my results are in agreement with those of previous contributions [19, 34, 108, 219, 220]. Afterwards, I made a comparison between the measured μ_{eff} by varying the roughness size d_W and μ_{rW} (Fig. 8.14). As the general trend of the curves are very similar, I propose to activate rolling friction at smooth walls to avoid slip, instead of using rough walls. In this way, the system

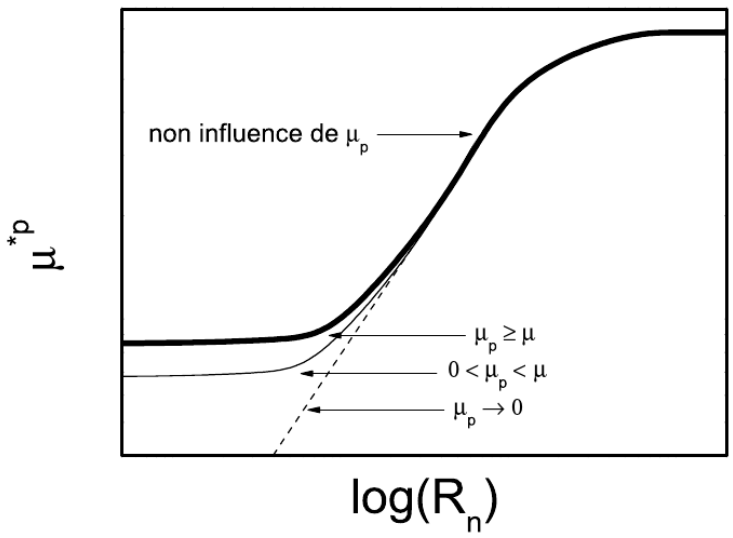

Figure 8.20: μ_{eff} ($\mu^{\star p}$ in this figure) as a function of normalized roughness R_n for different μ_{W}(μ_p in this figure), compared to the microscopic friction coefficient between the particles (μ in this figure) [34].

configuration and preparation becomes more straightforward. The small discrepancies between the results of rough walls and those with smooth walls and activated rolling friction may arise from the restructuring of the particles, when only rolling friction is activated.

I confirm also that for $R_n \lesssim 0.05$, μ_{eff} is influenced strongly by μ_{W} and for $R_n \gtrsim 0.05$ it is practically independent of μ_{W}. This is true for rough walls with and without gaps. This observation strengthens the argument in [34] that for large roughness the normal contact forces at shearing walls drive the flow. I conclude that particle trapping plays less critical role than the normal contact forces at the walls. My results show also, how the roughness reduces the persistence of the blocks and their life time in the slow shear regime in comparison to the case of shearing with smooth walls (see chapter 6 and cf. [174, 202, 203]).

The most interesting part in this section is the limit of small roughness, which is in most of the works considered as dealing with smooth walls [34]. I have shown that the general tendency for the measured μ_{eff} as a function of μ_{W} in the quasistatic shear regime is similar to that of real smooth walls in the limit of small roughness sizes (Fig. 8.17) and deviates with increasing roughness size. The fine resolution of the parameters d_{W} as well as μ_{W} let me claim that my results in Fig. 8.16 contradict the results in [34] in the limit $d_{\text{W}} \to 0$ for $0<\mu_{\text{W}}<\mu_{\text{P}}$. As reported in Fig. 3.82 (a) in [34] (Fig. 8.20) the effective friction coefficient for $0<\mu_{\text{W}}<\mu_{\text{P}}$ is smaller than the one measured for $\mu_{\text{W}} \geq \mu_{\text{P}}$. G. Koval has simulated the quasistatic limit of an annular shear cell with rough walls down to $R_n \simeq 10^{-3}$. Though it is claimed in [34], based on

simulations with different inner wall radii, that the shear geometry plays no role, it remains to be investigated, whether this residual difference to my setup is responsible for the discrepancy.

Part III

Simulation Technique: Development

9 Parallel Contact Dynamics Simulations

In chapter 4, different DEM methods with an emphasis on the contact dynamics method, used throughout this work, have been briefly introduced. In this chapter, after giving a short overview of the parallel version of the other DEM methods, I present a fully parallel version of the contact dynamics method using MPI communication with orthogonal recursive bisection domain decomposition for an arbitrary number of processors. For large enough systems, 100% efficiency has been demonstrated for up to 256 processors using a hierarchical domain decomposition with dynamic load balancing. The method minimizes the computational costs by optimizing the surface-to-volume ratio of the subdomains. The validation of this parallel code is done by numerical simulations of different test systems. The implementation is done in two dimensions and for spherical particles. However, the code is also capable of handling polygonal particles and the extension to three dimensions is straightforward. Compared to the sequential implementation, no influence of the parallelization on simulation results was found. The main results of this chapter have already been published in [157].

9.1 Parallel Version of Different DEM Methods

Molecular dynamics (Sec. 4.1.1) is the most widely used algorithm for discrete element simulations. Interactions are local and therefore efficient parallelization is possible [224–227] with 100% efficiency (see Sec. 9.2 for the definition of "efficiency") for large systems.

The event driven dynamics (Sec. 4.1.2) [165, 166] considers particle interactions of negligible duration compared to the time between collisions. The parallelization of this algorithm poses extreme difficulties, since the collisional events are taken from a *global* list, which in turn is changed by the actual collision. In general, a

naive domain decomposition leads to causality problems. The algorithm presented in [228] conserves causality by reverting to an older state when violated. The best efficiency reached so far is a speedup proportional to the square root of the number of processors [228].

In contrast to ED, lasting contacts between rigid bodies are considered in the realm of (multi)-rigid-body dynamics (Sec. 4.1.3). Parallelization of the FFD method (Sec. 4.3.3) is straightforward and efficient [167, 168], on the other hand, the parallel version suffers also from the undesired approximations in this method. The parallel implementation of the CCP algorithm (Sec. 4.3.1) by the use of Graphics Processing Units (GPU) for large-scale multibody dynamics simulations is presented in [229]. In this chapter, the impact of the parallelization on the numerical solution of the CD method is investigated, going beyond [167, 168, 229].

Providing a parallel CD code is motivated by the need for large-scale simulations of dense granular systems of hard particles. The computation time even scales as $\mathcal{O}(N^{1+2/d})$ with the number of particles in CD [161] (d is the dimension of the system), while it grows linearly with N in MD. However, parallelization of CD poses difficulties as in general the most time consuming part of the algorithm is a global iteration procedure, which cannot be performed completely in parallel. So far, a static geometrical domain decomposition method has been proposed in Ref. [230], and a partially parallel version is introduced in Ref. [231], where only the iterative solver is distributed between shared memory CPUs. In the former work, the force calculation is studied just on 8 processors and in the latter, already with 16 processors the performance efficiency is below 70%. None of these studies deals with computational load balancing during the execution of the code.

9.2 Speedup and Efficiency

Throughout this chapter, the performance of a parallel algorithm is quantified by the usual quantities, the *speedup* and the *efficiency*. Speedup $\mathcal{S}(N_p)$ is the ratio of the run time of the non-parallel version on a single processor to the run time of the parallel version on N_p processors:

$$\mathcal{S}(N_p) = \frac{T_1}{T_{N_p}}, \tag{9.1}$$

and the efficiency $\mathcal{E}$ is

$$\mathcal{E} = \frac{\mathcal{S}}{N_p} \times 100\%. \tag{9.2}$$

9.3 Contact Dynamics Method

9.3.1 CPU Time Analysis

The CD algorithm described in the previous section has three main parts: (i) The contact detection, (ii) the force calculation (iteration), (iii) the time evolution. In this section, the CPU consumption of all these parts is analyzed.

Given a system and the contact detection algorithm, the time consumption of parts (i) and (iii) can be easily estimated. On the other hand, the computational resource needed by part (ii) is strongly influenced by the number of iterations. If one uses extremely high values of N_I, part (ii) will dominate the CPU usage. This led Renouf *et al.* [231] to the conclusion that parallelizing the force calculation is enough.

My view is that the situation is more delicate and it is demonstrated by a simulation in which diluted granular material is compressed until a dense packing is reached [232]. The system consists of 1000 polydisperse disks in two dimensions with friction coefficient μ=0.5. The stopping criteria for the iteration was the fulfillment of any of the two conditions:

(1) The global convergence criterion is fulfilled (see Sec. 4.2.4).

(2) $N_I \geq 200$

Figure 9.1 shows the evolution of the relative CPU time consumption of the different parts of the algorithm. The time stepping contribution always remains less than 5%, and the rest is divided between the other two subroutines. Initially, the contact detection task consumes the majority of the computational time. After a while, clusters of contacting particles form, and the cost of force calculation increases and the iterative solver gradually becomes the most time consuming part of the code. Note that the contribution of the solver saturates to 70% of the total elapsed time. If only the force calculation part is executed in parallel, even with $\mathcal{E}_{\text{force}} = 100\%$, the remaining 30% non-parallel portions set an upper limit to the overall efficiency $\mathcal{E}$ and the speedup $\mathcal{S}$ of the code ($\mathcal{E}_{\text{max}} \approx 80\%$ and $\mathcal{S}_{\text{max}} \approx 4$). Therefore, I aim to provide

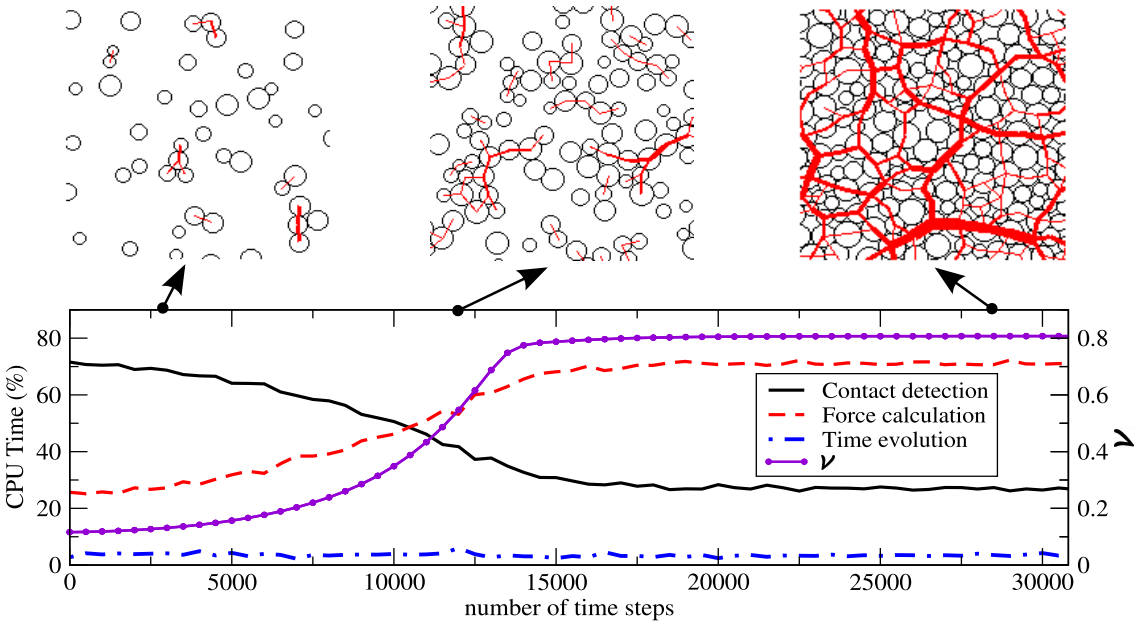

Figure 9.1: The percentage of CPU time consumption (lines) and the packing fraction ν (purple line, full circles) as a function of time. The insets show typical configurations of particles at different packing fractions. The thickness of the inter-center connecting red lines is proportional to the magnitude of the contact force.

a fully parallel version of CD which operates efficiently in all density regimes.

9.3.2 Sequential versus Parallel Update Scheme

As I pointed out in Sec. 4.2.4, the problem of finding the unilateral frictional contact forces that satisfy the constraint conditions cannot be solved locally in a dense granular system. In order to evaluate the new value of a single contact, one has to know the new values of the adjacent contact forces, which are unknown as well, i.e. all contact forces are coupled in a cluster of contacting particles. Note that this is a consequence of the infinite stiffness of the particles; a single collision influences the entire network of contact forces between perfectly rigid particles. This problem is solved by iterating through all contacts many times until a given precision is reached.

Similarly to solving the Laplace equation, the information about a disturbance (e.g. collision of a new particle) appearing on one side of a cluster must diffuse through the whole cluster to satisfy the constraints. Actually, the iteration scheme is very similar to two traditional schemes for solving a set of linear equations [233], albeit with nonlinearities introduced by the change of contact states (repulsive vs. force-less,

sticking vs. sliding): the Jacobi scheme and the Gauss-Seidel scheme, corresponding to parallel and sequential contact updating, respectively.

Here, I denote (i) *sequential*, where the contacts are solved one by one using always the newest information available, which is a mixture of new and old values, (ii) *parallel*, where all contacts are updated using the old values, and substituted with the new ones at the end of the iteration step. Needless to say that the second case is favored for parallel applications but instabilities may appear (like when combining the Jacobi scheme with Successive Over-Relaxation [233]). To study its impact, a mixed method is investigated, where a fraction p of the contacts are updated in parallel and the rest sequentially. First, a static homogeneous packing is generated by applying an external confining pressure [232]. Next, the inter-particle forces are set to zero, while the positions of the particles and the boundary conditions are kept fixed. Now the code recalculates the contact forces within one time step with an unconstrained number of iterations until the convergence is reached. I check how many iteration steps are needed to find a consistent equilibrium solution with a given accuracy threshold. The results are shown in Fig. 9.2(a).

It turns out that, on average, the number of iterations N_I to reach a given accuracy level increases with increasing p. For high values of p, fluctuations appear and beyond $p_c \approx 0.65$ the iterative solver is practically unable to find a consistent solution. I discuss the consequence of this behavior for the parallel version of CD in Secs. 9.4 and 9.5.

In order to investigate the dependence of p_c on the properties of the contact network, snapshots of the structure during the time evolution of the system in the simulation are taken, which are presented in Fig. 9.1. The same procedure as mentioned above is then applied to each of these samples to obtain p_c. The results are shown in Fig. 9.2(b). In dilute systems, the contacts form small isolated islands and the resulting set of equations is decomposed into smaller independent sets, so that even a completely parallel update scheme (p_c=1.0) can be tolerated. However, the contact network in dense systems forms a set of fully coupled nonlinear equations which converges only if the parallelness factor p is less than $p_c \sim 0.65$. By varying the system size and the friction coefficient, it could be concluded that p_c is mainly influenced by the degree of coupling between the equations which is reflected in the connectivity of the sample Z (see Fig. 9.2(b)).

Thus, the results of my numerical simulations reveal that the sequential update scheme is quite robust and the force convergence is reached smoothly, while the fully parallel update scheme is highly unstable in dense systems. However, there is a limit

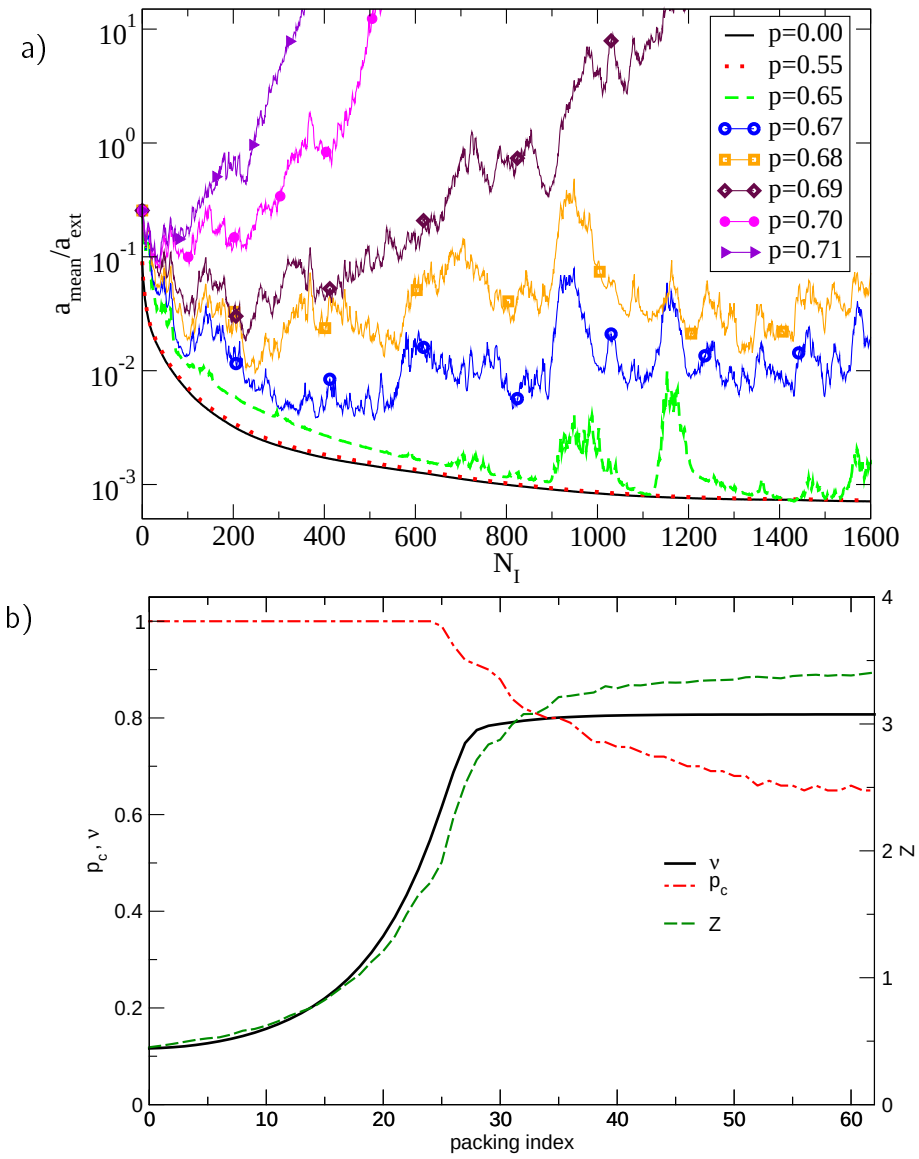

Figure 9.2: (a) The mean acceleration of the particles a_{mean} scaled by $a_{\text{ext}}=2\bar{r}P_{\text{ext}}/\bar{m}$ (where $\bar{r}$ and $\bar{m}$ are the mean particle radius and mass, respectively, and P_{ext} is the external pressure) in terms of the number of iterations N_I for several values of the "parallelness" p (cf. text). These results belong to the dense packing in the right panel of Fig. 9.1. (b) The critical parallelness ratio p_c, the average coordination number Z, and the packing fraction ν for several configurations obtained during the time evolution of the system in the simulation presented in Fig. 9.1.

of parallel update for which the iteration remains stable. This is important because the domain decomposition method allows for a sequential update only in the bulk of each domain, while the boundary contacts are updated in a parallel way (cf. section 9.4.1). This analysis suggests that the ratio of bulk contacts to boundary ones after the decomposition should never fall below 1. Fortunately, this is assured in a domain decomposition context anyway.

9.4 A parallel Version of the CD Algorithm

9.4.1 The Parallel Algorithm

A parallel version of the CD algorithm based on the decomposition of the simulation domain is introduced in this section. The main challenge is to properly evaluate the inter-particle forces when the contact network is broken into several subnetworks assigned to different processors. The parallelization presented in this section is valid only for spherical particles (disks in 2D), but it is straightforward to extend it for other shape types.

At the beginning of the simulation, a domain decomposition function is called to divide the system between N_p processors. Regarding the fact that neither the performance of the computing environment nor the density distribution and the internal dynamics of the system are known initially, a uniform distribution for all relevant factors is assumed and initially the simulation domain is geometrically divided into N_p parts with the same volume. The details of the hierarchical decomposition method are explained in Sec. 9.4.2.

After establishing the domains, the particles are distributed among the processors. Each processor maintains its set of *native* particles, the center of mass of which lie within its domain. The next task is to identify in each domain the *boundary* particles, i.e. those particles which may be in contact with particles in other domains, as this information should be passed to the neighbors. Two particles may come into contact if the gap is smaller than $2v_{\max}\Delta t$, where $v_{\max}$ is the maximum velocity in the whole system. So the maximal distance between the centers of mass of two particles, which may come into contact is

$$d \leq 2r_{\max} + 2v_{\max}\Delta t, \tag{9.3}$$

where $r_{\max}$ is the radius of the largest particles. This distance also defines the width of the *boundary region* in which particles may have contact with particles outside a processor's domain, see also Fig. 9.3.

While $r_{\max}$ is constant during the simulation, $v_{\max}$ varies in time and space. For reasons described in Sec. 9.4.2, a global upper limit ℓ for the boundary size is used, which is unchanged during the whole simulation. It was explained in Sec. 4.2.1, that the displacement of the particles must be small compared to particle size for contact dynamics to be valid. Therefore it is legitimate to define the upper limit for the

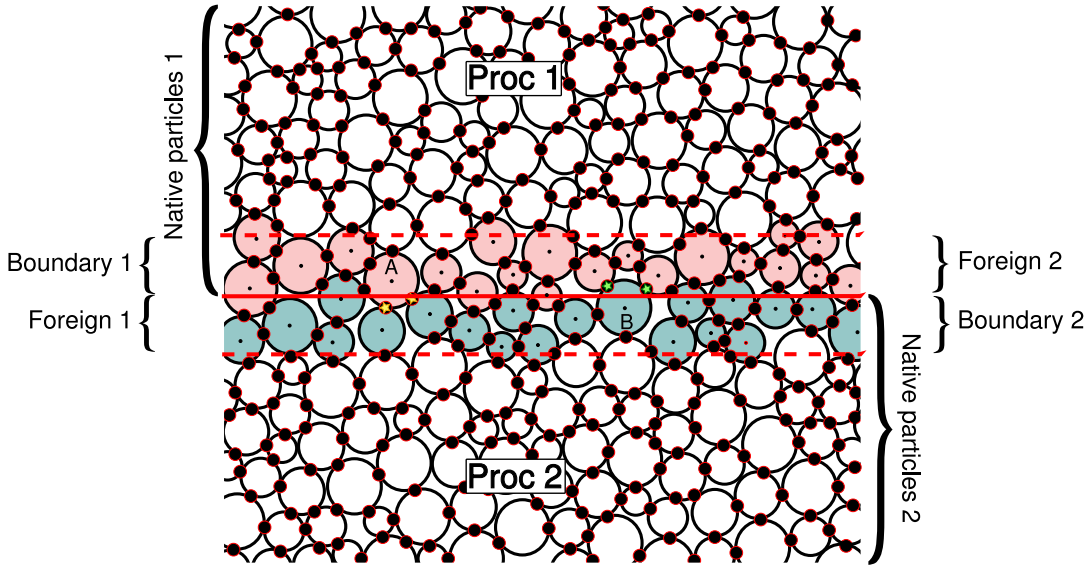

Figure 9.3: Schematic picture showing two neighboring processors at their common interface. Their respective domain and boundary regions are marked. Particle A is a *native* particle of processor 1 and is in contact (asterisks) with two *foreign* particles, namely *boundary* particles of processor 2. The contacts are *boundary* contacts of processor 2 and thus *foreign* ones to processor 1. Particle B is a *boundary* particle of processor 2 and has two contacts (asterisks) located inside the domain of processor 1, i.e. they belong to the latter's *boundary* contacts.

particle displacement to be $0.1r_{\max}$ and thus use the boundary size

$$\ell = 2.2r_{\max}\,. \tag{9.4}$$

Hence, a small amount of in principle irrelevant neighboring information is transferred. This is dominated by other effects, though, as will be shown in Sec. 9.4.2.

After the identification of the *boundary* particles, their relevant data is sent to the corresponding neighbor processors, which keep the information of these (to them) *foreign* particles. Since sender and receiver will always agree about the forces acting on these particles, the receiver can evolve their state on its own.

The next step is to identify actual and possible contacts between both *native* and *foreign* particles. A position is assigned to each contact, which is the middle of the gap (see Fig. 4.2). Obviously, for particles in touch, this is the contact point. Each processor builds a list of *native* contacts for the iteration loop exclusively from contacts lying in its domain. The remaining ones are called *foreign* contacts and are in turn *boundary* contacts of neighboring processors. During an iteration sweep, they

will not be updated but their forces enter the force calculation algorithm. Only at the end of the sweep, each processor sends the new forces of its *boundary* contacts to its corresponding neighbor. This means that during an iteration sweep, foreign contacts always have the values from the last iteration, while native contacts are gradually updated realizing a mixture of parallel and sequential update.

The convergence of the force calculation has to be checked after each iteration sweep. This should be a global test, since the convergence in different subdomains may be achieved at different iteration steps. This task can only be completed by a single processor. Therefore, the necessary data is collected and submitted to the root processor, which makes a decision whether the iteration should continue or the convergence is good enough and time stepping can take place. If further iterations are necessary, then only boundary *contact* information is exchanged among neighbors, as particles do not move within the iteration loop. With new foreign contact values, each processor can perform the next iteration sweep. If the iteration loop has finished, the particles are displaced according to the implicit Euler scheme of Eqs. (4.1) and (4.2). Every processor is responsible for its own native particles (but evolves its copies of foreign particles as well).

Before starting the next time step, we have to take care of the load balancing: Every processor broadcasts its own elapsed CPU time, which provides the required information to run the load balancing function. The detailed description of this function is presented in Sec. 9.4.3. If the load balancing function redivides the simulation box, then each processor has to compare its own particle positions to the new domain coordinates of all other processors to determine to which processor each particle has to be sent. This re-association of particles takes place also without domain redivision as particles change domains simply due to their dynamics.

Figure 9.4 summarizes the parallel algorithm. The main differences (highlighted in the diagram) are that (i) at certain points data must be sent or received to neighboring domains; (ii) the iteration scheme updates only native contacts gradually, while foreign contacts are refreshed only after a complete iteration sweep; (iii) load balancing and domain redivision checks take place at the end of the time step.

A mixture of the sequential and the parallel update scheme occurs for a fraction of the contacts. This fraction depends on the surface-to-volume ratio of the subdomain. As discussed in Sec. 9.3.2, a mixed update can become unstable if the contribution of the parallel update exceeds a threshold of order unity. This limitation coincides with the standard limitation of parallel computation that the boundary region should be negligible compared to the bulk. In this sense, for reasonably large systems, no

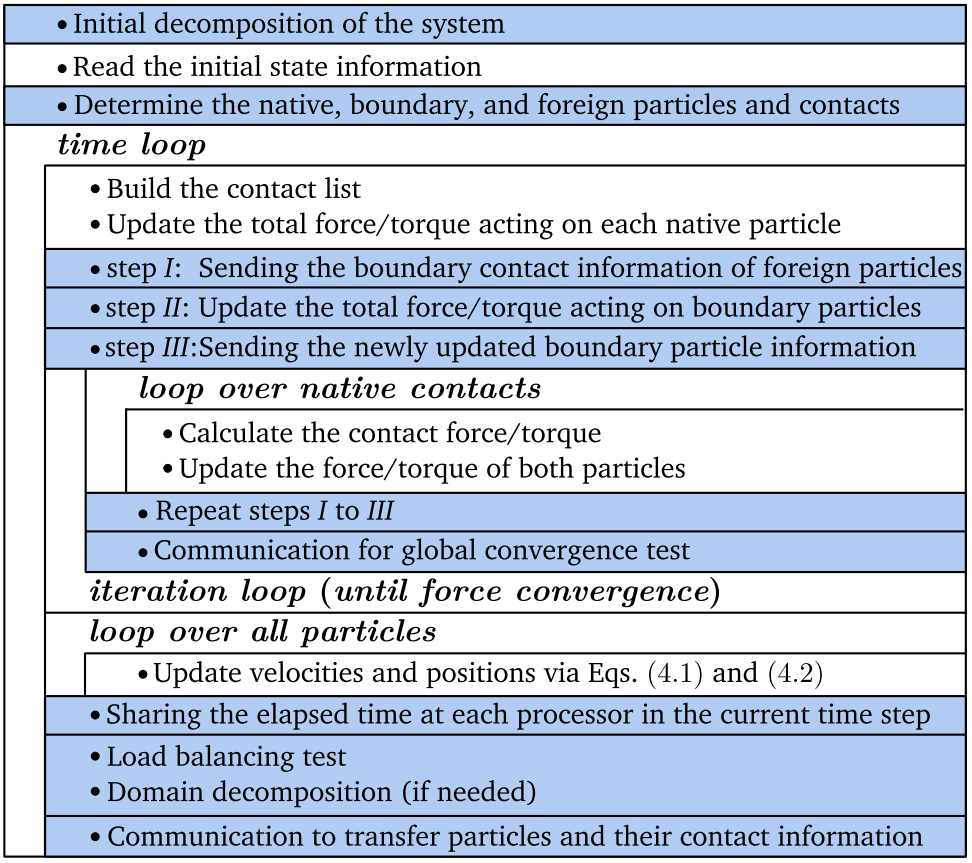

Figure 9.4: The diagram of the parallel version of CD. The colored regions correspond to the new parts compared to the original CD algorithm shown in Fig. 4.4.

instability impact due to the parallel update is expected. Nevertheless, this issue is investigated in Sec. 9.5.3.

In the next section, I introduce a hierarchical domain decomposition method, which finds the best way to arrange the orientation and location of the interfaces so that the surface-to-volume ratio is minimal for a given number of processors.

9.4.2 Hierarchical Domain Decomposition

There is a large variety of domain decomposition methods proposed for parallel particle simulations in the literature, from *Voronoi tessellation* [234] to *orthogonal recursive bisection* (ORB) [235, 236]. For the parallelization of CD the size of the interfaces between domains is more crucial than for MD, since besides communication overhead it also influences the parallel/sequential nature of the global iteration. So the ORB methods are the most suited for the CD code together with adaptive load balancing approaches [237], which is not only important in heterogeneous

clusters but also in the case of changing simulation setup and local particle/contact density.

Before describing the domain decomposition, the contact detection has to be investigated. This process, for which the brute force algorithm scales as $\mathcal{O}(N^2)$ with the number of particles, can be realized for different levels of polydispersity [238–240] within $\mathcal{O}(N)$ CPU cycles. In our CD code the most widespread one has already been implemented, the cell method [238], which works well for moderate polydispersity and which is the most suitable for parallel implementation.

The cell method puts a rectangular grid of mesh size $a_x \times a_y$ on the simulation space. Each particle is assigned to its cell according to its position, and the mesh size is chosen such that the particles can only have a contact with particles from neighboring cells and their own. That means, the cell diameter has essentially the same meaning as the width of the boundary region ℓ and thus they should coincide. On the other hand, the values a_x and a_y have to be chosen such that in each direction every domain has an integer number of cells. But this would mean, in general, a different mesh size for all subdomains, which may be far from the optimal value. Therefore, it is advantageous (for large systems and moderate polydispersities) to choose a global a_x and a_y instead, and restrict the domain boundaries to this grid.

The domain decomposition method proposed in this paper is based on the *orthogonal recursive bisection* algorithm [235] with axis-aligned domain boundaries. The basis of the algorithm is the hierarchical subdivision of the system. Each division represents recursive halving of domains into two subsequent domains. The advantage of such a division is an easy implementation of load balancing, which can be realized at any level, simply by shifting one boundary.

First, we have to group the N_p processors (where N_p is not required to be a power of two) hierarchically into pairs. The division algorithm used is the following: We start at level 0 with one *node*[1], which initially is a *leaf* (a node with no children) as well. A new level l is created by branching each node of level $l-1$ in succession into two nodes of level l, creating 2^l leaves. This continues until $2^l < N_p \leq 2^{l+1}$. Then, only $N_p - 2^l$ leaves from level l are branched from left to right, cf. Fig. 9.5(a).

Next, a domain has to be assigned to each leaf/processor. In the beginning, having no information about the system, all domains should have the same size. Actually, their sizes equal only approximatively due to grid restriction described above, cf. Fig. 9.6(a). To achieve this, the recursive division of the sample is done according

[1] These are abstract nodes in a tree rather than (compounds of) CPUs.

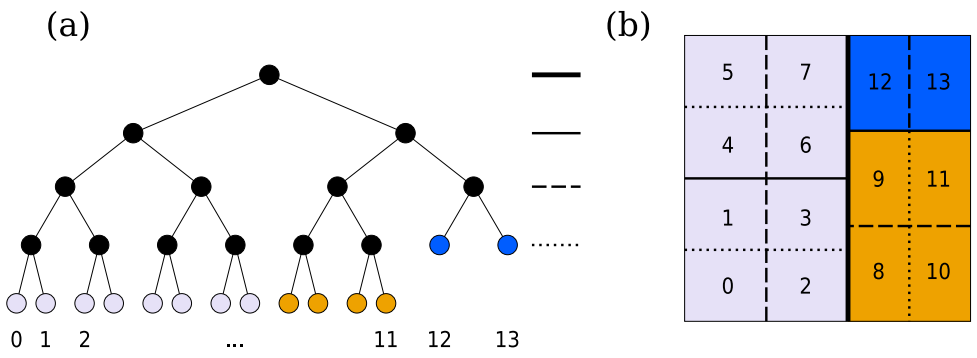

Figure 9.5: An initial hierarchical decomposition of the simulation domain for $N_p = 14$.

to the tree just described. Each non-leaf node represents a bisection with areas corresponding to the number of leaves of its branches (subtrees). The direction of the cut is always chosen as to minimize the boundary length.

The hierarchical decomposition method provides the possibility of quick searches through the binary tree structure. For example, the task to find the corresponding subdomain of each particle after load balancing requires a search of order $\mathcal{O}(\log(N_p))$ for N_p processors. With respect to bookkeeping overhead, a further advantage of this decomposition scheme is that local load imbalance does not necessarily affect higher level subdomain boundaries. For example, if particle exchange takes place across a low level domain boundary only this boundary will move leaving the others untouched.

9.4.3 Adaptive Load Balancing

For homogeneous quasi-static systems, the initially equal-sized subdomains provide already a reasonably uniform load distribution, but for any other case the domain boundaries should dynamically move during the simulation. In the load balancing function, I take advantage of the possibility provided by MPI to measure the wall clock time accurately. For every time step, the processors measure the computational time spent on calculations and broadcast it, so that all processors can decide simultaneously whether or not the load balancing procedure has to be executed. To quantify the global load imbalance, the relative standard deviation of the elapsed CPU time in this time step [2] is calculated via the dimensionless quantity

$$\sigma_T \equiv \frac{1}{\langle T \rangle} \sqrt{\langle T^2 \rangle - \langle T \rangle^2}, \tag{9.5}$$

[2]Assuming exclusive access to the computing resources on every processor, I identify wall clock time and CPU time throughout this chapter.

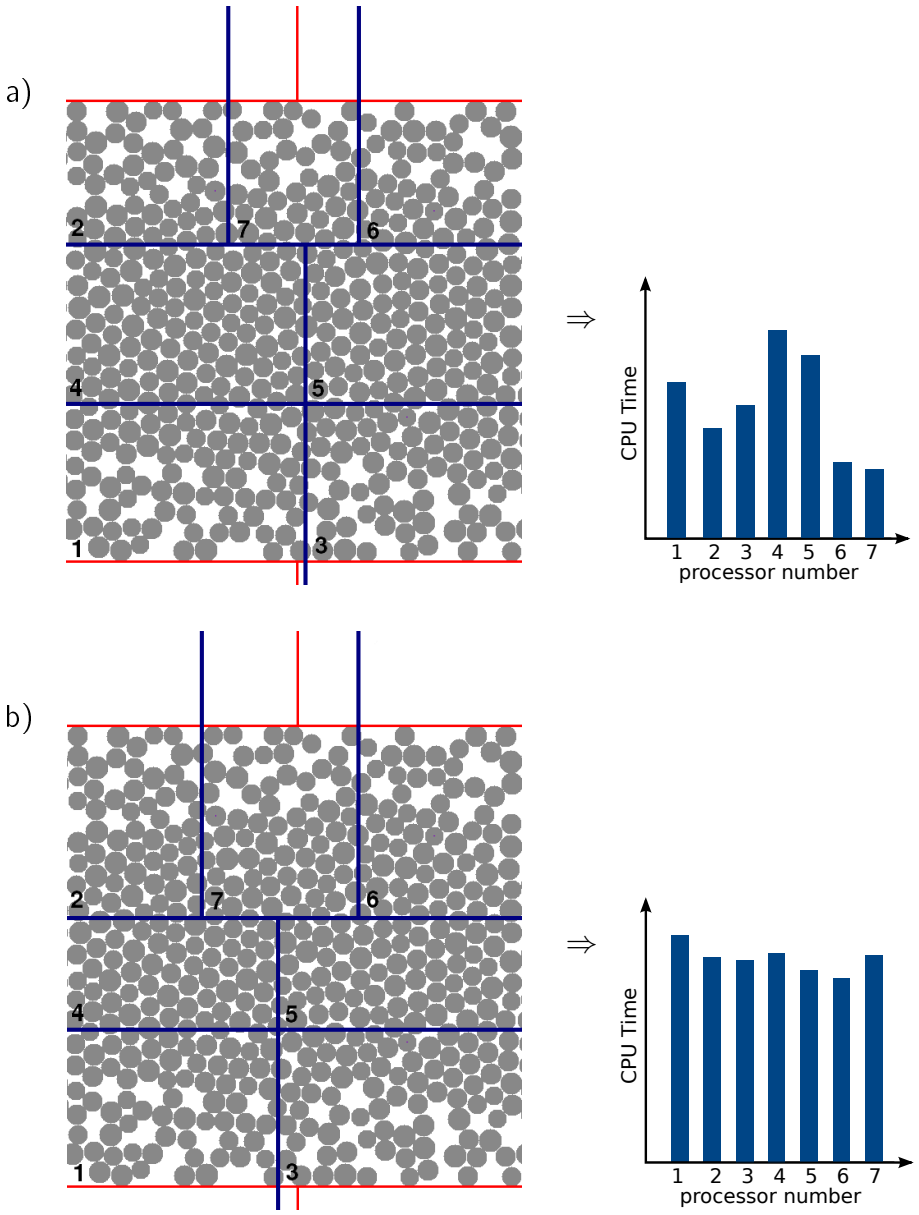

Figure 9.6: (a) Geometrical domain decomposition at the beginning of the simulation leads to an unbalanced distribution of the load over the processors. (b) After load balancing, the volume of the subdomains belonging to different processors vary according to the CPU time it needed in the previous time step and the load distribution over the processors becomes more even.

where the average is taken over the processors.

A threshold value σ_T^* is defined to control the function of the load balancing algorithm: If $\sigma_T < \sigma_T^*$, then the simulation is continued with the same domain configuration, otherwise load balancing must take place. This load balancing test is performed by all processors simultaneously, since all of them have the necessary data. The result being the same on all processors, no more communication is needed.

If the above test indicates load imbalance, we have to move the domain boundaries. This may happen at any non-leaf node of the domain hierarchy tree. The relevant parameter for the domain division is the *calculating capacity* of the branches, which is defined as

$$\nu_j = \sum_i \frac{V_i}{T_i}, \tag{9.6}$$

where T_i and V_i are the CPU time and volume of domain i, respectively, and the summation includes all *leaves* under branch j. Let us denote the two branches of a node as j and k, then the domain must be bisectioned according to

$$\tilde{\nu}_j \equiv \frac{\nu_j}{\nu_j + \nu_k} \quad \text{and} \quad \tilde{\nu}_k \equiv 1 - \tilde{\nu}_j \quad . \tag{9.7}$$

The above procedure is repeated for all parent nodes. If the size of a domain was changed, then all subdomain walls must be recalculated as even with perfect local load balance the orientation of the domain boundary may be subject to change. Note that boundaries must be aligned to the grid boundaries as explained in Sec. 9.4.2.

As an example, let us consider the situation of Fig. 9.5 at the node of level 0 with branch 1 to the left and branch 2 to the right. If all T_i would be the same, then $\tilde{\nu}_1 = 8/14$ and $\tilde{\nu}_2 = 6/14$, just as the initial configuration. Let us now assume that the processors 12 and 13 (top right in Fig. 9.5(b)) are only half as fast as the others, thus, the elapsed time is twice as much. In this case $\tilde{\nu}_1 = 8/13$ and $\tilde{\nu}_2 = 5/13$, so the thick, solid division line moves to the right. Furthermore, the thin, solid division line on the right moves up from the position 4/6 to 4/5.

Figure 9.6 shows how load balancing improves the CPU time distribution over seven processors. The initial geometrical decomposition leads to an uneven workload distribution because of the inhomogeneous density of the original particle configuration (Fig. 9.6(a)). However, the load balancing function manages to approximately equalize the CPU times in the next time step by moving the borders (Fig. 9.6(b)).

9.5 Numerical Results

In the following, I present the results of test simulations for different systems performed by the parallel code. The main question to answer is how efficient is the parallel code, i.e. how much could we speed up the calculations by means of parallelization. The sensitivity of the performance to the load balancing threshold is also studied. The partially parallel updates at the domain boundaries is the main conse-

quence of parallelization, which may make a difference in the results compared to the sequential implementation. Therefore, I investigate the impact of parallelization on the number of iterations and on the physical properties of the solutions.

9.5.1 Performance of the Force Calculation

In this section, I test the efficiency of the parallel algorithm solely with respect to the force calculation. In general, it is the most time consuming part of the contact dynamics simulation (see Sec. 9.3.1), so the efficient parallelization of the iteration scheme is necessary for the overall performance.

To focus just on the force calculation, I chose test systems where large scale inhomogeneities are absent and adaptive load balancing is unnecessary. Thus, dense static packings of 500, 8000, and 10^6 particles (with L_x=20, 20, 100 and L_y=20, 320, 10000, respectively) with periodic boundary conditions in one direction and confining walls in the other were set up (see Fig. 5.1). The calculations started with no information about the contact forces and the simulation was stopped when the local convergence criterion is fulfilled (see Sec. 4.2.4). Of course, this requires a different number of iterations depending on the system size and number of processors. In order to get rid of perturbing factors like input/output performance, solely the CPU time spent in the iteration loop is measured. Figure 9.7 summarizes the test results, which show that if the system is large compared to the boundary regions, the efficiency is about 100%, which is equivalent to a *linear* speedup. The smallest system is inapt for parallelization, as already for only 4 processors the boundary regions take up 20% of the particles, which induces a large communication overhead. The same fraction of boundary particles is reached around N_p=32 for the medium sized system with 8000 particles. Therefore, one would expect the same performance for N_p=4 and 32 for the small and medium sizes, respectively. In addition to the above mentioned effect, the efficiency of the medium system breaks down at N_p=24 due to special architecture of the distributed memory cluster used for simulations (Cray-XT6m with 24 cores per board), since the speed of the inter-board communications is much slower than the intra-board one. The observed efficiency values over 100% are possible through caching, which was already observed in molecular dynamics [227]. The largest system has a large computation task compared to the boundary communication, which is manifested in almost 100% efficiency. On the other hand, it is also too large for significant caching effects producing over 100% efficiency. However, a gradual increase in the efficiency is observed as the domain size (per processor) decreases with increasing the number of processors.

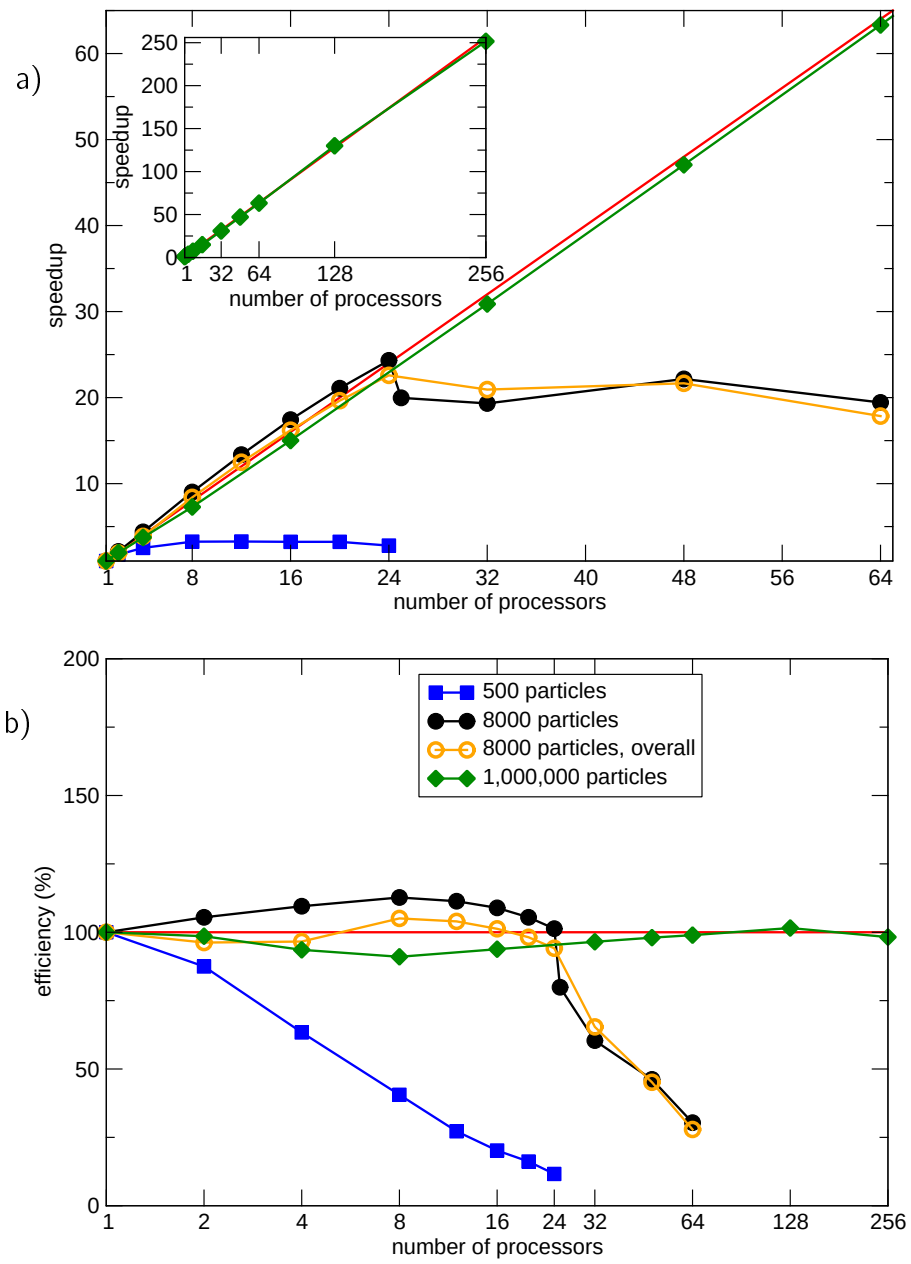

Figure 9.7: (a) Speedup and (b) efficiency of the force calculations for a small system with 500 particles (full squares), a medium system with 8000 particles (full circles), and a large system with 10^6 particles (full diamonds). The open circles present the overall efficiency for the medium sized system.

For the medium sized system, I also measured the overall performance including time stepping and load balancing. For this purpose, the top wall was removed and the bottom wall was pushed upwards in order to generate internal dynamical processes, which unbalances the load distribution. As shown in Fig. 9.7, there is no significant difference in efficiency due to the fact that time stepping and contact detection are perfectly parallelizable processes.

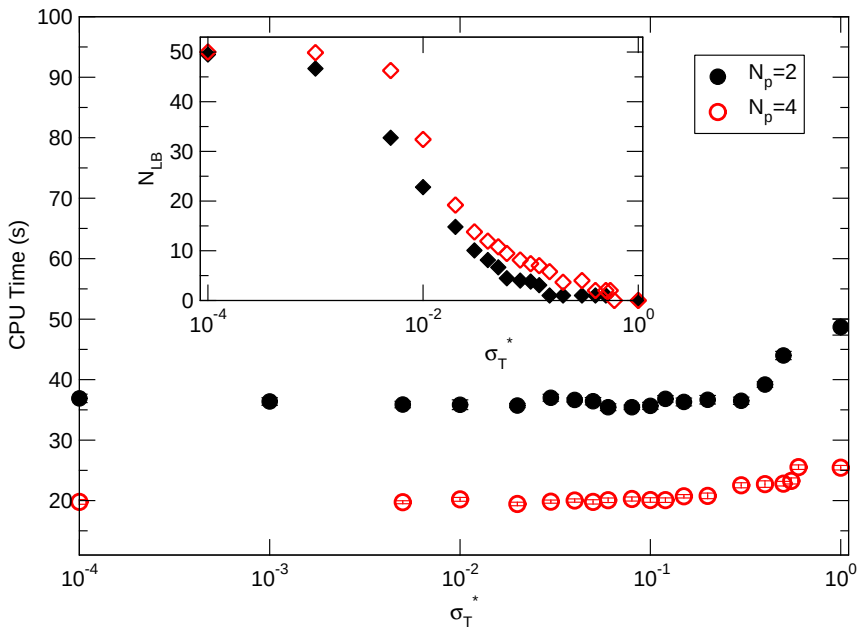

Figure 9.8: CPU time as a function of the load balancing threshold σ_T^*. The simulation runs over 50 time steps with 2 or 4 processors. The inset shows the number of load balancing events versus σ_T^*.

9.5.2 Load Balancing Threshold

In Sec. 9.4.3, the load balancing threshold σ_T^* was defined for the relative standard deviation of the elapsed CPU time on different processors, above which load balancing takes place. While the load balancing test is performed at each time step, the frequency of load redistribution is determined by the choice of σ_T^*. On the one hand, if the subdomain redivision happens frequently, a waste of CPU time is avoided because of even load distribution. On the other hand, the change of domain boundaries requires extra communication and administration. Doing this too often leads to unwanted overhead.

For load balancing, contact dynamics has the advantage, compared to other DEM methods, that the configuration changes rather infrequently (with respect to CPU time), because the force calculation with typically 50−200 iteration sweeps (for reasonably accurate precision of contact forces) dominates the computation. Thus, even taking the minimal value of σ_T^*=0 does not lead to measurable overhead. Moreover, in my implementation the domain boundaries must be on the cell grid, which avoids unnecessary small displacements of the domain walls. Hence, the optimal value of σ_T^* is the minimal one as shown in Fig. 9.8.

9.5.3 Increase of Iteration Number with Number of Processors

In the iteration scheme of contact dynamics, the forces relax towards the solution in a diffusive way [179]. The diffusion constant was found to be

$$D = q\frac{4\,r^2\,N_l}{\Delta t}, \tag{9.8}$$

where Δt is the time step, r is the diameter of a particle, and q is a constant depending on the update method: q_p=0.5 for parallel and $q_s \simeq 0.797$ for random sequential update. Thus the diffusion coefficient of the parallel update, D_p, is smaller than that of the sequential update D_s, for a given set of parameters N_l, Δt, and r. Boundaries between sub-domains handled by different processors behave like parallel update, since the new information only arrives at the end of an iteration sweep. It is therefore expected that the same system requires more iterations in the multiprocessor version, as the number of iterations is inversely proportional to the diffusion constant.

I test this conjecture on two examples: Let us first consider a linear chain of n touching identical particles placed between two perpendicular plates (cf. Fig. 9.9(a)). I suddenly switch on a compressing force on one side wall, while keeping the other wall fixed. The resulting contact forces are calculated by the iterative solver. In order to estimate the number of required iterations, I define the effective diffusion coefficient as of [241]:

$$\overline{D} = D_p p + D_s(1-p), \tag{9.9}$$

where p is the portion of the chain with a parallel update. In general, for each boundary one particle diameter is handled parallel and the rest sequential, which gives p=N_p/n. This is compared to the numerical results in Fig. 9.9(b). While in principle there is no fit parameter in Eq. (9.9), by adjusting the ratio to D_s/D_p=1.53, I get an almost perfect agreement for all different system sizes, as shown in Fig. 9.9(b). This fitted value is 4% smaller than the theoretical estimation of [179].

I have tested this scenario in a similar two-dimensional setup, where the forces were directly applied to the boundary particles as shown in Fig. 9.9(c). The number of iterations required for the prescribed force accuracy increases with the number of processors in a sub-linear manner (Fig. 9.9(d)). This is expected as the fraction of boundary particles in a two-dimensional system scales as $\sqrt{N_p/n}$. The theoretical estimation used in the above one dimensional example with D_s/D_p=1.53 is in good agreement with the results of the two dimensional system as well. The graph of simulation results is characterized by plateaus (e.g. between N_p=2−4 and 6−8), where the convergence rate is dominated by the higher number of domain walls in

one direction.

Let us conclude here that the slower parallel diffusion part takes place in a portion $p \propto \sqrt{N_p/n}$ of the two dimensional system, which is negligible in reasonably large systems. For example for the medium sized system of 8000 particles, I get $p \simeq 4\%$ for N_p=16, which would lead to about 2% increase in the iteration number. The measured value was about 1% justifying the insignificance of the iteration number increase in large systems. Indeed, no decrease in efficiency could be observed due to an increase of the iteration number for large parallel systems in Fig. 9.7.

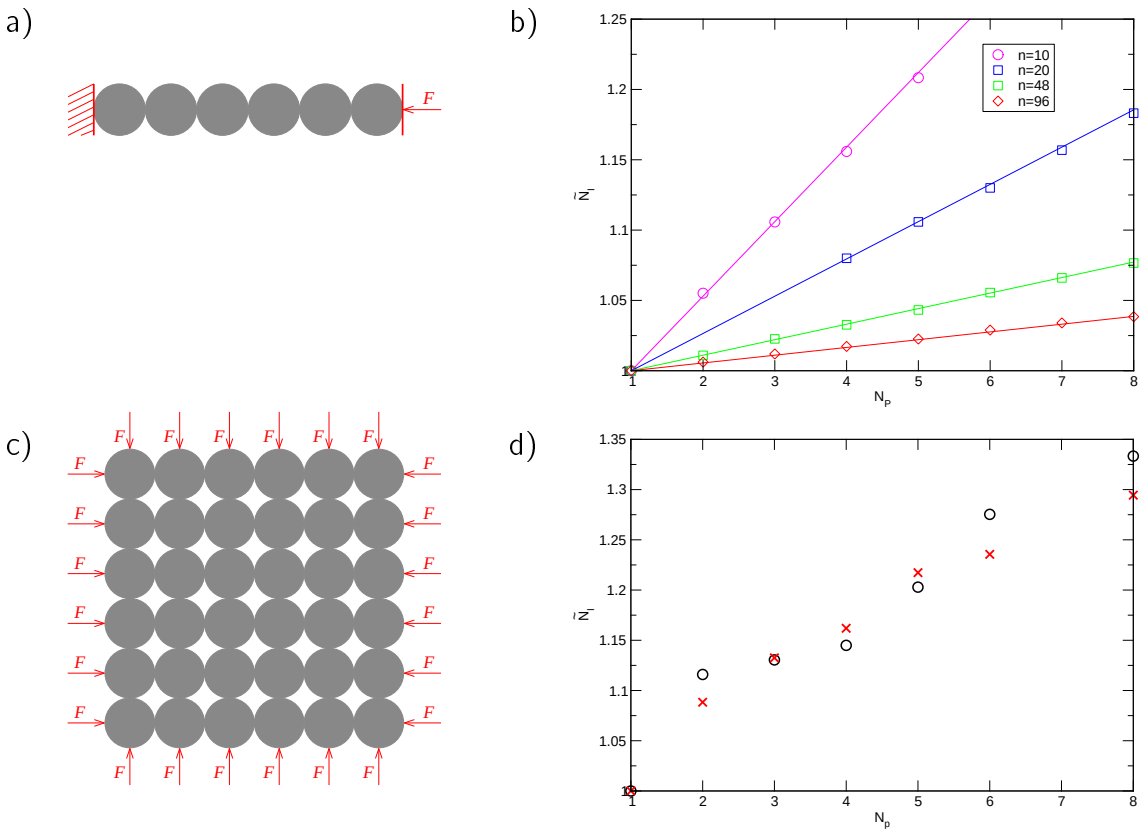

Figure 9.9: (a) A chain of n touching monodisperse particles, which are compressed with a force F. (b) The number of iterations needed to reach a given accuracy scaled by the value for a single processor ($\tilde{N}_I$) vs. the number of processors. The data points are simulation results, and the lines are linear fits (see text). (c) An ordered configuration of monodisperse particles, where the external forces F push the outer particles inwards. (d) $\tilde{N}_I$ vs. N_p, where open circles denote the simulation results and the crosses are the theoretical estimations.

9.5.4 Influence of Parallelization on Physical Properties of Solutions

As a last check, I tested the physical properties of the system calculated by different number of processors. It is known that in the rigid limit, the force network of a given geometrical packing is not unique [242, 243]. Running the contact dynamics with different random seeds (for the random sequential update) leads to different sets of contact forces, which all ensure the dynamical equilibrium. The domain decomposition also changes the update order and the solutions will be microscopically different. Thus, a direct comparison is impossible and I have to resort to comparing distributions. I first investigate the distribution of the contact force orientations $f(\phi)$ in the relaxed system of 8000 particles described in Sec. 9.5.1. The contact forces are calculated from scratch for the given geometry and boundary conditions using different number of processors. Since the system is very tall (L_y/L_x=16), it is divided only vertically for up to N_p=16, while for N_p=32 the 16 domains are cut horizontally as well. The orientation of each contact force is defined as $\phi = \arctan(R_y/R_x)$. The distributions of the contact force orientations, $f_{N_p}(\phi)$, are compared for several values of N_p in Fig. 9.10(a). The range of possible values for ϕ ($[0, \pi]$) is divided into 18 bins, and each data point in the figure corresponds to the total number of contacts in the same bin. For comparison, I have presented the results of the simulations with N_p=1 for two different random seeds as well. The match among the different runs are so good that the curves coincide. Hence, I also plot the relative difference $f_{N_p}(\phi)/f_1(\phi)-1$ to the non-parallel run for comparison, which shows negligible random noise. Evidently, parallelization has no systematic impact on the angular distribution of the contact forces. Similar results were obtained when the system is sheared by the horizontal confining walls moving with a constant velocity in opposite directions as shown in Fig. 9.10(b).

I also calculate the σ_{yy} component of the stress tensor as a function of the distance y from the bottom wall in the same system. $\sigma_{yy}(y)$ at a given height y is averaged over a horizontal stripe of width dy=$2r_{\max}$, where $r_{\max}$ is the largest particle radius in the system. The system height is thus divided into nearly 320 stripes. Figure 9.11 displays the results obtained by the non-parallel code as well as the parallel code with N_p=3. In the parallel case, the system is divided horizontally into three parts. The results of the parallel run match perfectly with the one of the non-parallel run. Especially, no kind of discontinuity or anomaly is observed at $y \simeq 107$ and $y \simeq 212$, where the interfaces between the processors are located.

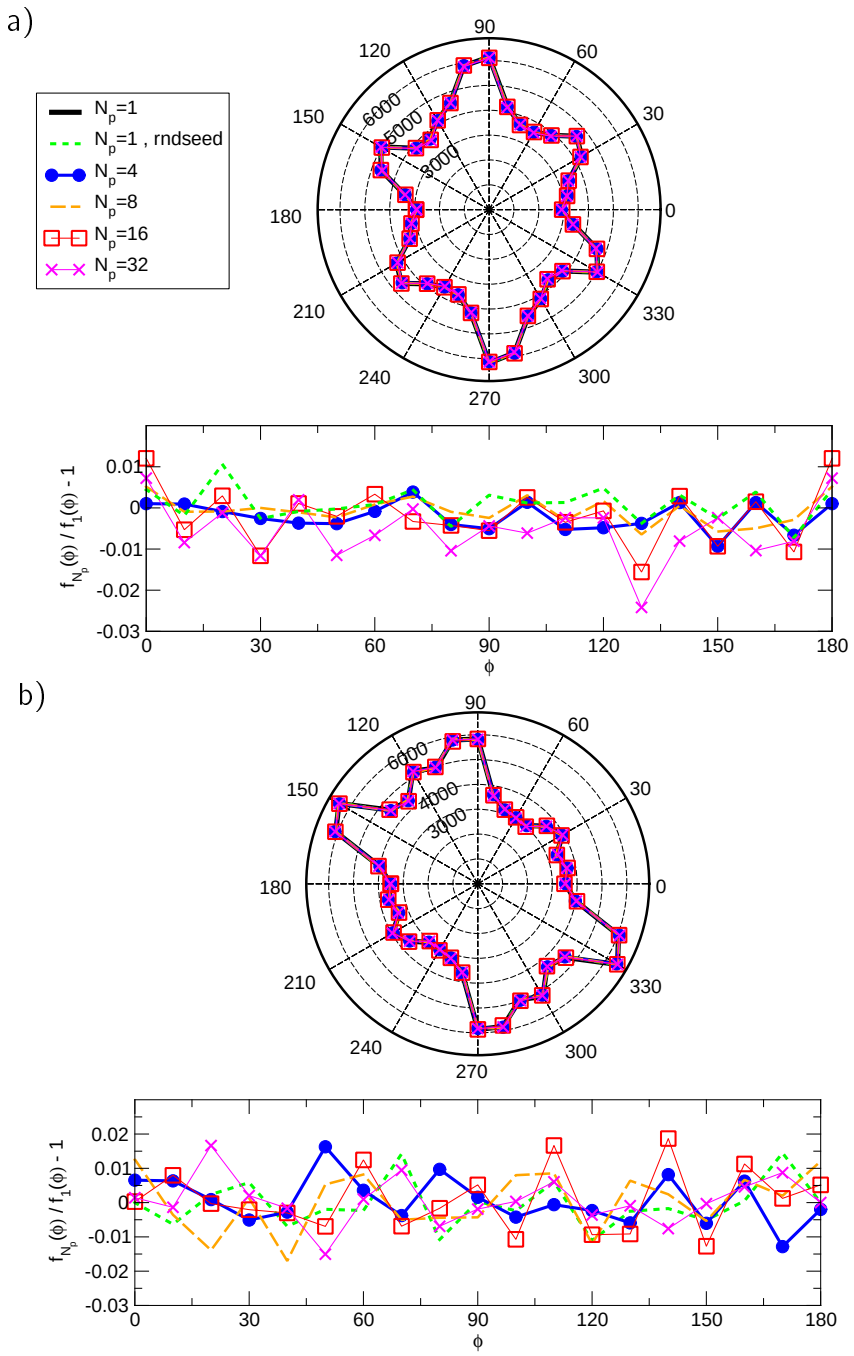

Figure 9.10: Angular distribution of the contact force orientations in (a) the relaxed static packing and (b) the sheared system with moving confining walls, with 8000 frictional particles calculated for different number of processors.

9.6 Conclusion and Discussion

In this chapter, I have presented an efficient parallel version of the contact dynamics method, which allows for large-scale granular simulations with almost 100% efficiency. I aimed at the full parallelization of the code with hierarchical domain decomposition

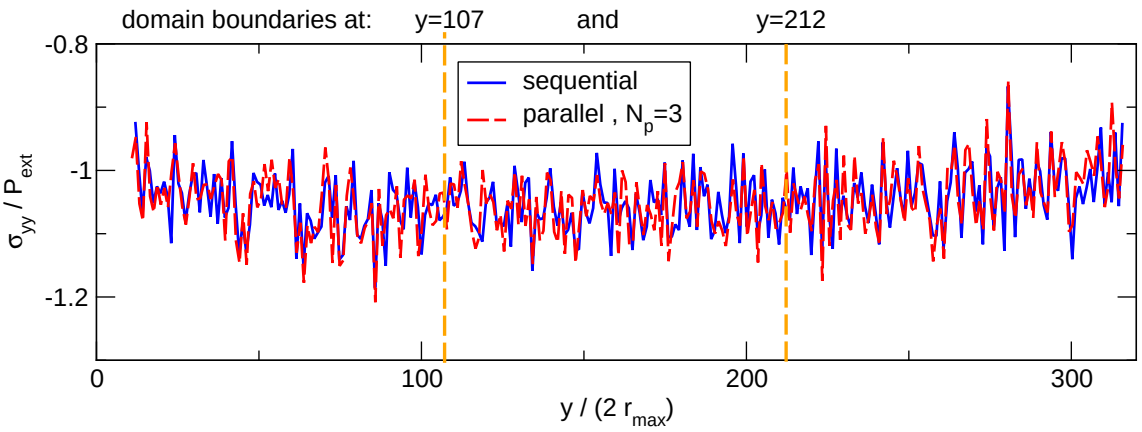

Figure 9.11: $\sigma_{yy}(y)$ scaled by the external pressure P_{ext} in terms of the height y scaled by the diameter of the largest particle in the system ($2\,r_{\text{max}}$). The results obtained by the non-parallel code are compared with those obtained by the parallel code for $N_p = 3$.

and dynamic load balancing, in which the interface area between subdomains is also minimized. The parallel code is hence applicable to a broad range of densities and different simulation conditions.

The force calculation in CD is done by an iterative scheme, which shows an instability if more than about half of the contacts are calculated in parallel. The iteration scheme was kept domain-wise sequential, while data across the domain boundaries is exchanged after each iteration sweep, ensuring that the iteration is stable for all system sizes. It is known that the CD iterative scheme approaches the solution in a diffusive manner. The diffusion constant is smaller for parallel update, which happens at domain boundaries. However, this overhead is proportional to the square root of the number of processors divided by the number of particles (in 2D), which vanishes for large systems. Regarding this as the only impact of the parallelization on the convergence, it must be expected that the efficiency is not affected by modifications at the local level i.e. non-spherical particles, three-dimensional particles, more sophisticated contact laws, etc. Of course, those can deteriorate the convergence per se but the parallel version will simply "inherit" that.

The other point of discussion raised here concerns the choice of the mesh size and adjusting the subdomain borders to it. Communication overhead was reduced because between iteration steps not all boundary information is sent but only the relevant part of it. The subdomain wall position is only important if the particle size is not small compared to the system size. For large scale parallel applications this can only be a problem for highly polydisperse systems, for which the cell method for contact detection breaks down anyway.

The load balancing is done only at the end of each time step. My investigations show that this happens rarely enough that load balancing overhead and CPU time fluctuations are negligible but often enough to achieve fast load balance. I used a global criterion for stopping the iteration scheme. This ensures that the physical properties of the tested samples do not show any difference compared to the non-parallel version of the code.

Blocking point-to-point communications were used to transfer data among processors. Since the algorithm needs synchronization after each iteration, non-blocking data transfer would not be advantageous. The whole amount of data is transmitted in one single packet, which reduces communication overhead over the pure data. This method introduces parallel contact update at domain boundaries, which induces an iteration number overhead due to the lower diffusivity of the information in parallel update. This overhead vanishes, e.g. with the square root of the processor number over particle number in two dimensions, which is in general negligible.

An alternative method would be to use non-blocking communications for the iteration scheme, namely to immediately send a freshly updated contact force in the vicinity of the borders to the corresponding processors, while on the other side this would trigger an interrupt when the other processor immediately updates the received contact data. This prevents the mixture of sequential and parallel update schemes. However, I do not expect that the performance of the method is greatly enhanced by the use of non-blocking communication because the information of each contact force is sent individually and the overhead associated with the increase of the inter-processor communications significantly affects the performance.

The last point to discuss concerns the load balancing method. The most exact method would be to consider the number of particles and/or contacts in each subdomain to calculate their new boundaries. Practically, this would cause difficulties, since each processor is just aware of particles and contacts within its own borders. The amount of calculations and communications between neighboring processors to place the interface according to the current contact and particle positions would make the load balancing a computationally expensive process. This leads us to balance the load further by dividing the simulation domain according to the current subdomain volumes (not always proportional to the number of particles and/or contacts), which is in fact a control loop with the inherent problems of under- and over-damping.

10 Conclusions and Outlook

In this thesis, the shear properties of granular assemblies of non-cohesive, hard, round, dissipative and frictional particles were studied by numerical simulations. A two dimensional planar shear cell with prescribed shear velocity and pressure has been selected as the shear geometry. Although planar shear is known to be the simplest shear geometry, using absolutely smooth but frictional walls, I have shown that strong shear rate inhomogeneities appear in this system, which are induced by slip at the walls. Three different shear regimes have been detected, each belonging to a well defined shear velocity interval. From high to low shear velocities, these three regimes are: (A) a fluid like state with almost homogeneous shearing, (B) a block like state with symmetric velocity profiles and fluidization only at the walls, and (C) a state of broken symmetry, where a block moves essentially with one wall while possessing a shear zone at the other. The properties of all these regimes as well as the transitions between them have been studied in detail in chapter 6. For increasing shear velocity, system size analysis shows a first order transition from regime C to B, at $V_{BC} \simeq 0.10$ and a continuous transition between regimes B and A starting at $V_{AB} \simeq 0.50$. Both V_{BC} and V_{AB} were shown to be essentially independent of the system size. A detailed discussion on these results can be found in Sec. 6.5 on page 82.

In chapter 7, the shear localization at smooth frictional walls has been investigated by deducing constitutive laws in the bulk and boundary regions, separately. The new approach of deducing constitutive laws for the boundary layer in this work helps to characterize the specific behavior in this region, despite the existence of strong inhomogeneity and slip. The boundary region is restricted by default to a layer of width 10 at the walls, and the rest of the system is considered as the bulk region. In the bulk, the constitutive laws agree with those in the literature. By means of separate constitutive laws in the bulk and boundary regions, supplemented by an elementary stability analysis, the occurrence of both transitions at V_{BC} and V_{AB}, as well as characteristic transient times have been predicted.

Additional numerical work could be fruitfully carried out in order to assess the dependence of the boundary layer constitutive law on the state of the adjacent bulk

material with full generality. The application of similar constitutive laws for smooth boundaries should be attempted in a variety of flow configurations: inclined planes, vertical chutes and circular cells. Finally, the success of the simple type of stability analysis carried out in this chapter calls for more accurate, full-fledged approaches, in which couplings of shear stress and deformation with the density field would be taken into account.

In chapter 8, the special features of shearing with absolutely smooth frictional walls are presented. With increasing Coulomb friction μ_W at the walls, the slip velocity decreases and disappears in the limit of $\mu_W \to \infty$. Below a critical friction coefficient $\mu_W^\star$, the walls are not able to shear the system and the whole filling moves as a block with very small velocities compared to the shear velocity. Hence, μ_{eff} increases linearly with μ_P and μ_W in this interval. Beyond this critical value, saturation can be observed after a short transient. The I-dependency of μ_{eff} leads to a sharp drop of μ_{eff} at $\mu_W^\star$ in the slow shear regime. As the velocity profiles reveal, this effect is a consequence of block formation for $\mu_W < \mu_W^\star$ and the reduced μ_{eff} for $\mu_W > \mu_W^\star$ in the quasistatic regime.

With increasing rolling friction μ_{rW} at smooth walls, the frustration of the rotation of the particles in contact with the walls increases and consequently μ_{eff} grows, leading to more and more homogeneous shearing in the bulk of the system. Hence, I propose to activate rolling friction at smooth walls to avoid slip, instead of using rough walls. In this way, the system configuration and preparation becomes more straightforward. In chapter 8, it was also shown that in the quasistatic shear regime the general tendency for μ_{eff} as a function of μ_W in the limit of small roughness sizes is similar to that of absolutely smooth walls and deviates with increasing roughness size. My results in Fig. 8.16 contradict the general assumption, which takes $\mu_W^\star = \mu_P$ [34]. A more detailed discussion on these results is presented in Sec. 8.3 on page 119.

In chapter 9, an efficient parallel version of the contact dynamics method is presented, which allows for large-scale granular simulations with almost 100% efficiency. The code is fully parallelized with hierarchical domain decomposition and dynamic load balancing, in which the interface area between subdomains is also minimized. The parallel code is hence applicable to a broad range of densities and different simulation conditions. Since a global criterion has been used for stopping the iteration scheme, the physical properties of the tested samples do not show any difference compared to the non-parallel version of the code. A more detailed discussion on points like the choice of the mesh size, blocking and non-blocking communications and the load balancing methods, is presented in Sec. 9.6 on page 145.

Bibliography

[1] E. Aharonov and D. Sparks. Shear profiles and localization in simulations of granular materials. *Physical Review E*, 65:051302, 2002.

[2] P. G. de Gennes. Granular matter: a tentative view. *Rev. Mod. Phys.*, 71(2):374–382, 1999.

[3] C. F. Higgs and J. Tichy. Effect of particle and surface properties on granular lubrication flow. In *Proceedings of the I MECH E Part J Journal of Engineering Tribology*, volume 222, pages 703–713, 2008.

[4] G. Gutiérrez, P. Boltenhagen, J. Lanuza, and E. Clément. Silo collapse: An experimental study. In C. Appert-Rolland, F. Chevoir, P. Gondret, S. Lassarre, J.-P. Lebacque, and M. Schreckenberg, editors, *Traffic and Granular Flow*, pages 517–523, Berlin, 2009. Springer.

[5] J. C. Williams. The segregation of particulate materials. a review. *Powder Technology*, 15:245–251, 1976.

[6] G. G. Batrouni, S. Dippel, and L. Samson. Stochastic model for the motion of a particle on an inclined rough plane and the onset of viscous friction. *Physical Review E*, 53(6):6496, 1996.

[7] C. Marone. Laboratory-derived friction laws and their application to seismic faulting. *Annu. Rev. Earth Planet. Sci.*, 26:643–96, 1998.

[8] M. Griffa, E. G. Daub, R. A. Guyer, P. A. Johnson, C. Marone, and J. Carmeliet. Vibration-induced slip in sheared granular layers and the micromechanics of dynamic earthquake triggering. *Europhys. Lett.*, 96(1):14001, 2011.

[9] L. Staron and F. Radjai. Friction versus texture at the approach of a granular avalanche. *Phys. Rev. E*, 72(4):041308, 2005.

[10] L. Staron, J.-P. Vilotte, and F. Radjai. Preavalanche instabilities in a granular pile. *Physical Review Letters*, 89(20):204302, 2002.

[11] M. Faraday. On a peculiar class of acoustical figures; and on certain forms assumed by groups of particles upon vibrating elastic surfaces. *Philosophical Transactions R. Soc. London*, 121:299–340, 1831.

[12] O. Reynolds. On the dilatancy of media composed of rigid particles in contact, with experimental illustrations. *Phil. Mag. Series 5*, 20(127):469–481, 1885.

[13] O. Reynolds. Experiments showing dilatancy, a property of granular material, possibly connected with gravitation. *Proc. Royal Institution of Great Britain*, 11:354–363, 1886.

[14] E. R. Bagnold. *Physics of Blown Sand and Sand Dunes*. Chapman & Hall, London, 1941.

[15] J. T. Jenkins and M. W. Richman. Kinetic theory for plane flows of a dense gas of identical, rough, inelastic, circular disks. *Physics of Fluids*, 28(12):3485, 1985.

[16] M. W. Richman. Boundary conditions based upon a modified Maxwellian velocity distribution for flows of identical, smooth, nearly elastic spheres. *Acta Mechanica*, 75(1-4):227–240, 1988.

[17] J. T. Jenkins. Boundary conditions for rapid granular flows: Flat, frictional walls. *J. Appl. Mech.*, 59:120, 1992.

[18] C. S. Campbell. Boundary interactions for two-dimensional granular flows. part 1. flat boundaries, asymmetric stresses and couple stresses. *Journal of Fluid Mechanics*, 247:111–136, 1993.

[19] C. S. Campbell. Boundary interactions for two-dimensional granular flows. part 2. roughened boundaries. *Journal of Fluid Mechanics*, 247:137–156, 1993.

[20] M. Y. Louge. computer simulations of rapid granular flows of spheres interacting with a flat, frictional boundary. *Physics of Fluids*, 6(7):2253–2269, 1994.

[21] X. M. Zheng and J. M. Hill. Molecular dynamics simulation of granular flows: Slip along rough inclined planes. *Computational Mechanics*, 22(2):160–166, 1998.

[22] H. M. Jaeger, S. R. Nagel, and R. P. Behringer. Granular solids, liquids, and gases. *Reviews of Modern Physics*, 68(4):1259, 1996.

[23] P. Jalali, W. Polashenski Jr., T. Tynjälä, and P. Zamankhan. Particle interactions in a dense monosized granular flow. *Physica D*, 162:188–207, 2002.

[24] A. V. Potapov, M. L. Hunt, and C. S. Campbell. Liquid-solid flows using smoothed particle hydrodynamics and the discrete element method. *Powder Technology*, 116(2-3):204–213, 2001.

[25] M. Babic, H. H. Shen, and H. T. Shen. The stress tensor in granular shear flows of uniform, deformable disks at high solids concentrations. *Journal of Fluid Mechanics*, 219:81–118, 1990.

[26] J. B. Knight, C. G. Fandrich, C. N. Lau, H. M. Jaeger, and S. R. Nagel. Density relaxation in a vibrated granular material. *Phys. Rev. E*, 51(5):3957–3963, 1995.

[27] GDR Midi. On dense granular flows. *The European Physical Journal E*, 14(4):341–365, 2004.

[28] H. M. Jaeger, C.-H. Liu, S. R. Nagel, and T. A. Witten. Friction in granular flows. *Europhysics Letters*, 11(7):619–624, 1990.

[29] F. da Cruz, S. Emam, M. Prochnow, J.-N. Roux, and F. Chevoir. Rheophysics of dense granular materials: Discrete simulation of plane shear flows. *Physical Review E*, 72:021309, 2005.

[30] P. Jop, Y. Forterre, and O. Pouliquen. A constitutive law for dense granular flows. *Nature*, 441:727, 2006.

[31] P. G. Rognon, J.-N. Roux, M. Naaïm, and F. Chevoir. Dense flows of bidisperse assemblies of disks down an inclined plane. *Physics of Fluids*, 19(5):058101, 2007.

[32] S. B. Savage and M. Sayed. Stresses developed by dry cohesionless granular materials sheared in an annular shear cell. *Journal of Fluid Mechanics*, 142:391–430, 1984.

[33] D. M. Hanes and D. L. Inman. Observations of rapidly flowing granular-fluid materials. *Journal of Fluid Mechanics*, 150:357–380, 1985.

[34] G. Koval. *Comportement d'interface des matériaux granulaires*. PhD thesis, École Nationale des Ponts et Chaussées, 2008.

[35] R. Artoni, A. Santomaso, and P. Canu. Effective boundary conditions for dense granular flows. *Physical Review E*, 79(3):031304, 2009.

[36] J. M. Hill and X. M. Zheng. Dilatant double shearing theory applied to granular chute flow. *Acta Mechanica*, 118:97–108, 1996.

[37] M. Kappl, L. Heim, H.-J. Butt, S. Luding, R. Tykhoniuk, and J. Tomas. *From grains to powders: from single particle contact mechanics measurements to bulk powder properties*, chapter 3.1, pages 493–497. Taylor & Francis Group, Stuttgart, Germany, 2005.

[38] K. Wada, H. Senshu, and T. Matsui. Numerical simulation of impact cratering on adhesive granular material. In *36th Annual Lunar and Planetary Science Conference*, page abstract no. 1596, League City, Texas, 2005.

[39] Y. Forterre and O. Pouliquen. Flows of dense granular media. *Annu. Rev. Fluid Mech.*, 40:1–24, 2008.

[40] O. R. Walton and R. L. Braun. Viscosity, granular-temperature, and stress calculations for shearing assemblies of inelastic, frictional disks. *J. Rheol.*, 30:949–980, 1986.

[41] L. Vanel, D. Howell, D. Clark, R. P. Behringer, and E. Clement. Memories in sand: Experimental tests of construction history on stress distributions under sandpiles. *Physical Review E*, 60(5):R5040–R5043, 1999.

[42] J. Török. *Shearing of granular Materials*. PhD thesis, Department of Theoretical Physics, Budapest University of Thechnology & Université de Paris-Sud, 2000.

[43] H. A. Makse. Stratification instability in granular flows. *Physical Review E*, 56(6):7008–7016, 1997.

[44] K. R. LaMarche, M. J. Metzger, B. J. Glasser, and T. Shinbrot. Shape-mediated ordering in granular blends. *Physical Review E*, 81(5):052301–052304, 2010.

[45] K. M. Hill and Y. Fan. Isolating segregation mechanisms in a split-bottom cell. *Physical Review Letters*, 101(8):088001, 2008.

[46] S. Ulrich, M. Schröter, and H. L. Swinney. Influence of friction on granular segregation. *Physical Review E*, 76(4):42301, 2007.

[47] T.-Y. Wang and T. M. Hong. Segregation induced by phase synchronization in a bidisperse granular layer. *Physical Review E*, 78(6):061301, 2008.

[48] L. B. H. May, L. A. Golick, K. C. Phillips, M. Shearer, and K. E. Daniels. Shear-driven size segregation of granular materials: Modeling and experiment. *Physical Review E*, 81(5):051301, 2010.

[49] L. A. Golick and K. E. Daniels. Mixing and segregation rates in sheared granular materials. *Physical Review E*, 80(4):042301–042304, 2009.

[50] Y. Fan and K. M. Hill. Phase transitions in shear-induced segregation of granular materials. *Physical Review Letters*, 106(21):218301–218304, 2011.

[51] J. B. Knight, H. M. Jaeger, and S. R. Nagel. Vibration-induced size separation in granular media: The convection connection. *Physical Review Letters*, 70(24):3728, 1993.

[52] N. Rivas, P. Cordero, D. Risso, and R. Soto. Segregation in quasi-two-dimensional granular systems. *New Journal of Physics*, 13:055018, 2011.

[53] N. Rivas, S. Ponce, B. Gallet, D. Risso, R. Soto, P. Cordero, and N. Mujica. Sudden chain energy transfer events in vibrated granular media. *Phys. Rev. Lett.*, 106(8):088001, 2011.

[54] A. Rosato, K. J. Strandburg, F. Prinz, and R. H. Swendsen. Why the brazil nuts are on top: Size segregation of particulate matter by shaking. *Phys. Rev. Lett.*, 58(10):1038, 1987.

[55] E. Somfai, M. van Hecke, W. G. Ellenbroek, K. Shundyak, and W. van Saarloos. Critical and noncritical jammming of frictional grains. *Physical Review E*, 75(2):020301, 2007.

[56] A. J. Liu and S. R. Nagel. Jamming is not just cool any more. *Nature*, 396:21, 1998.

[57] T. S. Majmudar, M. Sperl, S. Luding, and R. P. Behringer. Jamming transition in granular systems. *Physical Review Letters*, 98(5):058001, 2007.

[58] M. E. Cates, J. P. Wittmer, J.-P. Bouchaud, and P. Claudin. Jamming, force chains, and fragile matter. *Physical Review Letters*, 81(9):1841, 1998.

[59] C. S. O'Hern, S. A. Langer, A. J. Liu, and S. R. Nagel. Force distributions near jamming and glass transitions. *Physical Review Letters*, 86(1):111, 2001.

[60] F. da Cruz. *Friction and jamming in dry granular flows*. PhD thesis, École Nationale des Ponts et Chaussées, 2004.

[61] L. E. Silbert, D. Ertas, G. S. Grest, T. C. Halsey, and D. Levine. Analogies between granular jamming and the liquid-glass transition. *Physical Review E*, 65(5):051307, 2002.

[62] G. Bartels. Die Kontakt-Dynamik Methode: Konvergenzkriterien und eine Anwendung. Diploma thesis, Gerhard Mercator University, Duisburg, Germany, 2001.

[63] J. Duran, E. Kolb, and L. Vanel. Static friction and arch formation in granular materials. *Phys. Rev. E*, 58(1):805–812, 1998.

[64] R. Peralta-Fabi, C. Málaga, and R. Rechtman. Arching in confined dry granular materials. *Europhys. Lett.*, 45(1):76–82, 1999.

[65] S. Ostojic, E. Somfai, and B. Nienhuis. Scale invariance and universality of force networks in static granular matter. *Nature*, 439:828, 2006.

[66] T. S. Majmudar and R. P. Behringer. Contact force measurements and stress-induced anisotropy in granular materials. *Nature*, 435:1079, 2005.

[67] F. Radjai, M. Jean, J. J. Moraeu, and S. Roux. Force distributions in dense two-dimensional granular systems. *Physical Review Letter*, 77(2):274–277, 1996.

[68] C.-H. Liu, S. R. Nagel, D. A. Schecter, S. N. Coppersmith, S. Majumdar, and O. Narayan T. A. Witten. Force fluctuations in bead packs. *Science*, 269:513, 1995.

[69] D. M. Mueth, H. M. Jaeger, and S. R. Nagel. Force distribution in a granular medium. *Physical Review E*, 57(3):3164, 1998.

[70] O. Tsoungui, D. Vallet, and J.-C. Charmet. Experimental study of the force distributions inside 2d granular systems. In Herrmann et al. [244], pages 149–154.

[71] J. Geng, D. Howell, E. Longhi, R. P. Behringer, G. Reydellet, L. Vanel, E. Clément, and S. Luding. Footprints in sand: The response of a granular material to local perturbations. *Physical Review Letters*, 87(3):35506, 2001.

[72] J. Geng, G. Reydellet, E. Clément, and R. P. Behringer. Green's function measurements of force transmission in 2d granular materials. *Physica D*, 182(3-4):274–303, 2003.

[73] B. Miller, C. O'Hern, and R. P. Behringer. Stress fluctuations for continuously sheared granular materials. *Physical Review Letter*, 77(15):3110–3113, 1996.

[74] Bob Behringer's Home Page: www.phy.duke.edu/ bob/.

[75] F. Radjai and S. Roux. Contact Dynamics Study of 2D Granular Media: Critical States and Relevant Internal Variables. In Hinrichsen and Wolf [245], chapter 7, pages 165–187.

[76] G. Koval, J.-N. Roux, A. Corfdir, and F. Chevoir. Annular shear of cohesionless granular materials: From the inertial to quasistatic regime. *Physical Review E*, 79(2):021306, 2009.

[77] J. Blouwolff and S. Fraden. The coordination number of granular cylinders. *Europhys. Lett.*, 76(6):1095–1101, 2006.

[78] J.-N. Roux. Geometric origin of mechanical properties of granular materials. *Physical Review E*, 61(6):6802, 2000.

[79] F. Radjai, D. E. Wolf, M. Jean, and J.-J. Moreau. Bimodal character of stress transmission in granular packings. *Physical Review Letters*, 80(1):61, 1998.

[80] L. E. Silbert, G. S. Grest, and J. W. Landry. Statistics of the contact network in frictional and frictionless granular packings. *Phys. Rev. E*, 66(6):061303, 2002.

[81] C.-H. Liu, S. R. Nagel, D. A. Schecter, S. N. Coppersmith, S. Majumdar, O. Narayan, and T. A. Witten. Force fluctuations in bead packs. *Science*, 269(3):513–515, 1995.

[82] G. Løvoll, K. J. Måløy, and E. G. Flekkøy. Force measurements on static granular materials. *Physical Review E*, 60(5):5872, 1999.

[83] F. Radjai. Multicontact dynamics of granular systems. *Computer Physics Communications*, 121:294, 1999.

[84] F. Radjai, S. Roux, and J. J. Moraeu. Contact forces in a granular packing. *Chaos*, 9(3):544, 1999.

[85] S. Ouaguenouni and J.-N. Roux. Force distribution in frictionless granular packings at rigidity threshold. *Europhys. Lett.*, 39(2):117–122, 1997.

[86] S. J. Antony. Evolution of force distribution in three-dimensional granular media. *Phys. Rev. E*, 63(1):011302, 2000.

[87] J. H. Snoeijer, W. G. Ellenbroek, T. J. H. Vlugt, and M. van Hecke. Sheared force networks: Anisotropies, yielding, and geometry. *Physical Review Letters*, 96(9):098001, 2006.

[88] S. Ostojic, T. J. H. Vlugt, and B. Nienhuis. Universal anisotropy in force networks under shear. *Phys. Rev. E*, 75(3):030301, 2007.

[89] M. R. Shaebani, T. Unger, and J. Kertész. Unjamming due to local perturbations in granular packings with and without gravity. *Phys. Rev. E*, 78(1):011308, 2008.

[90] P. Wang, C. Song, C. Briscoe, K. Wang, and H. A. Makse. From force distribution to average coordination number in frictional granular matter. *Physica A*, 389(19):3972–3977, 2010.

[91] M. R. Shaebani, T. Unger, and J. Kertész. Unjamming of granular packings due to local perturbations: Stability and decay of displacements. *Phys. Rev. E*, 76(3):030301, 2007.

[92] C. Denniston and H. Li. Dynamics and stress in gravity-driven granular flow. *Physical Review E*, 59(3):3289, 1999.

[93] R. Zenit and M. L. Hunt. Solid fraction fluctuations in solid-liquid flows. *International Journal of Multiphase Flow*, 26(5):763–781, 2000.

[94] S. Schöllmann. Simulation of a two-dimensional shear cell. *Physical Review E*, 59(1):889, 1999.

[95] P. Eshuis, D. van der Meer, M. Alam, H. J. van Gerner, K. van der Weele, and D. Lohse. Onset of convection in strongly shaken granular matter. *Phys. Rev. Lett.*, 104(3):038001, 2010.

[96] P. Eshuis, K. van der Weele, D. van der Meer, R. Bos, and D. Lohse. Phase diagram of vertically shaken granular matter. *Phys. Fluids*, 19(12):123301, 2007.

[97] P. Richard, M. Nicodemi, R. Delannay, P. Ribiére, and D. Bideau. Slow relaxation and compaction of granular systems. *Nature Materials*, 4:121–128, 2005.

[98] F. Kohlrausch. *Praktische Physik*, volume 1. Teubner Verlag, Stuttgart, 1968.

[99] M. Bose and V. Kumaran. Velocity distribution for a two dimensional sheared granular flow. *Physical Review E*, 69(6):061301, 2004.

[100] P. A. Cundall. Numerical experiments on localization in frictional materials. *Ingenieur-Archiv*, 59(2):148–159, 1989.

[101] J. Proubet J. P. Bardet. *Numerical Simulation of Localization in Granular Materials*, pages 1269–1273. Columbus, Ohio, 1991.

[102] J. Proubet J. P. Bardet. A numerical investigation of the structure of persistent shear bands in granular media. *Géotechnique*, 41(4):599–913, 1991.

[103] J. J. Moreau. Numerical investigation of shear zones in granular materials. In Wolf and Grassberger [246], pages 233–247.

[104] J. C. Tsai and J. P. Gollub. Granular packings sheared in an annular channel: Flow localization and grain size dependence. *Physical Review E*, 72(5):051304, 2005.

[105] J. K. Morgan and M. S. Boettcher. Numerical simulations of granular shear zones using the distinct element method: I. shear zone kinematics and micromechanics of localization. *J. Geophys. Res. B.*, 104(B2):2703–2719, 1999.

[106] H.-B. Mühlhaus. Scherfugenanalyse bei granularem Material im Rahmen der Cosserat-Theorie. *Ingenieur-Archiv*, 56:389–399, 1986.

[107] I. Vardoulakis and E. C. Aifantis. Gradient dependent dilatancy and its implications in shear banding and liquefaction. *Ingenieur-Archiv*, 59(3):197–208, 1989.

[108] P. Moucheront, F. Bertrand, G. Koval, L. Tocquer, S. Rodts, J.-N. Roux, A. Corfdir, and F. Chevoir. MRI investigation of granular interface rheology using a new cylinder shear apparatus. *Magnetic Resonance Imaging*, 28(6):910–918, 2010.

[109] Y. Zhu and S. Granick. Limits of the hydrodynamic no-slip boundary condition. *Physical Review Letters*, 88(10):106102, 2002.

[110] N. Estrada, A. Taboada, and F. Radjaï. Shear strength and force transmission in granular media with rolling resistance. *Physical Review E*, 78(2):021301, 2008.

[111] D. M. Mueth. Measurements of particle dynamics in slow, dense granular couette flow. *Physical Review E*, 67(1):011304, 2003.

[112] G. Koval, F. Chevoir, J.-N. Roux, J. Sulem, and A. Corfdir. Interface roughness effect on slow cyclic annular shear of granular materials. *Granular Matter*, 13(5):525–540, 2011.

[113] L. E. Silbert, J. W. Landry, and G. S. Grest. Granular flow down a rough inclined plane: transition between thin and thick piles. *Phys. Fluids*, 15(1):1–10, 2003.

[114] T. S. Komatsu, S. Inagaki, N. Nakagawa, and S. Nasuno. Creep motion in a granular pile exhibiting steady surface flow. *Physical Review Letters*, 86(9):1757–1760, 2001.

[115] N. Taberlet, P. Richard, and R. Delannay. The effect of sidewall friction on dense granular flows. *Computers and Mathematics with Applications*, 55(2):230–234, 2008.

[116] C. S. Campbell. Boundary interactions for two-dimensional granular flows: Asymmetric stress and couple stresses. In M. Satake and J. T. Jenkins, editors, *Micromechanics of Granular Materials*, pages 163–173. Elsevier Science Punlishers B. V., Amsterdam, 1988.

[117] M. W. Richman and C. S. Chou. Boundary effects on granular shear flows of smooth disks. *Journal of Applied Mathematics and Physics (ZAMP)*, 39(6):885–901, 1988.

[118] T. Pöschel. Granular material flowing down an inclined chute: A molecular dynamics simulation. *J. Phys. II France*, 3(1):27–40, 1993.

[119] S. Dippel, G. G. Batrouni, and D. E. Wolf. Collision-induced friction in the motion of a single particle on a bumpy inclined line. *Physical Review E*, 54(6):6845, 1996.

[120] S. Dippel, G. G. Batrouni, and D. E. Wolf. How transversal fluctuations affect the friction of a particle on a rough incline. *Physical Review E*, 56(3):3645, 1997.

[121] S. Dippel, G. G. Batrouni, and D. E. Wolf. Motion of a particle on a rough inclined plane: Comparison of 2 and 3 dimensions. In Behringer and Jenkins [247], pages 559–562.

[122] S. Dippel, G. G. Batrouni, and D. E. Wolf. Friction experienced by a particle moving on a rough inclined plane. In Wolf and Grassberger [246], pages 311–315.

[123] C. Goujona, N. Thomas, and B. Dalloz-Dubrujeaud. Monodisperse dry granular flows on inclined planes: Role of roughness. *The European Physical Journal E: Soft Matter and Biological Physics*, 11(2):147–157, 2003.

[124] D. Bideau, I. Ippolito, L. Samson, G. G. Batrouni, S. Dippel, A. Aguirre, A. Calvo, and C. Henrique. Gravity driven motion of a single sphere on a rough inclined surface. In *Proceedings of the HLRZ Workshop on Traffic and Granular Flow*, Singapore, 1996. World Scientific.

[125] L. Samson, I. Ippolito, S. Dippel, and G. G. Batrouni. Diffusive motion of single particles on an inclined bumpy plane. In Behringer and Jenkins [247], pages 503–506.

[126] P. G. Rognon, J.-N. Roux, D. E. Wolf, M. Naaïm, and F. Chevoir. Rheophysics of cohesive granular media. *Europhysics Letters*, 74(4):644–650, 2006.

[127] P. E. Peyneau and J.-N. Roux. Frictionless bead packs have macroscopic friction, but no dilatancy. *Physical Review E*, 78(1):011307, 2008.

[128] A. W. Lees and S. F. Edwards. The computer study of transport processes under extreme conditions. *Journal of Physics C*, 5(15):1921–1928, 1972.

[129] A. Chatterjee. Modification to lees-edwards periodic boundary condition for dissipative particle dynamics simulation with high dissipation rates. *Molecular Simulation*, 33(15):1233–1236, 2007.

[130] F. da Cruz, M. Prochnow, J.-N. Roux, and F. Chevoir. *Dense granular flows: friction and jamming*, chapter 1.8, pages 361–364. Taylor & Francis Group, Stuttgart, Germany, 2005.

[131] A. Ries, D. E. Wolf, and T. Unger. Shear zones in granular media: Three-dimensional contact dynamics simulation. *Phys. Rev. E*, 76(5):051301, 2007.

[132] D. Fenistein and M. van Hecke. Wide shear zones in granular bulk flow. *Nature 425*, 425:256, 2003.

[133] D. Fenistein, J.-W. van de Meent, and M. van Hecke. Universal and wide shear zones in granular bulk flow. *Physical Review Letters*, 92(9):094301, 2004.

[134] T. Unger, J. Török, J. Kertész, and D. E. Wolf. Shear band formation in granular media as a variational problem. *Physical Review Letters*, 92(21):214301, 2004.

[135] D. Fenistein, J.-W. van de Meent, and M. van Hecke. Core precession and global modes in granular bulk flow. *Physical Review Letters*, 96(11):118001, 2006.

[136] J. Török, T. Unger, J. Kertész, and D. E. Wolf. Shear zones in granular materials: Optimization in a self-organized random potential. *Phys. Rev. E*, 75(1):011305, 2007.

[137] C. S. Changa and P.-Y. Hicherb. An elasto-plastic model for granular materials with microstructural consideration. *International Journal of Solids and Structures*, 42(14):4258–4277, 2005.

[138] S.-J. Chao. *Elastoplastic stress-strain model for granular material based on static hypothesis*. PhD thesis, UMass Amherst, Amherst, USA.

[139] I. Goldhirsch. Rapid granular flows. *Annu. Rev. Fluid Mech.*, 35:267–293, 2003.

[140] P. G. Rognon, J.-N. Roux, F. Chevoir, and M. Naaim. *Rheology of cohesive granular materials*, chapter 3.2, pages 565–568. Taylor & Francis Group, Stuttgart, Germany, 2005.

[141] G. Lois, A. Lemaître, and J. M. Carlson. Numerical tests of constitutive laws for dense granular flows. *Physical Review E*, 72(5):051303, 2005.

[142] O. Pouliquen, C. Cassar, P. Jop, Y. Forterre, and M. Nicolas. Flow of dense granular material: towards simple constitutive laws. *Journal of Statistical Mechanics: Theory and Experiment*, 07:07020, 2006.

[143] P. Mills, P. G. Rognon, and F. Chevoir. *Transient rigid clusters in dense granular flows*, chapter 1.8, pages 365–368. Taylor & Francis Group, Stuttgart, Germany, 2005.

[144] J. D. Goddard. Continuum modeling of granular assemblies. In Herrmann et al. [244], pages 1–24.

[145] S. B. Savage. Modeling and granular material boundary value problems. In Herrmann et al. [244], pages 25–96.

[146] D. Volfson, L. S. Tsimring, and I. S. Aranson. Partially fluidized shear granular flows: Continuum theory and molecular dynamics simulations. *Physical Review E*, 68(2):021301, 2003.

[147] L. S. Tsimring I. S. Aranson. Continuum modeling of granular flow and structure formation. In Hinrichsen and Wolf [245], chapter 6, pages 143–164.

[148] P. A. Cundall and O. D. L. Strack. A discrete numerical model for granular assemblies. *Géotechnique*, 29(1):47–65, 1979.

[149] S. Luding. Molecular Dynamics Simulations of Granular Materials. In Hinrichsen and Wolf [245], chapter 13, pages 299–324.

[150] T. Pöschel and V. Buchholtz. Molecular dynamics of arbitrarily shaped granular particles. *J. Phys. I France*, 5(11):1431–1455, 1995.

[151] P. Lötstedt. Mechanical systems of rigid bodies subject to unilateral constraints. *SIAM Journal on Applied Mathematics*, 42:281–296, 1982.

[152] D. Baraff. Fast contact force computation for nonpenetrating rigid bodies. In *Computer Graphics Proceedings*, pages 23–34, Orlando, 1994.

[153] M. Jean and J. J. Moreau. Unilaterality and dry friction in the dynamics of rigid body collections. In A. Curnier, editor, *Proceedings of Contact Mechanics*

International Symposium, pages 31–48, Lausanne, Switzerland, 1992. Presses Polytechniques et Universitaires Romandes.

[154] M. Jean. The non-smooth contact dynamics method. *Comput. Methods Appl. Mech. Engrg.*, 177(3):235–257, 1999.

[155] J. J. Moreau. *New computation methods in granular dynamics*, chapter 5, pages 227–232. A.A.Balkema, Rotterdam, 1993.

[156] J. J. Moreau. Some numerical-methods in multibody dynamics - application to granular-materials. *Eur. J. Mech. A-Solids*, 13:93–114, 1994.

[157] Z. Shojaaee, M. R. Shaebani, L. Brendel, J. Török, and D. E. Wolf. An adaptive hierarchical domain decomposition method for parallel contact dynamics simulations of granular materials. *Journal of Computational Physics*, 231(2):612–628, 2012.

[158] P. A. Cundall. A computer model for simulating progressive large scale movements in blocky rock systems. In *Proc. Int. Symp. Rock Fracture, ISRM*, pages 2–8, Nancy, France, 1971.

[159] D. C. Rapaport. The event scheduling problem in molecular dynamic simulation. *J. Comp. Phys.*, 34:184–201, 1980.

[160] O. R. Walton and R. L. Braun. Viscosity, granular-temperature, and stress calculations for shearing assemblies of inelastic, frictional disks. *Journal of Rheology*, 30:949–980, 1986.

[161] L. Brendel, T. Unger, and D. E. Wolf. Contact Dynamics for Beginners. In Hinrichsen and Wolf [245], chapter 14, pages 325–343.

[162] F. V. Donzé, V. Richefeu, and S.-A. Magnier. Advances in discrete element method applied to soil, rock and concrete mechanics. *in: State of the art of geotechnical engineering, Electronic Journal of Geotechnical Engineering*, Special Issue:44, 2009.

[163] S. Luding. Collisions and contacts between two particles. In Herrmann et al. [244], pages 285–304.

[164] N. V. Brilliantov and T. Pöschel. Collision of adhesive viscoelastic particles. In Hinrichsen and Wolf [245], chapter 8, pages 189–209.

[165] P. K. Haff. Grain flow as a fluid-mechanical phenomenon. *J. Fluid Mech.*, 134:401–430, 1983.

[166] S. McNamara and W. R. Young. Inelastic collapse in two dimensions. *Phys. Rev. E*, 50(1):R28–R31, 1994.

[167] K. Iglberger and U. Rüde. Massively parallel rigid body dynamics simulations. *Computer Science - Research and Development*, 23(3):159–167, 2009.

[168] K. Iglberger and U. Rüde. Massively parallel granular flow simulations with non-spherical particles. *Computer Science - Research and Development*, 25(1):105–113, 2010.

[169] D. Kadau, L. Brendel, G. Bartels, D. E. Wolf, M. Morgeneyer, and J. Schwedes. Macroscopic and microscopic investigation on the history dependence of the mechanical behaviour of powders. *Chem. Eng. Trans.*, 3:979–984, 2003.

[170] T. Unger. Refraction of shear zones in granular materials. *Physical Review Letters*, 98(1):018301, 2007.

[171] D. E. Stewart and J. C. Trinkle. An implicit time-stepping scheme for rigid body dynamics with coulomb friction. *International journal of numerical methods in engineering*, 39:2673–2691, 1996.

[172] D. M. Kaufman, T. Edmunds, and D. K. Pai. Fast frictional dynamics for rigid bodies. *ACM Trans Graph*, 24(3):946–956, 2005.

[173] D. Kadau, G. Bartels, L. Brendel, and D. E. Wolf. Pore stabilization in cohesive granular systems. *Phase Transitions*, 76(4-5):315–331, 2003.

[174] Z. Shojaaee. Phasenübergangsmerkmale der Rheologie granularer Materie. Diploma thesis, University of Duisburg-Essen, Duisburg, Germany, 2007.

[175] T. Unger. *Characterization of static and dynamic structures in granular materials*. PhD thesis, Budapest University of Technology and Economics, 2004.

[176] F. Radjai, J. Schäfer, S. Dippel, and D. Wolf. Collective friction of an array of particles: A crucial test for numerical algorithms. *J. Phys. I France*, 7:1053–1070, 1997.

[177] D. E. Stewart. Rigid-body dynamics with friction and impact. *SIAM Review*, 42:3–39, 2000.

[178] I. Nassi and B. Shneiderman. Flowchart techniques for structured programming. *SIGPLAN Notices*, 8:12–26, 1973.

[179] T. Unger, L. Brendel, D. E. Wolf, and J. Kertész. Elastic behavior in contact dynamics of rigid particles. *Phys. Rev. E*, 65(6):061305, 2002.

[180] D. E. Stewart. Convergence of a time-stepping scheme for rigid-body dynamics and resolution of painlevé's problem. *Arch. Rational Mech. Anal.*, 145:215–260, 1998.

[181] F. Jourdan, P. Alart, and M. Jean. A gauss-seidel like algorithm to solve frictional contact problems. *Computer Methods in Applied Mechanics and Engineering*, 155:31–47, 1998.

[182] N. Estrada, E. Azéma, F. Radjaï, and A. Taboada. Identification of rolling resistance as a shape parameter in sheared granular media. *Physical Review E*, 84(1):011306, 2011.

[183] D. Kadau, G. Bartels, L. Brendel, and D. E. Wolf. Pore stabilization in cohesive granular systems. *Phase Transitions*, 76(4):315–331, 2003.

[184] D. Daudon, J. Lanier, and M. Jean. *A micro mechanical comparison between experimental results and numerical simulation of a biaxial test on 2D granular material*, pages 219–222. A.A.Balkema, Rotterdam, 1997.

[185] J. Lanier and M. Jean. Experiments and numerical simulations with 2d disks assembly. *Powder Technology*, 109(1-3):206–221, 2000.

[186] F. Calvetti, G. Combe, and J. Lanier. Experimental micromechanical analysis of a 2d granular material: relation between structure evolution and loading path. *Mechanics of Cohesive-Frictional Materials*, 2(2):121–163, 1997.

[187] H. Joer, J. Lanier, J. Desrues, and E. Flavigny. "1γ2ε": A new shear apparatus to study the behavior of granular materials. *Geotechnical Testing Journal*, 15(2):129–137, 1992.

[188] M. Röck, M. Morgeneyer, J. Schwedes, D. Kadau, L. Brendel, and D. E. Wolf. Steady state flow of cohesive and non-cohesive powders: Investigations in experiment and simulation. *Granular Matter*, 10(4):285–293, 2008.

[189] H. A. Knudsen and J. Bergli. Experimental demonstration of snell's law for shear zone refraction in granular materials. *Physical Review Letter*, 103(10):108301, 2009.

[190] T. Börzsönyi, T. Unger, and B. Szabó. Shear zone refraction and deflection in layered granular materials. *Physical Review E*, 80(6):060302, 2009.

[191] T. Preclik. Iterative rigid multibody dynamics, diploma thesis. Master's thesis, Lehrstuhl für Informatik 10 (Systemsimulation), Erlangen-Nuremberg, 2008.

[192] T. M. Preclik, K. Iglberger, and U. Rüde. Iterative rigid multibody dynamics. In K. Arczewski, J. Fraczek, and M. Wojtyra, editors, *Multibody Dynamics 2009, ECCOMAS Thematic Conference*, page 17 pp., Warsaw, Poland, 2009.

[193] T. Koziara and N. Bićanić. A distributed memory parallel multibody contact dynamics code. *nternational Journal for Numerical Methods in Engineering*, 87:1–5, 2011.

[194] M. Anitescu. Optimization-based simulation of nonsmooth rigid multibody dynamics. *Mathematical Programming*, 105(1):113–143, 2006.

[195] A. Tasora and M. Anitescu. *A Fast NCP Solver for Large Rigid-Body Problems with Contacts, Friction, and Joints*, volume 12, pages 45–55. Springer, Netherlands, 2008.

[196] M. Anitescu and A. Tasora. An iterative approach for cone complementarity problems for nonsmooth dynamics. *Computational Optimization and Applications*, 47(2):207–235, 2010.

[197] M. Anitescu and G. D. Hart. A constraint-stabilized time-stepping approach for rigid multibody dynamics with joints, contact and friction. *Int J Numer Methods Eng*, 60(14):2335–2371, 2004.

[198] H. Wengenroth. Rigid body collisions, bachelor's thesis. Master's thesis, Lehrstuhl für Informatik 10 (Systemsimulation), Erlangen-Nuremberg, 2007.

[199] M. Lätzel, S. Luding, and H. J. Herrmann. Macroscopic material properties from quasi-static, microscopic simulations of a two-dimensional shear-cell. *Granular Matter*, 2(3):123–135, 2000.

[200] J. J. Moreau. Numerical investigation of shear zones in granular materials. In Wolf and Grassberger [246], pages 233–247.

[201] Private communication with S. McNamara.

[202] Z. Shojaaee, L. Brendel, and D. E. Wolf. Rheological transition in granular media. In C. Appert-Rolland, F. Chevoir, P. Gondret, S. Lassarre, J.-P. Lebacque, and M. Schreckenberg, editors, *Traffic and Granular Flow'07*, pages 653–658, Berlin, 2009. Springer.

[203] Z. Shojaaee, A. Ries, L. Brendel, and D. E. Wolf. Rheological transitions in two- and three-dimensional granular media. In M. Nakagawa and S. Luding, editors, *Powders and Grains*, pages 519–522, New York, 2009. American Institute of Physics.

[204] C. S. Campbell. Granular material flows – an overview. *Powder Technology*, 162:208–229, 2006.

[205] Y. Forterre and O. Pouliquen. Flows of dense granular material. *Annual Review of Fluid Mechanics*, 40:1–24, 2008.

[206] L. Lacaze and R. R. Kerswell. Axisymmetric granular collapse: A transient 3d flow test of viscoplasticity. *Phys. Rev. Lett.*, 102:108305, 2009.

[207] O. Pouliquen. Scaling laws in granular flows down rough inclined planes. *Physics of Fluids*, 11(3):542, 1999.

[208] L. E. Silbert, D. Ertas, G. S. Grest, T. C. Halsey, D. Levine, and S. J. Plimpton. Granular flow down an inclined plane: Bagnold scaling and rheology. *Physical Review E*, 64(5):051302, 2001.

[209] R. M. Nedderman. *Statics and kinematics of granular materials*. Cambridge University Press, Cambridge, 1992.

[210] P. G. Rognon, J.-N. Roux, M. Naaïm, and F. Chevoir. Dense flows of cohesive granular materials. *Journal of Fluid Mechanics*, 596:21–47, 2008.

[211] Z. Shojaaee, J.-N. Roux, F. Chevoir, and D. E. Wolf. Shear flow of dense granular materials near smooth walls. I. Shear localization and constitutive laws in boundary region, 2012. Physical Review E, accepted.

[212] T. Unger. Collective rheology in quasi static shear flow of granular media. arXiv:1009.3878v1.

[213] T. Hatano. Power-law friction in closely packed granular materials. *Physical Review E*, 75:060301(R), 2007.

[214] Z. Shojaaee, L. Brendel, J. Török, and D. E. Wolf. Shear flow of dense granular materials near smooth walls. II. Block formation and suppression of slip by rolling friction, 2012. Physical Review E, accepted.

[215] C. Voivret, F. Radjaï, J.-Y. Delenne, and M. S. El Youssoufi. Multiscale force networks in highly polydisperse granular media. *Physical Review Letters*, 102(17):178001, 2009.

[216] J. Török, Z. Shojaaee, and L. Brendel. Notes on the velocity profile of simple shear. in preparation.

[217] H. P. Zhu and A. B. Yu. The effects of wall and rolling resistance on the couple stress of granular materials in vertical flow. *Physica A*, 325(3):347–360, 2003.

[218] T. Pöschel and N. V. Brilliantov. Rolling friction of a viscous sphere on a hard plane. *Europhys. Lett.*, 42(3):511–516, 1998.

[219] D. Porcino, V. Fioravante, V. N. Ghionna, and S. Pedroni. Interface behavior of sands from constant normal stiffness direct shear tests. *Geotechnical Testing Journal*, 26(3):1–13, 2003.

[220] J. T. DeJong, J. D. Frost, and M. Sacs. Relating quantitative measures of surface roughness and hardness to geomaterial interface strength. In *Proceedings of Geo-Eng 2000 Conference*, Sydney, 2000. CD-ROM.

[221] F. Radjai. Turbulentlike fluctuations in quasistatic flow of granular media. *Physical Review Letters*, 89(6):064302, 2002.

[222] D. M. Mueth, G. F. Debregeas, G. S. Karczmar, P. J. Eng, S. R. Nagel, and H. M. Jaeger. Signatures of granular microstructure in dense shear flows. *Nature*, 406:385–389, 2000.

[223] C. Josserand. A 2d asymmetric exclusion model for granular flows. *Europhysics Letters*, 48(1):36–42, 1999.

[224] S. Plimpton. Fast parallel algorithms for short-range molecular dynamics. *J. Comp. Phys.*, 117(1):1–19, 1995.

[225] L. Nyland, J. Prins, R. H. Yun, J. Hermans, H.-C. Kum, and L. Wang. Achieving scalable parallel molecular dynamics using dynamic spatial domain decomposition techniques. *J. Parallel Distrib. Comput.*, 47(2):125–138, 1997.

[226] Y. Deng, R. F. Peierls, and C. Rivera. An adaptive load balancing method for parallel molecular dynamics simulations. *J. Comp. Phys.*, 161(1):250–263, 2000.

[227] S. J. Plimpton. Fast parallel algorithms for short-range molecular dynamics. *J. Comp. Phys.*, 117(1):1–19, 1995.

[228] S. Miller and S. Luding. Event-driven molecular dynamics in parallel. *J. Comp. Phys.*, 193(1):306–316, 2003.

[229] A. Tasora, D. Negrut, and M. Anitescu. *GPU-Based Parallel Computing for the Simulation of Complex Multibody Systems with Unilateral and Bilateral Constraints: An Overview*, pages 283–307. Springer-Verlag, Netherlands, 2011.

[230] P. Breitkopf and M. Jean. Modélisation parallèle des matériaux granulaires. In *4ème colloque national en calcul des structures*, pages 387–392, Giens, 1999.

[231] M. Renouf, F. Dubois, and P. Alart. A parallel version of the non smooth cantact dynamics algorithm applied to the simulation of granular media. *J. Comput. Appl. Math.*, 168(1):375–382, 2004.

[232] M. R. Shaebani, T. Unger, and J. Kertész. Generation of homogeneous granular packings: Contact dynamics simulations at constant pressure using fully periodic boundaries. *Int. J. Mod. Phys. C*, 20(6):847–867, 2009.

[233] W. Press, S. A. Teukolsky, W. T. Vetterling, and B. P. Flannery. *Numerical Recipes: The Art of Scientific Computing*. Cambridge University Press, Cambridge, 2007.

[234] V. Zhakhovskii, K. Nishihara, Y. Fukuda, and S. Shimojo. *A new dynamical domain decomposition method for parallel molecular dynamics simulation on grid*, pages 147–150. Osaka University, Institute of Laser Engineering, 2004.

[235] J. K. Salmon. *Parallel hierarchical N-body methods*. PhD thesis, Caltech University, Pasadena, U.S.A., 1990.

[236] M. S. Warren and J. K. Salmon. A parallel hashed oct-tree n-body algorithm. In *Proceedings of Supercomputing 93*, pages 12–21, 1993.

[237] F. Fleissner and P. Eberhard. Parallel load-balanced simulation for short-range interaction particle methods with hierarchical particle grouping based on orthogonal recursive bisection. *Int. J. Numer. Meth. Engng*, 74(4):531–553, 2008.

[238] M. P. Allen and D.J. Tildeslay. *Computer Simulation of Liquids*. Oxford University Press, Oxford, 1987.

[239] M. Wackenhut, S. McNamara, and H. J. Herrmann. Shearing behavior of polydisperse media. *Eur. Phys. J. E*, 17:237–246, 2005.

[240] V. Ogarko and S. Luding. Data structures and algorithms for contact detection in numerical simulation of discrete particle systems. In *Proc. of World Congress Particle Technology 6*, Nuremberg, 2010. Nürnberg Messe GmbH.

[241] S. Revathi and V. Balakrishnan. Effective diffusion constant for inhomogeneous diffusion. *J. Phys. A: Math. Gen.*, 26:5661–5673, 1993.

[242] M. R. Shaebani, T. Unger, and J. Kertész. Extent of force indeterminacy in packings of frictional rigid disks. *Phys. Rev. E*, 79(5):052302, 2009.

[243] T. Unger, J. Kertész, and D. E. Wolf. Force indeterminacy in the jammed state of hard disks. *Physical Review Letters*, 94(17):178001, 2005.

[244] H. J. Herrmann, J.-P. Hovi, and S. Luding, editors. *Physics of dry granular media*, volume NaTO ASI Series, Series E: Applied Science- Vol.35. Kluwer Acad. Publ., Dordrecht, 1998.

[245] H. Hinrichsen and D. E. Wolf, editors. *The Physics of Granular Media*. Wiley-VCH, Berlin, 2004.

[246] D. E. Wolf and P. Grassberger, editors. *Friction, Arching, Contact Dynamics*. World Scientific, London, 1997.

[247] R. P. Behringer and J. T. Jenkins, editors. *Powders & Grains 97*. A.A.Balkema, Rotterdam, 1997.

Danksagung

An dieser Stelle, möchte ich mich bei allen, die diese Arbeit unterstützt haben bedanken.

An erster Stelle danke ich Herrn Prof. Dr. Dietrich E. Wolf, der diese Promotion an seinem Lehrstuhl ermöglicht hat. Ihm danke ich ebenfalls für die zahlreichen Auslandsaufenthalte und Konferenzteilnahmen.

Dr. Lothar Brendel danke ich ganz herzlich für die zahlreichen Diskussionen, seine Anmerkungen zu den Publikationen und dieser Arbeit und seine Hilfsbereitschaft bei technischen Fragen. Dr. Reza Shaebani danke ich für die fruchtbaren Diskussionen und die Zusammenarbeit, welche zur Parallelisierung des Kontakt Dynamik Modells geführt haben und ebenfalls für die Korrektur der vorliegenden Arbeit. Dr. János Török danke ich für seinen Anstoß zu den Kapiteln 8 und 9 dieser Arbeit.

Bei Dr. Jean-Noël Roux und Dr. François Chevoir bedanke ich mich für viele inspirierende Diskussionen bei der gemeinsamen Arbeit und ihre Gastfreundlichkeit bei meinen Aufenthalten in Paris. Bei Prof. Dr. Stefan Luding und Prof. Isaac Goldhirsch bedanke ich mich ebenfalls für viele hilfreiche Diskussionen.

Bei allen anderen Kollegen der Arbeitgruppe Wolf bedanke ich mich für Diskussionen und mentale Unterstützung.

Bei Michael und Andrea Farle bedanke ich mich sehr für deren hilfreichen und netten Beistand.

Michael Vennemann danke ich herzlich für seine Unterstützung und Motivation während meine Doktorarbeit, liebevolle Unterstützung im Leben und für die zahlreichen Korrekturarbeiten. Ohne seine Hilfe (Betreuung unseres Sonnenscheins Philipp Sepehr) wäre die Vollendung dieser Arbeit nicht möglich gewesen.

Nicht zuletzt möchte ich mich bei meinen Eltern bedanken, die größten Wert auf das

Lernen gelegt haben. Leider hat mein Vater die Vollendung dieser Arbeit nicht erleben dürfen. Diese Arbeit widme ich meinen lieben Eltern. Bei meinen Geschwistern und Familie Vennemann bedanke ich mich ebenfalls für deren mentale Unterstützung.

Erklärung

Ich versichere, dass ich die von mir vorgelegte Dissertation selbständig angefertigt, die benutzten Quellen und Hilfsmittel vollständig angegeben und die Stellen der Arbeit - einschließlich der Abbildungen -, die anderen Werken im Wortlaut oder dem Sinn nach entnommen sind, in jedem Einzelfall als Entlehnung kenntlich gemacht habe; dass diese Dissertation noch keiner anderen Fakultät oder Universität zur Prüfung vorgelegen hat; dass sie - abgesehen von unten angegebenen Teilpublikationen - noch nicht veröffentlicht worden ist sowie, dass ich eine solche Veröffentlichung vor Abschluss des Promotionsverfahrens nicht vornehmen werde. Die Bestimmungen dieser Promotionsordnung sind mir bekannt. Die von mir vorgelegte Dissertation ist von Herrn Professor Dr. Dietrich E. Wolf betreut worden.

Duisburg, den 20. Juni 2012

Teilpublikationen

1) Z. Shojaaee, J.-N. Roux, F. Chevoir, D. E. Wolf
Shear flow of dense granular materials near smooth walls. I.
Shear localization and constitutive laws in boundary region
Accepted to be published in Physical Review E, 2012.

2) Z. Shojaaee, L. Brendel, J. Török, and D. E. Wolf
Shear flow of dense granular materials near smooth walls. II.
Block formation and suppression of slip by rolling friction
Accepted to be published in Physical Review E, 2012.

3) Z. Shojaaee, M. R. Shaebani, L. Brendel, J. Török, and D. E. Wolf
An adaptive hierarchical domain decomposition method for parallel contact dynamics simulations of granular materials
Journal of Computational Physics, 231(2):612-628, 2012.

4) Z. Shojaaee, A. Ries, L. Brendel, and D. E. Wolf
Rheological Transitions in Two- and Three-Dimensional Granular Media
in: Powders and Grains 2009 (AIP CP 1145), eds: M. Nakagawa, S. Luding, (AIP, Melville, New York), 519-522, 2009.

5) Z. Shojaaee, L. Brendel, and D. E. Wolf
Rheological Transition in Granular Media
in: Traffic and Granular Flow '07 (Paris), eds: C. Appert-Rolland, F. Chevoir, P. Gondret, S. Lassarre, J.-P. Lebacque, and M. Schreckenberg, (Springer, Berlin), 653-658, 2009.